Surface Plasmon Hybridization in the Strong Coupling Regime in Gain Structures

Aurore Castanié

UNIVERSITÉ MONTPELLIER II
SCIENCES ET TECHNIQUES DU LANGUEDOC

THÈSE

pour obtenir le grade de

DOCTEUR DE L'UNIVERSITE MONTPELLIER II

Discipline : Physique de la Matière Condensée
École Doctorale : Information, Structures, Systèmes

présentée et soutenue publiquement

par

Aurore Castanié

le 4 octobre 2013

Titre :

Surface Plasmon Hybridization in The Strong Coupling Regime in Gain Structures

JURY

Prof. Dominique Barchiesi	Université de Technologie de Troyes	Président du jury
Prof. Alexey Kavokin	University of Southampton	Rapporteur
Prof. Joël Bellessa	Université Lyon 1	Rapporteur
D.R. Philippe Ben-Abdallah	Institut d'Optique	Examinateur
Prof. Didier Felbacq	Université Montpellier 2	Directeur de thèse
Prof. Brahim Guizal	Université Montpellier 2	Directeur de thèse
Mcf. Mauro Antezza	Université Montpellier 2	Examinateur

Acknowledgements

These three years of doctorate have been a really great, professional and personal, experience. First, I wish to thank Alexey Kavokin and Joël Bellessa for spending time to read my works, and Dominique Barchiesi, Philippe Ben-Abdallah and Mauro Antezza for doing me the honor of agreeing to be part of my examination committee.

Je tiens tout particulièrement à remercier mes directeurs de thèse, Brahim Guizal et Didier Felbacq pour m'avoir guidée dans mes recherches et m'avoir appris tant de choses. Ce fut véritablement une expérience très enrichissante pour moi. Je souhaite tout autant remercier mes collègues de travail avec lesquels j'ai partagé un bureau et de nombreuses conversations informelles.

Je remercie ma famille pour son soutien et sa patience durant ces trois années et même durant celles qui les ont précédées ! Merci à Richard pour sa présence et le sacrifice de vacances d'été au profit de ma (nos !) rédaction(s). J'espère aussi t'avoir apporté mon soutien et continuer à le faire. Merci à Elisabeth pour ses conseils, à Dominique pour ses corrections d'anglais, à Olivia, à Marie, à mon Père, à ma Mère... Merci en somme.

Contents

Introduction

Nanophotonics and micro-optics had a remarkable impact on all kinds of applications in communications, sensing, imaging, data storage, etc [1]... However, the size of a dielectric waveguide is still ruled by the diffraction limit ($\lambda/(2n)$, n being the guide refractive index and λ being the free space wavelength of the incident wave). It has been discovered that waveguides based on surface plasmon polaritons can support propagation modes tightly bounded to the metallic surfaces and confine the waves in deep sub-wavelength scales. Accordingly, plasmonics has received tremendous attention for its scope to overcome the diffraction limit. In order to present the context and the perspective of this work, it is appropriate to start out with a short introduction to the plasmonics' research history.

Plasmonics is a branch of nanophotonics devoted to the study of surface plasmon polaritons (SPs) and their applications. In 1902, R. W. Wood [2] observed sudden variations of the intensity in the light beam spectrum, reflected by a diffraction grating under the transverse magnetic polarization. According to him, the intensity of the incident beam being continuous, the reflected spectrum had to be continuous too. These variations are strongly dependent on the incident angle of the light beam, and it was demonstrated later that they are due to the coupling between the propagating incident waves and the surface plasmons waves. In 1957, R. H. Ritchie [3] demonstrated theoretically the existence of transverse plasmons on a metallic surface. In 1958, R. A. Ferrel studied, also theoretically, the coupling of these modes with an electromagnetic wave and presented the first determination of the dispersion relation corresponding to electromagnetic waves on a metallic surface. Using a mono-kinetic electronic beam, C. J. Powell and J. B. Swan [4] experimentally observed surface plasmon excitations at metallic interfaces. A. Otto proposed an experimental configuration based of the use on a prism, called the FTR (Frustrated Total Reflection) configuration, to observe the coupling between

an electromagnetic wave and surface plasmons. E. Kretschmann [5] modified and simplified this geometry towards the well-known ATR (Attenuated Total Reflection) configuration. It was only in 1989 that it became possible to observe surface plasmons using Scanning Near-field Optical Microscopy (SNOM) [6, 7].

Research in plasmonics has made very fast progress in the following decades [8, 9, 10, 11, 12, 13]. In 1998, T. W. Ebbesen *et al.* [14] described an experiment in which nanoholes in a silver film allow a great transmission of light through sub-wavelength nanostructures when the standard aperture theory [15] predicted a very small light transmission for such small holes. To explain this phenomenon, different devices were analysed and the experiments showed that this effect persists on all metals and with a strong angle dependency. It was thus assumed that this was a SP related effect. This result renewed the interest for studying SPs and the term plasmonics began to be used shortly after.

Plasmonics have been very beneficial in terms of resolution for lenses [16] since the studies carried out by J. B. Pendry [17] and by N. Fang *et al.* [18]. They are also used to enhance light emission [19] or photovoltaic devices [20]. The LSPR (localized surface plasmon resonance) allows the electromagnetic field enhancement that leads to surface-enhanced Raman scattering (SERS) [21], second harmonic generation [22] and other surface-enhanced spectroscopic processes [23]. Imaging at the single molecule level has also taken advantage of the enhancement of the fluorescence on plasmonic surfaces [24, 25] or in solutions containing metallic nanoparticles [26]. At present, the range of plasmonics based biosensors is dominated by instruments that operate using the Kretschmann arrangement (this configuration is presented in Section 2.3.1). The physical size of the sensing element is limited by the propagation length of the SP. The new approach pursued now is to combine SPR with other types of guided modes (hybrid sensors). For instance, in metamaterial arrays of silver nanorods capable of supporting a guided mode, the interaction between the guided mode and the SPR leads to excellent sensor performances in the near infrared [27].

In the field of sub-wavelength surface optics, Zhijun *et al.* [28] presented the possibility of creating metallic Fresnel-like lenses. These were designed in such a way that each nanoslit element transmits light with phase retardation controlled by the metal thickness in the aperture region. The advantage, as compared to the conventional lenses, is the possibility to control each phase shift separately by

changing the corresponding slit depth.

The SP modes play key roles in today's nanophotonics [29] and are also used in many applications such as detection, or in surface optics. However, the intrinsic losses due to the metal limit their propagation length and thus their applications [30, 31, 32, 33]. To enhance this propagation length, many possibilities have been considered. The older one consists in coupling two surface plasmons. When a metallic film becomes too thin, the two SP modes which are on each interface between the metal and the dielectric media can interact and there is a coupling [34, 35, 36]. The result is the creation of two new modes, known as the $LRSP$ (Long Range Surface Plasmon) which is characterized by a better propagation length than the SP on a metallic bulk [37] and the $SRSP$ (Short Range Surface Plasmon) which has a lower propagation length. Going on from there, a large range of applications [38, 39, 40], such as in photonic crystals, stratified media, quantum systems or with anisotropy, become possible.

A more recent and famous way to enhance the propagation length of the SP modes is the use of gain media. These structures involve adding gain in a dielectric medium with a metallic film directly deposited on it [41, 42]. However, the improvement of the field is limited by the depth penetration of the plasmon in the two media. Thus, the efficiency of this approach is insufficient.

Another point of view consists in thinking that the SPs are light waves that we want to amplify as a laser. This possibility has been explored and has been called a SPASER. It could generate stimulated emission of surface plasmons in resonating metallic nanostructures adjacent to a gain medium [43, 44]. The light emission could also be coherent, which can give interesting applications in sub-wavelength surface optics.

In the same idea, it was reported the use of confined Tamm plasmon modes towards the realization of nano-lasers [45]. Their advantage in comparison of classical SP modes is that they can be directly excited with light wave because their in-plane wave vector is less than the wave vector of light in vacuum. They can also be formed in both TM and TE polarizations [46, 47]. A first demonstration of laser emission for Tamm structures is presented in [45].

The configuration we propose here consists of putting gain into the medium between a SP and a classical waveguide under the regime of the strong coupling. This regime allows a significant improvement of the SP emission as will be pre-

sented in this work.

Scope of this thesis

We begin by providing an overview of the theoretical foundations of SPs by the means of Maxwell's equations. The aim of this first chapter is to present the tools used to compute and study multistratified media through both the dispersion and absorption relations. Thus, we present the transfer and scattering matrix methods, which are usual methods to study multistratified media. These methods need to be extended in order to find the modes and to account for the losses of the structure. The losses lead to a complex dispersion relation. It is also possible to demonstrate that the existence of solutions corresponds to the maximisation of the determinant of the scattering matrix, that is to say the *poles* of this matrix. Thereafter, it is demonstrated that the poles of a complex function can be found though Cauchy's integral theorem. The development of our technique of computation, called the *tetrachotomy* method, according to [48] is also presented.

Chapter 2 concerns the definition of the surface plasmon polaritons and their coupling, when a metallic film supporting two SP modes becomes thin enough to allow the interaction. To begin, the coupling between a volume plasmon and a photon generates a surface plasmon. When the collective oscillation of the electrons' gas is coupled with light at the interface between a metal and a dielectric, we also talk about surface plasmon polaritons (noted SPs). The SP modes correspond to solutions of Maxwell's equations. There are two ways to find them: we can search solutions corresponding to evanescent waves on both sides of the interface; or we can search for the response of the structure with the determination of the reflection and transmission coefficients r and t when an electromagnetic plane wave comes to hurt the structure.

The scope of this chapter is to present the coupling between SP modes, the result being the creation of two modes, known as the $LRSP$ (Long Range Surface Plasmon) which is characterized by better propagation length than the SP on a metallic bulk, and the $SRSP$ (Short Range Surface Plasmon) defined by a lower propagation length. The main drawback of using the SP modes resides in their intrinsic losses, and the $LRSP$ modes can provide a first solution to reduce them. We finally demonstrate the possibility to excite a $LRSP$ mode without the $SRSP$

mode on a perfect electric conductor (PEC) substrate. This last possibility is a first step towards the use of the $LRSP$ for applications such as the detection of molecules, the experimental realization being possible with a PEC on one side and vacuum on the other.

In Chapter 3, the coupling between two dielectric waveguides is studied in order to understand the basic physical mechanisms at play. Dielectric waveguides provide simple models for the confining mechanism of waves propagating in optical devices. The coupling of waveguides has been intensively studied, in particular with the coupled-mode theory [49, 50, 51, 52, 53]. After a reminder concerning the dielectric slab waveguides, the coupled-mode theory will be presented. This theory can be derived from the variational principle for the frequencies of the system. When a trial solution is introduced into the electric field in a lossless electromagnetic system, such as the linear superposition of modes, the coupled-mode theory gives the result. The coupled-modes theory is presented both for the transverse electric and transverse magnetic polarizations, the latter one never having been published. The last section deals with the case of two optical waveguides respecting the parity time (PT) symmetry. This symmetry has been evidenced in quantum mechanics by C. M. Bender [54] but it can also apply to optical devices. Furthermore, a numerical application is also presented.

The last chapter focuses on the strong coupling regime. This regime has been particularly studied in microcavities since the work of C. Weisbuch *et al.* [55]. The strong coupling is characterized by an anticrossing between the original modes dispersion relations and by the apparition of a Rabi splitting [56] between the new modes of the structures. In the first section, the characteristics of the strong coupling regime are introduced, with the classical case of two coupled oscillators. Then, the properties of the strong coupling regime in microcavities are presented until recent works implying surface plasmons. Finally, we demonstrate the strong coupling regime between SP modes and guided modes in a layered structure. More precisely, we study the features of the new modes so as to justify the interest of this kind of structure. Gain is added in order to further enhance the plasmon emission. In this way, we obtain an improvement of the propagation length for a hybrid surface plasmon mode (that is still confined on the surface) of more than six thousand times the length of the strongly coupled case without gain.

Chapter 1

Theoretical and Numerical Tools

Overview All the structures we are going to study are stratified media, thin and smooth films alternated in layers. We study more precisely the corresponding dispersion relations which allow the determination of the modes living in the structures and also give information about their interactions. After reminding the wave equation, the propagation equations in a stratified media are introduced. The transfer matrix (T-matrix) method is also presented and compared to the scattering matrix (S-matrix) method. The S-matrix formalism allows to find the coefficients of reflection R and transmission T but also the modes of the structure. We demonstrate that it is sufficient to find the poles of the determinant of the S-matrix to obtain the dispersion curves and the corresponding absorption curves. The fundamental properties of polology are summed up and we describe the method we used, namely the *tetrachotomy method*.

1.1 Wave equation

1.1.1 Maxwell's equations

Published in 1864, Maxwell's equations predicted the propagation - even in vacuum - of electromagnetic waves. More precisely, they predicted a velocity c for these waves in vacuum. It is possible to demonstrate that this velocity is the speed of light and only depends on two known constants: $c = (\mu_0 \varepsilon_0)^{-1/2}$ with μ_0 and ε_0 the

permeability and the permittivity of the vacuum, respectively[1].

In linear, isotropic, homogeneous (LIH) and source-free medium, Maxwell's equations are:

$$\nabla \times \mathbf{E} = -\frac{\partial \mathbf{B}}{\partial t}, \tag{1.1}$$

$$\nabla \times \mathbf{H} = \frac{\partial \mathbf{D}}{\partial t}, \tag{1.2}$$

$$\nabla \cdot \mathbf{D} = 0, \tag{1.3}$$

$$\nabla \cdot \mathbf{B} = 0, \tag{1.4}$$

with $\varepsilon_r(x, y, z)$, the permittivity of the medium. In what follows, we only consider non-magnetic media, where $\mu = \mu_0$.

To find a self-consistent solution for the electromagnetic field, Maxwell's equations must be supplemented by the constitutive relations that describe the behavior of matter under the influence of the fields. Thus, the electric displacement field $\mathbf{D}$ is defined by:

$$\mathbf{D} = \varepsilon_0 \mathbf{E} + \mathbf{P}, \quad (\text{in vacuum } \mathbf{D} = \varepsilon_0 \mathbf{E}). \tag{1.5}$$

$\mathbf{D}$ is used to avoid explicit inclusion of the charge associated with the polarization $\mathbf{P}$ in Gauss's flux law (Eq. 1.3). Equivalently, we can also write the polarization $\mathbf{P} = \chi \varepsilon_0 \mathbf{E}$, where the electric susceptibility χ is given by $\chi = \varepsilon_r - 1$. Then, the expression of the magnetic induction field $\mathbf{B}$ is:

$$\mathbf{B} = \mu_0(\mathbf{H} + \mathbf{M}). \tag{1.6}$$

In what follows, $\mathbf{B}$ will always be replaced by its equivalent $\mu_0 \mathbf{H}$ because $\mathbf{M} = 0$ for LIH and non-magnetic medium.

Combining Eqs. 1.1 and 1.2 leads to *Helmholtz's equations* for $\mathbf{E}$ and $\mathbf{H}$:

$$\frac{1}{\varepsilon_r(x, y, z)} \nabla \times [\nabla \times \mathbf{E}] - \frac{\omega^2}{c^2} \mathbf{E} = 0, \tag{1.7}$$

[1]By definition, the exact value of μ_0 is $4\pi.10^{-7}$ $H.m^{-1}$ and the measured value of ε_0 is $8,854.10^{-12}$ $F.m^{-1}$.

$$\nabla \times \left[\frac{1}{\varepsilon_r(x,y,z)} \nabla \times \mathbf{H} \right] - \frac{\omega^2}{c^2} \mathbf{H} = 0, \tag{1.8}$$

where $\omega/c = k_0 = 2\pi/\lambda_0$ with λ_0, the wavelength of light in vacuum.

In the case of metallic media, Ampere's equation (Eq. 1.2) includes the differential form of Ohm's law $j = \sigma E$, because the conductivity $\sigma \neq 0$ (more precisely, it is not negligibly small). Eq. 1.2 becomes:

$$\nabla \times \mathbf{H} + \mathrm{i}\omega\varepsilon\mathbf{E} - \mathbf{j} = \nabla \times \mathbf{H} + \mathrm{i}\omega \left(\varepsilon + \mathrm{i}\frac{\sigma}{\omega} \right) \mathbf{E} = 0. \tag{1.9}$$

To rewrite this equation in its initial form, we have to introduce an effective dielectric permittivity $\tilde{\varepsilon}$ in order to account for the conductivity term σ:

$$\tilde{\varepsilon} = \varepsilon + i\frac{\sigma}{\omega}. \tag{1.10}$$

In the case of homogeneous metals, $\tilde{\varepsilon}$ is constant and independent of the direction in space, it follows that $\nabla \cdot \mathbf{E} = 0$ is still used. The corresponding Helmholtz's equation is also given by Eq. 1.7 with $\varepsilon_r(x,y,z) = \tilde{\varepsilon}/\varepsilon_0$.

1.1.2 Solution of the wave equation

We consider Maxwell's equations for vacuum ($\varepsilon_r(x,y,z) = 1$) in order to obtain the simplest form of the electromagnetic wave equation and to present the well known solution of the wave equation. The Ampere and Faraday equations are rewritten as:

$$\nabla \times \mathbf{E} = -\mu_0 \frac{\partial \mathbf{H}}{\partial t}, \tag{1.11}$$

$$\nabla \times \mathbf{H} = \varepsilon_0 \frac{\partial \mathbf{E}}{\partial t}. \tag{1.12}$$

The solutions for $\mathbf{E}$ and $\mathbf{H}$ can be separated by taking the curl of Eq. 1.11 and the time derivative of Eq. 1.12. Then, using the fact that the order of differentiation can be reversed, the two Maxwell's wave equations are:

$$\nabla^2 \mathbf{E} = \mu_0 \varepsilon_0 \frac{\partial^2 \mathbf{E}}{\partial t^2}, \tag{1.13}$$

$$\nabla^2 \mathbf{H} = \mu_0 \varepsilon_0 \frac{\partial^2 \mathbf{H}}{\partial t^2}. \tag{1.14}$$

These equations are the form:

$$\frac{\mathrm{d}^2 \mathbf{A}}{\mathrm{d}x^2} = \frac{1}{c^2} \frac{\mathrm{d}^2 \mathbf{A}}{\mathrm{d}t^2}. \tag{1.15}$$

For simplicity, we only consider the wave propagation in a single spatial direction, the x-direction. The vector $\mathbf{A}$ becomes a function of x and t and may be expressed as $\mathbf{A}(x,t)$. It could represent either the electric field vector $\mathbf{E}(x,t)$ or the magnetic field vector $\mathbf{H}(x,t)$. c is still the velocity of light in vacuum.

It is possible to demonstrate that $\mathbf{A}(x,t)$ is an oscillatory wave function with an amplitude that is transverse to the direction of propagation. We assume that the wave function $\mathbf{A}(x,t)$ is separable and thus can be written as a product of functions $\mathrm{A}_z(z)$ and $\mathrm{A}_t(t)$. Eq. 1.15 becomes:

$$\frac{c^2}{A_z} \frac{\mathrm{d}^2 A_z}{\mathrm{d}z^2} = \frac{1}{A_t} \frac{\mathrm{d}^2 A_t}{\mathrm{d}t^2}. \tag{1.16}$$

Both sides must be equal to a negative constant $-\omega^2$ in order to satisfy the equation [2]. That leads to the following equations:

$$\frac{\mathrm{d}^2 A_x}{\mathrm{d}x^2} + \frac{\omega^2}{c^2} A_x = 0, \tag{1.17}$$

$$\frac{\mathrm{d}^2 A_t}{\mathrm{d}t^2} + \omega^2 A_t = 0. \tag{1.18}$$

And the corresponding solutions are:

$$A_x = c_1 e^{ik_x x} + c_2 e^{-ik_x x}, \tag{1.19}$$

$$A_t = d_1 e^{i\omega t} + d_2 e^{-i\omega t}, \tag{1.20}$$

where the constants c_1, c_2, d_1 and d_2 are determined by the boundary conditions

[2] The consequence of the choice of a positive constant for $\mathrm{A}_t(t)$ would be real exponential that cannot represent a real field. On the other hand, taking a negative constant leads to periodic functions $\mathrm{A}_t(t) = e^{\pm i\omega t}$ with $\omega = kc$, so the solutions could be monochromatic waves.

and the propagation constant $k_x = \omega/c = 2\pi/\lambda$. Finally, the general solution involves a complex wave function:

$$A(x,t) = A_x(x)A_t(t) \propto e^{\pm i[k_x x \mp \omega t]}. \tag{1.21}$$

The wave described by Eq. 1.21 represents a wave that, for any value of x, has the same amplitude value for all values of y and z. It is thus referred to as a *plane wave* since it represents planes of constant value that are of infinite lateral extent.

We consider a wave travelling from left to right that is a function of the form $A(x,t) = ce^{i(k_x x - \omega t)}$ and the more general form for $\mathbf{A}(x,y,z,t)$ is:

$$\mathbf{A} = \mathbf{A}_0 e^{i(\mathbf{k}\cdot\mathbf{r} - \omega t)}. \tag{1.22}$$

with $\mathbf{A}$ the electric or magnetic component of an electromagnetic wave. So, with this type of solution, $\nabla \cdot \mathbf{E} = 0$ can be associated to $\nabla \cdot \mathbf{E} = i\mathbf{k} \cdot \mathbf{E}$ from Eq. 1.22. That involves $i\mathbf{k} \cdot \mathbf{E} = 0$, and thus $\mathbf{E}$ is perpendicular to $\mathbf{k}$, the direction of propagation. The same conclusion is found with the magnetic field $\mathbf{H}$ and Eq. 1.4. Hence, these electromagnetic waves are referred to as *transverse waves*.

1.2 Wave propagation in a stratified medium

All the structures we are going to study are stratified media, thin and smooth films alternated in layers. More precisely, we study the corresponding dispersion relations which allow the determination of the modes living in the structures, and also give information concerning their interactions.

The relation between the angular frequency of an incident wave and the magnitude of its wave vector is the dispersion relation [3]. In this work, we will always consider ω real, and the propagation constant α complex.

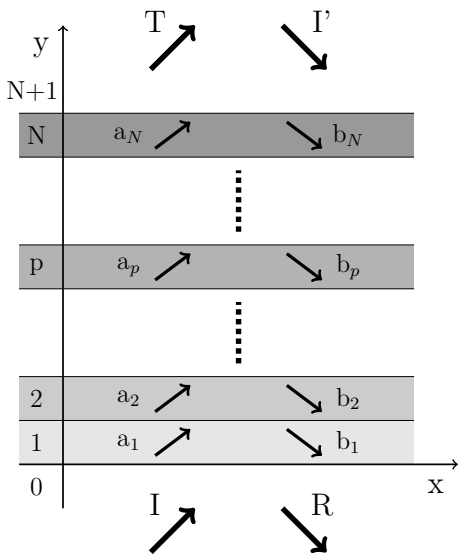

Figure 1.1: Stratified medium with layers from 1 to N. We note the outgoing amplitudes R and T and the incoming ones I and I'. The intermediate layers have the amplitudes a_p and b_p ($p = 1 \dots N$).

1.2.1 Propagation equations

Expression of the field

We consider a stratified medium with layers from 0 to $N+1$ (Fig. 1.1) [57]. In a LIH medium, with the time dependence $e^{-i\omega t}$ and the TM polarization in the plane (x, y), we denote the magnetic field as $\mathbf{H} = H(x, y)\mathbf{e}_z$. The field $H(x, y)$ satisfies the following Helmholtz's equation:

$$\mathrm{div}(\varepsilon_j^{-1} \nabla H) + k_j^2 H = 0, \tag{1.23}$$

where $k_j^2 = k_0^2 \varepsilon_j$ is the wave vector in each layer j. This equation has to be solved separately in regions of constant ε_j, and the solutions obtained must be matched using appropriate boundary conditions. We note α and β_j the wave vectors in the

[3]The dispersion relation, $\omega = \omega(\alpha)$ with α the in-plane component of the wave vector (the propagation constant), is a linear equation with constant coefficients which determines how the temporal oscillations $\exp(-i\omega t)$ are linked to the spatial oscillations $\exp(i\alpha x)$, with plane waves $\exp(i\alpha x)\exp(-i\omega(\alpha)t)$ as solutions.

x and the y directions.

We note $H(x,y) = e^{i\alpha x}u(y)$ and the field $u(y)$ in each medium j satisfies:

$$\frac{\partial^2 u}{\partial y^2} + (k_j^2 - \alpha^2)u = 0, \tag{1.24}$$

The solutions are plane waves $e^{i(\mathbf{k}\cdot\mathbf{r}-\omega t)} = e^{i(\alpha x+\beta_j y-\omega t)}$ and the dispersion relation is given by $\alpha^2 + \beta_j^2 = k_0^2\varepsilon_j$ with $\mu_r = 1$.

The field in the different layers is:

$$u_0(x,y) = Ie^{i(\alpha x+\beta_0 y)} + Re^{i(\alpha x-\beta_0 y)}, \tag{1.25}$$

$$u_p(x,y) = a_p e^{i(\alpha x+\beta_p y)} + b_p e^{i(\alpha x-\beta_p y)} \quad \text{with } p = 1\ldots N, \tag{1.26}$$

$$u_{N+1}(x,y) = Te^{i(\alpha x+\beta_{N+1} y)} + I'e^{i(\alpha x-\beta_{N+1} y)}. \tag{1.27}$$

Before applying the boundary conditions, we can simplify the previous expressions. First, we must impose that there are no incoming waves in the medium of transmission $(N+1)$, $I' = 0$. Moreover, the quantity β_j is defined in terms of the quantities k_j and α:

$$\beta_j = \begin{cases} \sqrt{k_0^2\varepsilon_j - \alpha^2} \text{ if } \mid \alpha \mid < k_0\sqrt{\varepsilon_j}, \\ i\sqrt{\alpha^2 - k_0^2\varepsilon_j} \text{ if } \mid \alpha \mid > k_0\sqrt{\varepsilon_j}. \end{cases} \tag{1.28}$$

The first condition $\mid \alpha \mid < k_0\sqrt{\varepsilon_j}$ implies that β_j is real and corresponds to propagating waves. The second condition $\mid \alpha \mid > k_0\sqrt{\varepsilon_j}$ implies that β_j is imaginary and corresponds to evanescent waves. Evanescent waves are solutions that remain confined in the near vicinity of an interface between two media.

Boundary conditions

We apply the boundary conditions to solve Eqs. 1.25, 1.26 and 1.27 with $p = 1\ldots N$. For each interface, u and $\varepsilon_j^{-1}\partial_y u$ must be conserved in the TM polariza-

tion. For $y = 0$:

$$\begin{cases} e^{i\alpha x}\left(Ie^{i\beta_0 0} + Re^{-i\beta_0 0}\right) = e^{i\alpha x}\left(a_1 e^{i\beta_1 0} + b_1 e^{-i\beta_1 0}\right), \\ i\frac{\beta_0}{\varepsilon_0}e^{i\alpha x}\left(Ie^{i\beta_0 0} - Re^{-i\beta_0 0}\right) = i\frac{\beta_1}{\varepsilon_1}e^{i\alpha x}\left(a_1 e^{i\beta_1 0} - b_1 e^{-i\beta_1 0}\right). \end{cases} \tag{1.29}$$

For $y = y_p$:

$$\begin{cases} e^{i\alpha x}\left(a_p e^{i\beta_p y_p} + b_p e^{-i\beta_p y_p}\right) = e^{i\alpha x}\left(a_{p+1} e^{i\beta_{p+1} y_p} + b_{p+1} e^{-i\beta_{p+1} y_p}\right), \\ i\frac{\beta_p}{\varepsilon_p}e^{i\alpha x}\left(a_p e^{i\beta_p y_p} - b_p e^{-i\beta_p y_p}\right) = i\frac{\beta_{p+1}}{\varepsilon_{p+1}}e^{i\alpha x}\left(a_{p+1} e^{i\beta_{p+1} y_p} - b_{p+1} e^{-i\beta_{p+1} y_p}\right). \end{cases} \tag{1.30}$$

For $y = y_N$:

$$\begin{cases} e^{i\alpha x}\left(a_{N+1} e^{i\beta_N y_N} + b_{N+1} e^{-i\beta_N y_N}\right) = e^{i\alpha x}\left(Te^{i\beta_{N+1} y_N} + 0e^{-i\beta_{N+1} y_N}\right), \\ i\frac{\beta_N}{\varepsilon_N}e^{i\alpha x}\left(a_{N+1} e^{i\beta_N y_N} - b_{N+1} e^{-i\beta_N y_N}\right) = i\frac{\beta_{N+1}}{\varepsilon_{N+1}}e^{i\alpha x}\left(Te^{i\beta_{N+1} y_N} - 0e^{-i\beta_{N+1} y_N}\right). \end{cases} \tag{1.31}$$

These systems of equations can be solved by using the following matrix-methods which give access to the expression of the fields in each layer.

1.2.2 The Transfer matrix method

The T-matrices are found by considering Eqs. 1.29, 1.30 and 1.31 under matrix form. For $y = 0$:

$$\begin{bmatrix} 1 & 1 \\ \frac{\beta_0}{\varepsilon_0} & -\frac{\beta_0}{\varepsilon_0} \end{bmatrix} \begin{bmatrix} I \\ R \end{bmatrix} = \begin{bmatrix} 1 & 1 \\ \frac{\beta_1}{\varepsilon_1} & -\frac{\beta_1}{\varepsilon_1} \end{bmatrix} \begin{bmatrix} a_1 \\ b_1 \end{bmatrix}. \tag{1.32}$$

For $y = y_p$:

$$\begin{aligned} &\begin{bmatrix} 1 & 1 \\ \frac{\beta_p}{\varepsilon_p} & -\frac{\beta_p}{\varepsilon_p} \end{bmatrix} \begin{bmatrix} e^{i\beta_p y_p} & 0 \\ 0 & e^{-i\beta_p y_p} \end{bmatrix} \begin{bmatrix} a_p \\ b_p \end{bmatrix} \\ &\qquad = \begin{bmatrix} 1 & 1 \\ \frac{\beta_{p+1}}{\varepsilon_{p+1}} & -\frac{\beta_{p+1}}{\varepsilon_{p+1}} \end{bmatrix} \begin{bmatrix} e^{i\beta_{p+1} y_p} & 0 \\ 0 & e^{-i\beta_{p+1} y_p} \end{bmatrix} \begin{bmatrix} a_{p+1} \\ b_{p+1} \end{bmatrix}. \end{aligned} \tag{1.33}$$

For $y = y_N$:

$$\begin{bmatrix} 1 & 1 \\ \frac{\beta_N}{\varepsilon_N} & -\frac{\beta_N}{\varepsilon_N} \end{bmatrix} \begin{bmatrix} e^{i\beta_N y_N} & 0 \\ 0 & e^{-i\beta_N y_N} \end{bmatrix} \begin{bmatrix} a_N \\ b_N \end{bmatrix} = \begin{bmatrix} 1 & 1 \\ \frac{\beta_{N+1}}{\varepsilon_{N+1}} & -\frac{\beta_{N+1}}{\varepsilon_{N+1}} \end{bmatrix} \begin{bmatrix} e^{i\beta_{N+1} y_N} & 0 \\ 0 & e^{-i\beta_{N+1} y_N} \end{bmatrix} \begin{bmatrix} T \\ 0 \end{bmatrix}. \tag{1.34}$$

The T-matrices relate the amplitudes I and R to the amplitudes T and I' ($I' = 0$):

$$\begin{bmatrix} I \\ R \end{bmatrix} = \begin{bmatrix} \tau_{11} & \tau_{12} \\ \tau_{21} & \tau_{22} \end{bmatrix} \begin{bmatrix} T \\ I' \end{bmatrix}. \tag{1.35}$$

$$\Leftrightarrow$$

$$\begin{bmatrix} I \\ R \end{bmatrix} = \begin{bmatrix} 1 & 1 \\ \frac{\beta_0}{\varepsilon_0} & -\frac{\beta_0}{\varepsilon_0} \end{bmatrix}^{-1} T_1 \times T_2 \times \ldots T_N \times \begin{bmatrix} 1 & 1 \\ \frac{\beta_{N+1}}{\varepsilon_{N+1}} & -\frac{\beta_{N+1}}{\varepsilon_{N+1}} \end{bmatrix} \begin{bmatrix} T \\ 0 \end{bmatrix}, \tag{1.36}$$

with the T-matrices written as:

$$T_p = \begin{bmatrix} 1 & 1 \\ \frac{\beta_p}{\varepsilon_p} & -\frac{\beta_p}{\varepsilon_p} \end{bmatrix} \begin{bmatrix} e^{-i\beta_p(y_{p+1}-y_p)} & 0 \\ 0 & e^{i\beta_p(y_{p+1}-y_p)} \end{bmatrix} \begin{bmatrix} 1 & 1 \\ \frac{\beta_p}{\varepsilon_p} & -\frac{\beta_p}{\varepsilon_p} \end{bmatrix}^{-1}, \; p = 1 \ldots N. \tag{1.37}$$

With the T-matrix method, finding the expression of the fields in a stratified medium is reduced to the multiplication of the T-matrices obtained for each elementary layer of the structure. The coefficients of transmission T and reflection R are given by $T = I/\tau_{11}$ and $R = \tau_{11}T$, respectively. In Eq. 1.37, the presence of two opposed exponentials in the matrix, $e^{i\beta_p(y_{p+1}-y_p)}$ and $e^{-i\beta_p(y_{p+1}-y_p)}$, causes bad conditioned matrices and instability for the resolution of great systems [58].

In the next section, we present the S-matrix method that relates the outgoing fields to incoming ones, and removes the problem of instability [59].

1.2.3 The Scattering matrix method

The S-matrix formalism allows to find the coefficients of reflection and transmission R and T, but also all the modes of the structure [60, 61, 62, 63, 64]. It relates the outgoing amplitudes, R and T, to the incoming ones, I and $I^{'}$ (Fig. 1.1).

The combination of the S-matrices obtained for each elementary layer of the structure is no longer simple. It is necessary to cascade the S matrices [65]. This

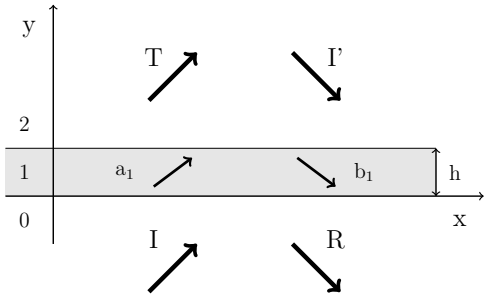

Figure 1.2: Slab with the outgoing amplitudes R and T and the incoming ones I and I'. The intermediate layer has the amplitudes a_1 and b_1. The thickness of the slab is h.

technique is presented for the case of a slab (Fig. 1.2).

The field in the different layers is written as (Eq. 1.26):

$$u_0(x,y) = Ie^{i(\alpha x+\beta_0 y)} + Re^{i(\alpha x-\beta_0 y)}, \tag{1.38}$$

$$u_1(x,y) = a_1 e^{i(\alpha x+\beta_1 y)} + b_1 e^{i(\alpha x-\beta_1 y)}, \tag{1.39}$$

$$u_2(x,y) = Te^{i(\alpha x+\beta_2 (y-h))} + I'e^{i(\alpha x-\beta_2 (y-h))}. \tag{1.40}$$

We directly apply the boundary conditions (as in Section 1.2.1) and simplify the expressions. For $y = 0$:

$$\begin{cases} I + R = a_1 + b_1, \\ \frac{\beta_0}{\varepsilon_0}(I - R) = \frac{\beta_1}{\varepsilon_1}(a_1 - b_1). \end{cases} \tag{1.41}$$

For $y = h$:

$$\begin{cases} a_1 e^{i\beta_1 h} + b_1 e^{-i\beta_1 h} = T + I', \\ \frac{\beta_1}{\varepsilon_1}(a_1 e^{i\beta_1 h} - b_1 e^{-i\beta_1 h}) = \frac{\beta_2}{\varepsilon_2}(T - I'). \end{cases} \tag{1.42}$$

Under the matrix form, the S matrices are obtained from:

$$\begin{bmatrix} a_1 \\ R \end{bmatrix} = \begin{bmatrix} 1 & -1 \\ \frac{\beta_1}{\varepsilon_1} & \frac{\beta_0}{\varepsilon_0} \end{bmatrix}^{-1} \begin{bmatrix} -1 & 1 \\ \frac{\beta_1}{\varepsilon_1} & \frac{\beta_0}{\varepsilon_0} \end{bmatrix} \begin{bmatrix} b_1 \\ I \end{bmatrix}, \tag{1.43}$$

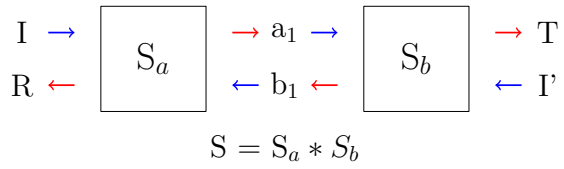

Figure 1.3: Cascade of the S-matrix with $S = S_a * S_b$: in red, the outgoing amplitudes; in blue, the incoming ones.

and:

$$\begin{bmatrix} T \\ b_1 \end{bmatrix} = \begin{bmatrix} 1 & 0 \\ 0 & e^{i\beta_1 h} \end{bmatrix} \begin{bmatrix} 1 & -1 \\ \frac{\beta_2}{\varepsilon_2} & \frac{\beta_1}{\varepsilon_1} \end{bmatrix}^{-1} \begin{bmatrix} -1 & 1 \\ \frac{\beta_2}{\varepsilon_2} & \frac{\beta_1}{\varepsilon_1} \end{bmatrix} \begin{bmatrix} 1 & 0 \\ 0 & e^{i\beta_1 h} \end{bmatrix} \begin{bmatrix} I' \\ a_1 \end{bmatrix}. \tag{1.44}$$

We denote S_a and S_b the two intermediate S-matrices (Fig. 1.3), and their expressions are respectively:

$$\begin{bmatrix} a_1 \\ R \end{bmatrix} = \begin{bmatrix} S_{a11} & S_{a12} \\ S_{a21} & S_{a22} \end{bmatrix} \begin{bmatrix} b_1 \\ I \end{bmatrix}, \tag{1.45}$$

and:

$$\begin{bmatrix} T \\ b_1 \end{bmatrix} = \begin{bmatrix} S_{b11} & S_{b12} \\ S_{b21} & S_{b22} \end{bmatrix} \begin{bmatrix} I' \\ a_1 \end{bmatrix}. \tag{1.46}$$

The global matrix, noted S, has the following components:

$$\begin{cases} S_{11} = S_{a11} + S_{a12}(I_d - S_{b11}S_{a22})^{-1}S_{b11}S_{a21}, \\ S_{12} = S_{a12}(I_d - S_{b11}S_{a22})^{-1}S_{b12}, \\ S_{21} = S_{b21}(I_d - S_{a22}S_{b11})^{-1}S_{a21}, \\ S_{22} = S_{b22} + S_{b21}(I_d - S_{a22}S_{b11})^{-1}S_{a22}S_{b12}. \end{cases} \tag{1.47}$$

The final result is also:

$$\begin{aligned} \begin{pmatrix} T \\ R \end{pmatrix} = (S_a * S_b) \begin{pmatrix} I' \\ I \end{pmatrix} = S \begin{pmatrix} I' \\ I \end{pmatrix} \\ = \begin{pmatrix} S_{11} & S_{12} \\ S_{21} & S_{22} \end{pmatrix} \begin{pmatrix} I' \\ I \end{pmatrix}. \end{aligned} \tag{1.48}$$

In Eq. 1.44, the presence of only one exponential, $e^{i\beta_1 h}$, implies that the conditioning of the S-matrix is better than in the case of the T-matrices. It is possible to demonstrate that this result can be generalized to N layers.

The modes of the structure are defined by the existence of outgoing waves in the absence of excitation. With $\mathbf{OUT} = (R, T)$, this condition is equivalent to $S^{-1}\mathbf{OUT} = 0$. Thus, to find the modes of the structure, for each frequency ω, we have to find the propagation constant α which corresponds to the cancellation of the determinant of the S^{-1}-matrix. It is equivalent to finding the maximization of the determinant of the S-matrix, that is the poles of $\det S(\omega, \alpha)$.

However, the S-matrix contains complex variables and the numerical determination of its poles is not a simple extension of the equivalent problem for a function of a real variable.

There are two types of methods to find the zeros or the poles of a function of a complex variable. The first are the iterative methods. The most common one is the Newton method (also known as the Newton-Raphson method). In this method, we need a first estimated value of the sought zero or pole. After that, successive approximations are generated and can converge to the right solution. This method has not been sufficient to find the poles of the S-matrix because of its intrinsic instability (the convergence is a function of the first estimated value) and the requirement to give this first value. Similarly, the Muller's method did not give us more satisfaction. This method, which is based on the secant method, also requires initial values.

The second type of methods implies the use of Cauchy's integrals for holomorphic functions. For each frequency ω, we look for the corresponding poles in the complex plane. The extension in the complex plane requires a recap of the complex analysis and more precisely the pology theory [66].

1.3 The pology theory

1.3.1 Cauchy's integral formula and Laurent series

We consider a path integral which encloses a point singularity $z = z_0$, and the function to be integrated is:

$$g(z) = \frac{f(z)}{z - z_0}, \tag{1.49}$$

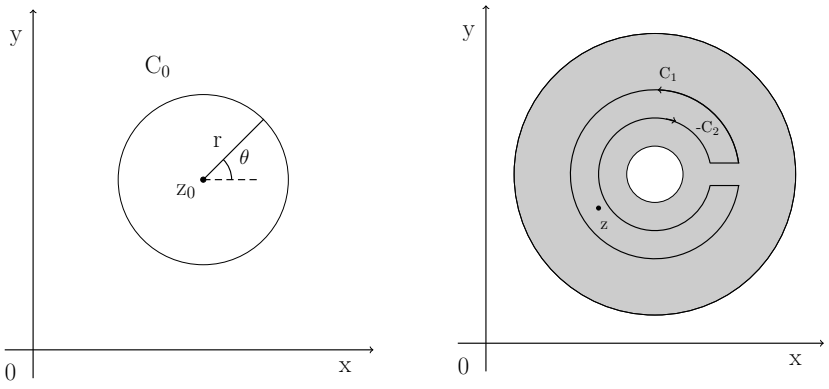

(a) (b)

Figure 1.4: (a) A path C_0 which is a circle of radius r centred on the point z_0. (b) The contour used to derive the Laurent expansion of a function.

where $f(z)$ is analytic on and within the contour of integration C. $g(z)$ at the singularity $z = z_0$ is non-analytic. It is possible to demonstrate that the integral over any closed path around $z = z_0$ gives the same result. We can also consider a path C_0 which is a circle of radius r centred on the point z_0 as illustrated in Fig. 1.4a.

In polar coordinates, $z - z_0 = re^{i\theta}$ and $\mathrm{d}z = ire^{i\theta}\mathrm{d}\theta$. The integral is thus:

$$\int_{C_0} \frac{f(z)}{z - z_0}\mathrm{d}z = if(z_0)\int \mathrm{d}\theta = 2\pi i f(z_0). \tag{1.50}$$

Theorem [67]: Cauchy's integral formula *Let $f(z)$ be analytic inside and on a simple closed contour C. Then at any point z inside the contour,*

$$f(z) = \frac{1}{2\pi i}\oint_C \frac{f(z')}{z' - z}\mathrm{d}z'. \tag{1.51}$$

To accommodate expansions about singular point, we have to consider the *Laurent expansions* that are more general expansions than Taylor series. For an analytic function $f(z)$ in an annular region, we consider Cauchy's formula for the contour shown in Fig 1.4b with C_2 defined as the *counter-clockwise* path around the circle. We take the limit that the segments which join the two circles come

arbitrarily close together, so that their contributions cancel. Cauchy's formula then becomes:

$$f(z) = \frac{1}{2\pi i}\int_{C_1}\frac{f(z^{'})}{z^{'}-z}\mathrm{d}z^{'} - \frac{1}{2\pi i}\int_{C_2}\frac{f(z^{'})}{z^{'}-z}\mathrm{d}z^{'}. \tag{1.52}$$

We can write $z^{'}-z = (z^{'}-z_0)-(z-z_0)$. However, on the curve C_1, $|z^{'}-z_0| > |z-z_0|$, while for C_2, $|z^{'}-z_0| < |z-z_0|$. In the first integral, we pull out the term $1/(z^{'}-z_0)$ and in the second integral we pull out the term $1/(z-z_0)$. Then, expanding the geometric term, we have:

$$\begin{aligned} f(z) = \frac{1}{2\pi i}\sum_{n=0}^{\infty}(z-z_0)^n \oint_{C_1}\frac{f(z^{'})}{(z^{'}-z_0)^{n+1}}\mathrm{d}z^{'} \\ + \frac{1}{2\pi i}\sum_{n=0}^{\infty}(z-z_0)^{-n-1}\oint_{C_2}(z^{'}-z_0)^n f(z^{'})\mathrm{d}z^{'}. \end{aligned} \tag{1.53}$$

The first summation looks like the usual Taylor series expansion of an analytic function, while the second summation is singular at the point $z = z_0$. These two series may be combined into one, referred to as a Laurent series:

$$f(z) = \sum_{n=-\infty}^{\infty} a_n(z-z_0)^n, \tag{1.54}$$

where

$$a_n = \frac{1}{2\pi i}\oint_{C}\frac{f(z^{'})}{(z^{'}-z_0)^{n+1}}\mathrm{d}z^{'}, \tag{1.55}$$

and C is now any counter-clockwise contour within the annulus.

The last step in finding an expression of the pole z_0 is to consider the Residue theorem.

1.3.2 Residue theorem

Let us consider a function which has a Laurent expansion about the point $z = z_0$. The integral about a circle of radius r (the closed path) centred on this point is:

$$\oint\sum_{n=-\infty}^{\infty} a_n(z-z_0)^n\mathrm{d}z = \sum_{n=-\infty}^{\infty} a_n\oint(z-z_0)^n\mathrm{d}z. \tag{1.56}$$

The evaluation of this integral is possible term by term because the series is uniformly convergent.

Then, it is possible to demonstrate with Cauchy's theorem that all terms for which $n \geq 0$ vanish. For $n = -m < 0$,

$$a_{-m} \oint (z - z_0)^{-m} = a_{-m} \int_0^{2\pi} r^{-m} e^{-im\theta} ire^{i\theta} \mathrm{d}\theta = ia_{-m} r^{-m+1} \int_0^{2\pi} e^{-i(m-1)\theta} \mathrm{d}\theta. \tag{1.57}$$

This integral is identically zero, except for $m = 1$, or $n = -1$ and the contour integral about the point $z = z_0$ reduces to:

$$\oint f(z)\mathrm{d}z = 2\pi i a_{-1}. \tag{1.58}$$

This contour integral only depends on the value a_{-1}, which is called the *residue* of the function $f(z)$ at $z = z_0$, which we will write as $\mathrm{Res}(z_0)$. In the case when the contour encloses several singular points of $f(z)$ as in Fig. 1.5, it is possible to demonstrate that we finally obtain:

$$\oint_C f(z)\mathrm{d}z = 2\pi i \left[\sum_i \mathrm{Res}(z_i) \right]. \tag{1.59}$$

This equation may be stated as a theorem and this theorem reduces the evaluation of a contour integral of the function $f(z)$ to the algebraic determination of the residues of the function.

Theorem: Residue theorem [67] *The integral of a function $f(z)$ which is analytic on and within a closed contour except at a finite number of isolated singular points is given by $2\pi i$ times the sum of the residues enclosed by the contour.*

If the singularity $z = z_0$ is a simple pole (pole of order 1), the corresponding Laurent expansion is:

$$f(z) = \frac{a_{-1}}{z - z_0} + \sum_{n=0}^{\infty} a_n (z - z_0)^n. \tag{1.60}$$

Cauchy's theorem allows to obtain:

$$a_{-1} = \frac{1}{2i\pi} \int_C f(z)\mathrm{d}z, \tag{1.61}$$

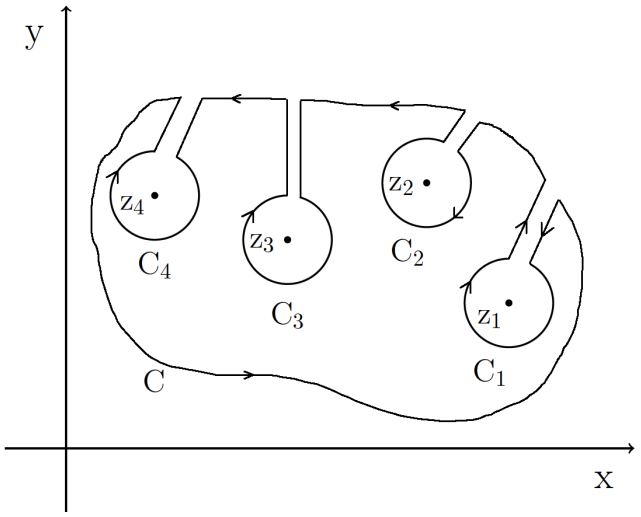

Figure 1.5: A contour which can be used to evaluate a path integral enclosing numerous isolated singularities.

and also:

$$z_0 a_{-1} = \frac{1}{2i\pi} \int_C z f(z) \mathrm{d}z. \tag{1.62}$$

Then, by comparing both results, the value of the pole z_0 is:

$$z_0 = \frac{\int_C z f(z) \mathrm{d}z}{\int_C f(z) \mathrm{d}z}. \tag{1.63}$$

1.3.3 Branch points and cut lines

The existence of a square root in the quantity β_j (Eq. 1.28) implies a problem of definition in the complex plane. Indeed, some singularities cannot be classified using an ordinary Laurent series. A classical example is also the square root of a complex function:

$$f(z) = z^{1/2}. \tag{1.64}$$

For a real function $f(x) = \sqrt{x}$, we already have to choose between two possible roots, $+\sqrt{x}$ and $-\sqrt{x}$. For the roots of a complex number z with $z = z_0 e^{2\pi n i}$, we

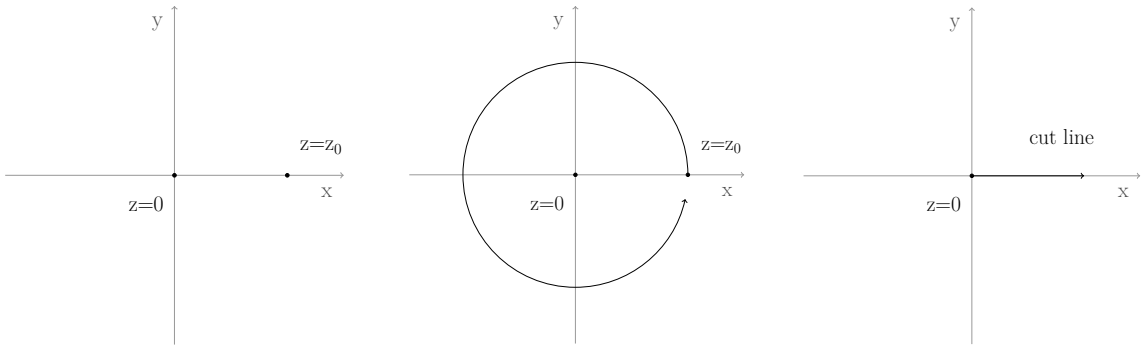

(a) (b) (c)

Figure 1.6: The multivalued nature of the function $f(z) = z^{1/2}$ with the branch point $z = 0$: (a) Starting at point z_0 with $f(z_0) = z_0^{1/2}$; (b) Ending at point z_0 with $f(z_0) = -z_0^{1/2}$. (c) The cut line (where argument discontinuous) introduced by defining a multivalued function by a branch defined by $0 < \arg(z) < 2\pi$.

have the same dilemma:

$$z^{1/2} = z_0^{1/2} e^{\pi n i} = \begin{cases} +z^{1/2}, \\ \text{or} \\ -z^{1/2}. \end{cases} \tag{1.65}$$

Likewise, there are two possible choices for the square root, except at the point $z = 0$, where the only possibility is 0. Then, we have the following problem: when we consider a closed circular path around the point $z = 0$ and if we are starting at the point $z = z_0$ (Fig. 1.6a), we are ending up at a different value than when we started,

$$f(z) \to z_0^{1/2} e^{\pi i} = -z_0^{1/2}, \tag{1.66}$$

as it is illustrated in Fig. 1.6b. It is not possible to develop a Taylor or Laurent series for the point $z = 0$. This kind of point is called a *branch point* and the function $z^{1/2}$ has two "branches", a positive one and a negative one.

In this case, we always choose the positive branch of $f(z) = z^{1/2}$, but one line in the complex plane along which the function $f(z)$ is discontinuous always exists as illustrated in Fig 1.6c.

Such a line is usually referred to as a *cut line*. Fortunately, its location depends on the phase of the complex number. If $0 \leq \arg(z) < 2\pi$, the cut line runs from

the origin to infinity along the positive x-axis. If $-\pi < \arg(z) \leq \pi$, the cut line runs from the origin to infinity along the negative x-axis. It is possible to choose other arguments to move the cut lines in other directions. In our case, it is often necessary to move it because the function $f(z)$ is non-analytic along this cut line and Cauchy's theorem cannot be used across this line. Therefore, we wrote a function in Matlab in order to move it and to have access to the poles we were looking for [4].

Riemann sheets

Another possibility, introduced by B. Riemann, is to consider both branches together. As we have noted, our choice of the location of the cut line is arbitrary for the function $f(z) = z^{1/2}$. Riemann suggested that the proper domain of the function $f(z)$ is a pair of complex planes which are joined together along the cut line, as opposed to a single complex plane.

This geometry is illustrated in Fig. 1.7 and corresponds to the construction of a surface by cutting each of the two complex planes along their cut lines, and then connecting the cut edges of one plane to the opposing edges of the other.

Therefore, the function $f(z)$ is analytic on this pair of complex planes except at the point $z = 0$. This linked set of planes is referred to as a *Riemann surface*, and each individual complex plane is called a *Riemann sheet*. It must be noted that the Riemann surfaces cannot be constructed in three-dimensional space without the surfaces crossing. If we consider the function $f(z) = z^{1/3}$, we find that the Riemann surface consists of three complex planes joined together along a cut line.

Branch points are broadly grouped into three categories. *Algebraic branch points* are those of the form of a fractional power of z and can be expressed by a series,

$$f(z) = (z - z_0)^{\alpha} \sum_{n=-\infty}^{\infty} a_n (z - z_0)^n , \tag{1.67}$$

when $a_n = 0$ for all $n < -N$. In such a case, the function can be described by a finite number of Riemann sheets. If $a_n \neq 0$, as $n \to -\infty$, it is referred to as a *transcendental branch point*, and it is the multivalued analogue of an isolated

[4] According to the location of the cut line, a pole can be seen as a zero and a zero as a pole. That is why we need to know in advance where we have to look in order to find the poles corresponding to the physical modes.

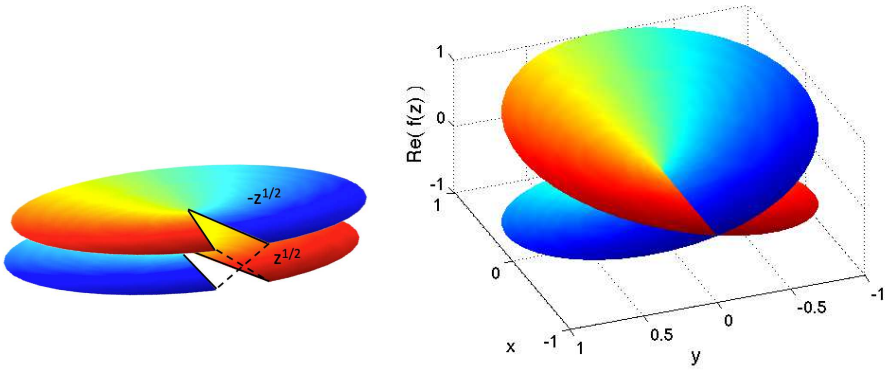

(a) (b)

Figure 1.7: (a) An illustration of the Riemann surfaces of the multivalued function $f(z) = z^{1/2}$. (b) The real part of $\sqrt{z}$, showing how the two surfaces are tied together.

essential singularity. *Logarithmic branch points* are those which behave as follows:

$$f(z) = (z - z_0)^{\alpha} \log(z - z_0) \sum_{n=-\infty}^{\infty} a_n (z - z_0)^n . \tag{1.68}$$

In such a case, the function can be described with an infinite number of Riemann sheets.

The main drawback for our study is the presence of the square root in the expression of β_j (Eq. 1.28). We stay in the case of algebraic branch points and the use of our function to move the cut line is always enough to apply Cauchy's theorem at the right regions. An interesting method that applies Cauchy's theorem to find the modes in a structure - initially in photonic crystals - was developed by F. Zolla *et al.* [48]. This method is called the tetrachotomy method and we have adapted it to our study.

1.4 The tetrachotomy method

1.4.1 Poles of a meromorphic function

The tetrachotomy method allows to find the poles in the complex plane corresponding to a given meromorphic function $f(\alpha)$ in $\mathbb{C}$ [48]. If $f(\alpha)$ has a single pole at α_0, then in the neighbourhood of that point there exists a non-vanishing

holomorphic function $G(\alpha)$ (in $\mathbb{C}\setminus\{\alpha_0\}$) and the function f can be written as [68]:

$$f(\alpha) = \frac{G(\alpha)}{\alpha - \alpha_0}. \tag{1.69}$$

First, we consider a Jordan loop Γ which only contains the pole α_0. We assume that the pole α_0 is simple and that G does not have a pole at $\alpha = 0$, so that we can rewrite it $G(\alpha) = \alpha F(\alpha)$ with F a holomorphic function. We can demonstrate that the following integrals allow to determine the pole α_0:

$$I_0 = \frac{1}{2i\pi}\int_\Gamma \frac{f(\alpha)}{\alpha}\mathrm{d}\alpha = \frac{1}{2i\pi}\int_\Gamma \frac{F(\alpha)}{\alpha - \alpha_0}\mathrm{d}\alpha, \tag{1.70}$$

$$I_1 = \frac{1}{2i\pi}\int_\Gamma f(\alpha)\mathrm{d}\alpha = \frac{1}{2i\pi}\int_\Gamma \alpha\frac{F(\alpha)}{\alpha - \alpha_0}\mathrm{d}\alpha, \tag{1.71}$$

$$I_2 = \frac{1}{2i\pi}\int_\Gamma \alpha f(\alpha)\mathrm{d}\alpha = \frac{1}{2i\pi}\int_\Gamma \alpha^2\frac{F(\alpha)}{\alpha - \alpha_0}\mathrm{d}\alpha. \tag{1.72}$$

F being a holomorphic function, that implies the integrals $\int_\Gamma F(\alpha)\mathrm{d}\alpha$ and $\int_\Gamma \alpha F(\alpha)\mathrm{d}\alpha$ are vanishing. Then,

$$I_1 = \frac{1}{2i\pi}\int_\Gamma \alpha\frac{F(\alpha)}{\alpha - \alpha_0}\mathrm{d}\alpha = \frac{1}{2i\pi}\int_\Gamma \alpha_0\frac{F(\alpha)}{\alpha - \alpha_0}\mathrm{d}\alpha + \frac{1}{2i\pi}\int_\Gamma F(\alpha)\mathrm{d}\alpha, \tag{1.73}$$

and after simplification:

$$I_1 = \frac{\alpha_0}{2i\pi}\int_\Gamma \frac{F(\alpha)}{\alpha - \alpha_0}\mathrm{d}\alpha = \alpha_0 I_0. \tag{1.74}$$

The expression of the pole is also $\alpha_0 = I_1/I_0$. Similarly,

$$I_2 = \frac{1}{2i\pi}\int_\Gamma \alpha^2\frac{F(\alpha)}{\alpha - \alpha_0}\mathrm{d}\alpha = \frac{1}{2i\pi}\int_\Gamma \alpha F(\alpha)\mathrm{d}\alpha + \frac{\alpha_0}{2i\pi}\int_\Gamma F(\alpha)\mathrm{d}\alpha + \frac{\alpha_0^2}{2i\pi}\int_\Gamma \frac{F(\alpha)}{\alpha - \alpha_0}\mathrm{d}\alpha. \tag{1.75}$$

The expression of the pole is then $\alpha_0^2 = I_2/I_0 = \alpha_0 I_1/I_0$.

The pole α_0 of the function $f(\alpha)$ is precisely given by:

$$\alpha_0 = \frac{I_2}{I_1} = \frac{I_1}{I_0}. \tag{1.76}$$

This is the direct application in the case where there is only one pole. As a

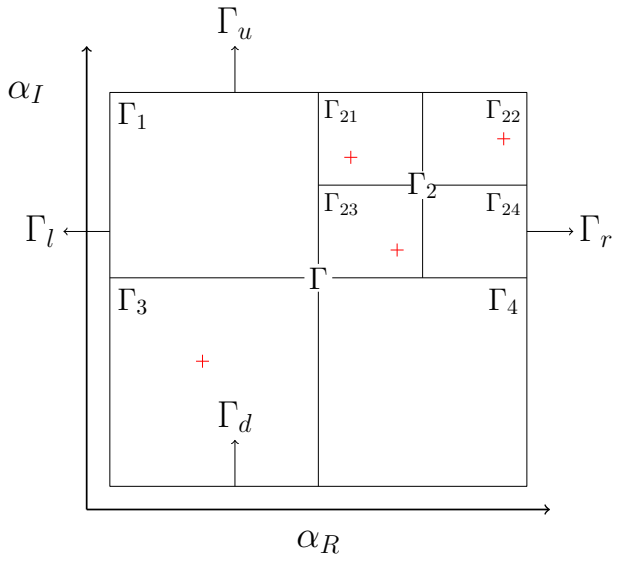

Figure 1.8: The Tetrachotomy algorithm performed on a rectangle in the complex plane (α_R, α_I). The poles are represented by red crosses.

matter of fact, for a given meromorphic function f in $\mathbb{C}$, the number of corresponding poles $\{\alpha_i\}$ in the complex plane is unknown. The schematic representation of the tetrachotomy method is shown in Fig. 1.8.

The first step is then to isolate the poles from each other. The evaluation of the integrals I_0, I_1 and I_2 enables to know if there is no pole, one pole or several poles inside the loop Γ. Indeed, three possibilities arise:

1. If $I_0 = I_1 = 0$, there is no pole inside the considering loop (as in the loops Γ_1, Γ_4 and Γ_{24} in Fig. 1.8).

2. If $I_2/I_1 \neq I_1/I_0$, that means there are several poles (as the loop Γ_2 in Fig. 1.8).

3. When $I_2/I_1 = I_1/I_0$, there is one pole in the considering loop and the evaluation of one of the fractions of Eq. 1.76 gives very precisely the sought pole (as in the loops Γ_3, Γ_{21}, Γ_{22} and Γ_{23} in Fig. 1.8).

The principle of the tetrachotomy method is, whenever the second situation arises, to divide the rectangle Γ into four equal rectangles Γ_i $(i = [1, 2, 3, 4])$, and

to repeat the process until the initial rectangle is divided into rectangles which all contain only one pole as it is illustrated in Fig. 1.8.

The efficiency of this method is linked to the numeric evaluation of the integrals I_0, I_1 and I_2. Their precise determination is possible because $f(\alpha)$ is analytic in $\mathbb{C} \setminus \{\alpha_i\}$. The restrictive function f to the rectangle Γ, noted $f(\alpha)_{|\Gamma}$, is regular as the curve Γ and that means it is continue only. However, if we split the initial loop as (Fig. 1.8):

$$\int_{\Gamma} f(\alpha)\mathrm{d}\alpha = \int_{\Gamma_d} f(\alpha)\mathrm{d}\alpha + \int_{\Gamma_r} f(\alpha)\mathrm{d}\alpha + \int_{\Gamma_u} f(\alpha)\mathrm{d}\alpha + \int_{\Gamma_l} f(\alpha)\mathrm{d}\alpha, \tag{1.77}$$

the function $f(\alpha)_{|\Gamma_a}$ $(a = d, r, u, l)$ is also always derivable.

We suppose that Γ is parametrised by $z(t)$ with $z(t) \in [0, 2\pi]$. The integrals of $f(\alpha)_{|\Gamma_a}$ along the loops Γ_a are given by:

$$\int_{\Gamma_d} f(\alpha)\mathrm{d}\alpha = \int_0^{\frac{\pi}{2}} f(z(t))z'(t)\mathrm{d}t, \tag{1.78}$$

$$\int_{\Gamma_r} f(\alpha)\mathrm{d}\alpha = \int_{\frac{\pi}{2}}^{\pi} f(z(t))z'(t)\mathrm{d}t, \tag{1.79}$$

$$\int_{\Gamma_u} f(\alpha)\mathrm{d}\alpha = \int_{\pi}^{\frac{3\pi}{2}} f(z(t))z'(t)\mathrm{d}t, \tag{1.80}$$

$$\int_{\Gamma_r} f(\alpha)\mathrm{d}\alpha = \int_{\frac{3\pi}{2}}^{2\pi} f(z(t))z'(t)\mathrm{d}t. \tag{1.81}$$

We can show that the quantities of these integrals only depend on Γ (they do not depend on the parametrisation). The trajectories are parametrised with:

$$z(t) = \begin{cases} \frac{2}{\pi}(x_1 - x_0)t + x_0 + iy_0 \text{ on } \Gamma_d, \\ x_1 + i[\frac{2}{\pi}(y_1 - y_0)(t - \frac{\pi}{2})] + y_0 \text{ on } \Gamma_r, \\ \frac{2}{\pi}(x_1 - x_0)(\frac{3\pi}{2} - t) + x_0 + iy_1 \text{ on } \Gamma_u, \\ x_0 + i[d\frac{2}{\pi}(y_1 - y_0)(2\pi - t) + y_0] \text{ on } \Gamma_l. \end{cases} \tag{1.82}$$

The numerical evaluation is obtained by the method of integration called the periodisation method [69]. This is based on the fact that if $I_n(f)$ is the approx-

imation of $I = \int_a^b f(t)\mathrm{d}t$, the error yielded by the rectangle method integration $e_n = I_n - I$ decreases as $O(\frac{1}{N})$, where N is the number of rectangles used to approximate the function and goes to infinity [70]. However, if f is a function of class C^{2k} on the integration interval $[a, b]$ and if its odd-order derivatives satisfy the condition:

$$\forall p \in \{1, \ldots, k-1\} q^{(2p-1)}(a) = q^{(2p-1)}(b), \tag{1.83}$$

then the error behaves like $O(N^{-2k})$ when N goes to infinity, which means the evaluation is more efficient and more precise. The functions $f(z(t))z'(t)$ are functions of class $C^\infty([a, b])$ but they are not functions that satisfy the condition Eq. 1.83.

With the periodisation method, it is possible to find a change of variables such that the parametrisation of the integrals yields an integrand that verifies condition Eq. 1.83. Hence, the computation of the integrals is made fast and accurate.

The change of variable is $t = P(x)$, where $P(x)$ is a $4k-3$-degree polynomial given by:

$$P(x) = \frac{\int_a^b (t-a)^{2k-2}(b-t)^{2k-2}\mathrm{d}t}{\int_a^x (t-a)^{2k-2}(b-t)^{2k-2}\mathrm{d}t}. \tag{1.84}$$

This polynomial is strictly increasing on $[a, b]$ and verifies the following properties:

$$P(a) = 0, \quad P(b) = 1, \tag{1.85}$$

$$P^{[l]}(a) = P^{[l]}(b) = 0, \ 1 \leq l \leq 2k-1. \tag{1.86}$$

Thus, the integral of the function f is given by:

$$I = \int_a^b g(x)\mathrm{d}x, \tag{1.87}$$

with $g(x) = P'(x)f(P(x))$ where $g(x)$ is a function of class C^{2k} that satisfies the condition of Eq. 1.83.

In practice, taking $k = 2$ is enough. The convergence in $O(\frac{1}{N^4})$ is sufficient (ten times more points give four supplementary significant numbers). Thus, to calculate the integral I, the rectangle method is applied to $g(x)$ so as to obtain the periodisation method.

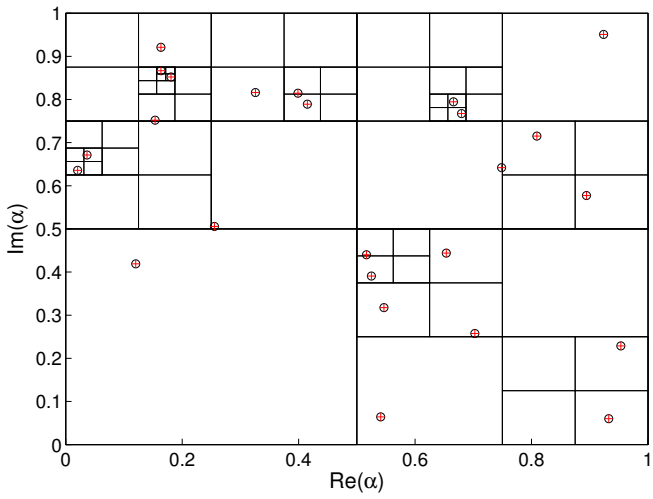

Figure 1.9: The poles found using the tetrachotomy method for a test function (red crosses) plotted against the exact (simple) poles of the meromorphic test function (black circles).

1.4.2 Application

To test the validity of the tetrachotomy method, we consider the following function:

$$f(\alpha) = \frac{g(\alpha)}{(\alpha - \alpha_i)^n}, \tag{1.88}$$

where f is meromorphic in $\mathbb{C} \setminus \{\alpha_i\}$ and α_i are the poles of the f.

In the complex plane defined by ($\alpha_R \in [0,1], \alpha_I \in [0,1]$), we consider twenty five poles α_i randomly chosen (with the function RAND of Matlab) and we apply the algorithm to this function. The results show that the poles found by the program are extremely close to the ones we entered as input data (see Fig. 1.9). The corresponding randomly values are shown in Table 1.1. We also have at least eight identical numbers which is the tolerance number we imposed in our computations. The CPU took around 8 seconds to find these poles.

Re(f)	Re(α_i)	Im(f)	Im(α_i)
0.1201870179870 81	0.1201870196255 25	0.4190482920435 86	0.4190482936248 83
0.5408840812414 76	0.5408840812373 28	0.0641870873888 41	0.0641870873918 99
0.2553867404880 51	0.2553867404862 75	0.5056366175697 18	0.5056366175717 56
0.5464494399030 68	0.5464494399029 04	0.3174278636543 75	0.3174278636558 50
0.0205357746581 85	0.0205357746582 72	0.6356613888613 70	0.6356613888613 77
0.5250451647626 09	0.5250451647628 52	0.3907620822038 25	0.3907620822041 75
0.0365630180484 53	0.0365630180484 48	0.6712021853565 18	0.6712021853565 36
0.5165582083512 70	0.5165582083513 38	0.4400355957603 17	0.4400355957602 54
0.7027023069504 75	0.7027023069507 54	0.2576137367121 09	0.2576137367124 38
0.1535903766194 00	0.1535903766195 46	0.7519463938673 38	0.7519463938674 50
0.6536998890082 53	0.6536998890085 06	0.4439641550183 88	0.4439641550188 10
0.1807377602547 94	0.1807377602547 70	0.8522638903438 52	0.8522638903438 46
0.3258336287632 49	0.3258336287628 24	0.8161401028755 46	0.8161401028753 23
0.1635123685275 26	0.1635123685275 36	0.8667498969993 16	0.8667498969993 19
0.4150933866130 47	0.4150933866131 28	0.7890735149389 85	0.7890735149389 58
0.3988807523831 99	0.3988807523834 32	0.8145397729008 78	0.8145397729006 51
0.9326135720485 64	0.9326135720487 64	0.0600188197792 11	0.0600188197794 76
0.1635699097849 93	0.1635699097841 67	0.9210972558923 83	0.9210972558921 97
0.9534570698862 48	0.9534570698867 28	0.2286694821057 89	0.2286694821055 01
0.7486188717761 97	0.7486188717745 08	0.6420608284372 04	0.6420608284338 52
0.6797338982104 67	0.6797338982104 44	0.7673295107765 02	0.7673295107765 74
0.6659872164111 11	0.6659872164111 21	0.7946578853888 43	0.7946578853887 53
0.8943893753542 43	0.8943893753542 96	0.5773941967065 78	0.5773941967066 49
0.8092038512937 93	0.8092038512948 56	0.7152125147815 98	0.7152125147858 40
0.9236756126204 07	0.9236756126186 13	0.9508944153804 93	0.9508944153781 35

Table 1.1: The real part Re(f) and the imaginary part Im(f) of the poles of the test function f as compared to the calculated poles $\alpha_i = \text{Re}(\alpha_i) + i\text{Im}(\alpha_i)$ with the tetrachotomy method. The agreement is pretty good with at least eight identical numbers for the real and imaginary parts, which is the tolerance number we imposed in our computations.

Chapter 2

Coupling Surface Plasmon Polaritons

Overview Research in plasmonics has gone made very fast progress in the last decades [8, 9, 10, 11, 12, 13]. Since 1990, the study of plasmonic waveguides and plasmonic enhanced (extraordinary) transmission [14] has greatly boosted the exposure of the subject. Plasmonics is a branch of optical condensed matter devoted to optical phenomena at the nanoscale in structured metallic systems, due to modes called surface plasmon polaritons ($SPPs$). $SPPs$, predicted more than 50 years ago by R. H. Ritchie [3] and extensively studied ever since [5, 71], play key roles in today's nanophotonics [29]. They are optical surface waves that propagate (typically) along the metal-dielectric interface. But they are also characterized by a high attenuation due to the intrinsic losses in the metal, limiting the applications [30, 31, 32, 33]. The aim of this chapter is to present the best known way to enhance the surface plasmon emission, which is coupling it with another surface plasmon. It is possible in structures which are composed of a metallic film in a symmetric medium. Indeed, a metallic film supports two SPP that are coupled and the strength of this coupling depends on the metallic thickness. This coupling helps improve the propagation length of surface plasmons. After a reminder of the basic properties of the SPP modes, we present the long range surface plasmon polariton ($LRSPP$) which corresponds to one of the coupled SPP in thin metallic film. It is demonstrated how to obtain this mode on a metallic film deposited on a perfect electric conductor substrate. This possibility allows to not excite the short range surface plasmon polariton ($SRSPP$) mode and to obtain the $LRSPP$ without a symmetric device.

2.1 Surface plasmon polaritons at a single interface

2.1.1 Existence conditions

In order to investigate the physical properties of $SPPs$, we have to begin by the Drude model. This model gives a well known relation between metal permittivity and plasma frequency. It was proposed by Paul Drude in 1900 [72] in order to explain the transport properties of electrons in materials, especially in metals. To describe the optical properties of metals, we can consider a gas made up of free conduction electrons. This free electron gas can collectively oscillate and this longitudinal displacement of the density of charges is called a *plasmon*. Its energy quantum is $\hbar\omega_p$, where ω_p is the plasma frequency:

$$\omega_p = \sqrt{\frac{N_e e^2}{\varepsilon_0 m_e}}, \tag{2.1}$$

where N_e is the electrons' density, e the charge of electrons, ε_0 the dielectric constant of the vacuum and m_e the electron mass. In this work, we apply the kinetic theory. As a consequence, the electron gas is treated as neutral solid spheres. Its motion is uniform rectilinear until collision. The metal is also like a set of conduction electrons which are free to move with these negative charges and relatively immobile positive ions.

The dielectric permittivity ε_m, which is the response of the metal to an excitation with the pulsation ω is given by:

$$\varepsilon_m(\omega) = 1 - \frac{\omega_p^2}{\omega(\omega + i\Gamma)}, \tag{2.2}$$

where Γ is the damping factor (it is used to account for the dissipation of the electron motion) and ω_p the plasma frequency. In the present work, we mostly consider silver metal for computations where $\Gamma = \omega_p/428$ and $\omega_p = 1.374 \times 10^{16}$ s^{-1} [73] [1]. In the case of metal without losses, the dielectric permittivity becomes

[1] A reason for not using gold is that, it was demonstrated for a wavelength $\lambda < 520$ nm that the photons do not transfer their energy to the SPs but to the individual electrons to generate intraband transitions, which cancels the SP resonance [74]. M. Watanabe *et al.* [75] present

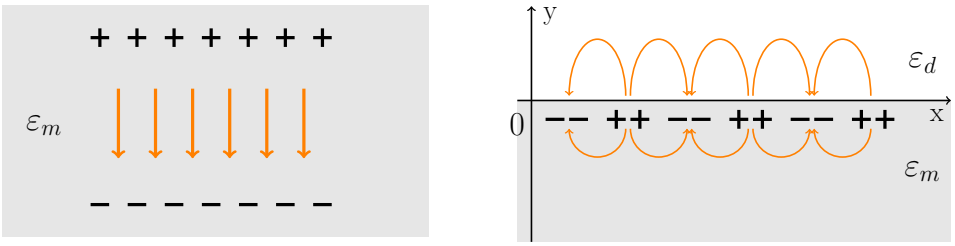

(a) (b)

Figure 2.1: (a) Volume plasmon in a bulk metal with a permittivity ε_m. (b) Surface plasmon at the interface between a dielectric (ε_d) and a metal (ε_m).

$\varepsilon_m(\omega) = 1 - \omega_p^2/\omega^2$.

Two types of plasmons can be distinguished. In bulk metal (Fig. 2.1a), the collective oscillation of the electron gas is called *volume plasmon*, whereas the interface between a metal and a dielectric support is a *surface plasmon* (Fig. 2.1b). Lastly, when the collective oscillation of the electron gas is coupling with light, this mode is called a *surface plasmon polariton* (SPP). In what follows, we will only consider these SPP modes and we can use SP to simplify the notation.

SPs are surface mode solutions of Maxwell's equations with appropriate boundary conditions. We search these solutions at a flat interface between a metal and a dielectric. It is possible to demonstrate that SPs only exist in transverse magnetic (TM) polarization. We consider time harmonic modes with the magnetic field linearly polarized along a direction which is transverse to the direction of propagation z. We denote the magnetic field as $\mathbf{H} = u(x, y)\mathbf{e}_z$ and the time dependence is $e^{-i\omega t}$. The field $u(x, y)$ satisfies the following Helmholtz's equation:

$$\mathrm{div}(\varepsilon_j^{-1}\nabla u) + k_j^2 u = 0, \tag{2.3}$$

where $k_j^2 = k_0^2\varepsilon_j$ is the wave vector in each medium ($j = d, m$). This equation has to be solved separately in regions of constant ε_j. The solutions obtained have to be matched using appropriate boundary conditions. We note ε_m for $y < 0$ and ε_d for $y > 0$, the permittivities of the metal and the dielectric respectively. α and $\tilde{\beta}_j$

this as "anomalous reflection of gold" because below this wavelength, the gold loses its metallic properties of reflectivity.

$(j = d, m)$ are the wave vectors in the x and the y directions.

We note $u(x, y) = e^{i\alpha x}U(y)$ and the field $U(y)$ satisfied the following equations:

$$\begin{aligned} y > 0\text{: } & \frac{\partial^2 U}{\partial y^2} + (k_d^2 - \alpha^2)U = 0, \\ y < 0\text{: } & \frac{\partial^2 U}{\partial y^2} + (k_m^2 - \alpha^2)U = 0. \end{aligned} \tag{2.4}$$

The solutions are:

$$\begin{aligned} y > 0\text{: } & U(y) = a_1 e^{-i\tilde{\beta_d} y} + b_1 e^{i\tilde{\beta_d} y}, \\ y < 0\text{: } & U(y) = a_2 e^{-i\tilde{\beta_m} y} + b_2 e^{i\tilde{\beta_m} y}, \end{aligned} \tag{2.5}$$

where $\tilde{\beta_j}$ $(j = d, m)$ are defined by the relation $\alpha^2 + \tilde{\beta_j}^2 = k_0^2 \varepsilon_j$.

The solution corresponding to surface waves along the x direction imposes that the field is evanescent along the y direction so that β_j must be imaginary. We have $\mid \alpha \mid > k_0\sqrt{\varepsilon_j}$ and $\tilde{\beta_j}$ are written as:

$$\tilde{\beta_j} = i\sqrt{\alpha^2 - k_0^2 \varepsilon_j}. \tag{2.6}$$

We note $\tilde{\beta_j} = i\beta_j$. However, we must impose $a_1 = 0$ and $b_2 = 0$ (as the modes are bound to the surface, they must decay with increasing/decreasing y) and the field is rewritten as:

$$\begin{aligned} y > 0\text{: } & U(y) = b_1 e^{-\beta_d y}, \\ y < 0\text{: } & U(y) = a_2 e^{\beta_m y}. \end{aligned} \tag{2.7}$$

At $y = 0$, U and $\varepsilon_j^{-1}\partial_y U$ must be conserved in the TM polarization:

$$\begin{aligned} b_1 &= a_2, \\ -\frac{\beta_d}{\varepsilon_d} b_1 &= \frac{\beta_m}{\varepsilon_m} a_2. \end{aligned} \tag{2.8}$$

To obtain the solution, we can solve the system of Eq. 2.8 or consider the cancellation of the coefficient of reflection's denominator. The result must be the

same:

$$\frac{\tilde{\beta_d}}{\varepsilon_d} + \frac{\tilde{\beta_m}}{\varepsilon_m} = 0. \tag{2.9}$$

And the corresponding dispersion relation for the SP is:

$$k_{SP} = \pm k_0 \sqrt{\frac{\varepsilon_d \varepsilon_m}{\varepsilon_d + \varepsilon_m}}, \tag{2.10}$$

where k_{SP} is the corresponding in-plane wave vector (propagation constant) α for the surface plasmon.

In the case of a real metal (with losses), k_{SP} and necessarily β_m and β_d are complex, which implies a sinusoidal supplementary component (along the y direction) to the evanescent envelope of the field. We note $\varepsilon_m = \varepsilon_m^{'} + i\varepsilon_m^{''}$. With the convention of signs in the exponents and to verify Eq. 2.9, the real part dielectric permittivities $\varepsilon_m^{'}$ and ε_d must have opposite signs. Since dielectrics have a positive (and real) ε_d, that means ε_m must be negative. In addition, the real part of the dispersion relation (Eq. 2.10) involves a supplementary condition: the propagation along x is only possible through the existence of a real part for k_{SP}. These two conditions imply $\varepsilon_m^{'} > -1$ [5].

These conditions are largely fulfilled by several metals in the visible and near-infrared ranges of the spectrum. In these ranges, ε_m for silver has a large negative real part and a small positive imaginary part associated to the absorption and the scattering losses in the metal.

2.1.2 The dispersion relation

To properly understand SP modes, we have to examine the corresponding dispersion relation, the relationship between the frequency ω and the in-plane wave vector α. The in-plane wave vector is the wave vector of the mode in the plane of the surface along which it propagates. For light in free space, the wave vector is given by $k_0 = \omega/c$ (the light line), c being the speed of light. In a medium with the dielectric permittivity ε_d, the dispersion relation becomes $k = \sqrt{\varepsilon_d} k_0$. Lastly, for SPs propagating along the interface between a metal and a dielectric, the dispersion relation (Eq. 2.10) is found by looking for the surface mode solutions of Maxwell's equations in the section 2.1.1.

Fig. 2.2a illustrates an interface between air ($\varepsilon_d = 1$) and a metal (ε_m). By

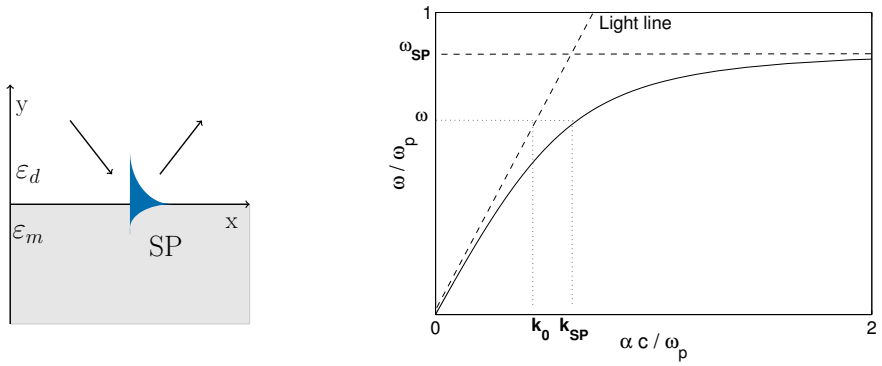

(a) (b)

Figure 2.2: (a) Single plane interface between a dielectric ($\varepsilon_d = 1$) and a metal (ε_m) which supports a SP. (b) The dispersion relation, found by taking the real part of Eq. 2.10 with the metallic permittivity based on the Drude model (Eq. 2.2) and the plasma frequency ω_p for silver. The constant of propagation α is plotted in units of ω_p/c and the frequency ω in units of ω_p. The light line is the dispersion line for light in free space, $k_0 = \omega/c$. The asymptotic surface plasmon frequency corresponds to $\omega_{SP} = \omega_p/\sqrt{1+\varepsilon_d}$. The dispersion curve for a SP mode shows the momentum mismatch problem: the SP mode is always lying beyond the light line because its wave vector k_{SP} is greater than the wave vector of a free space photon k_0 at a given frequency ω. It is a non-radiative mode.

substituting the expression of ε_m by the dielectric permittivity of silver based on the Drude model (Eq. 2.2), and by taking the real part of Eq. 2.10, we can plot the corresponding dispersion relation (Fig. 2.2b).

Fig. 2.2b illustrates the dispersion curve of the SP modes. At low frequencies, the dispersion curve lies very close to the light line, also said to be light-like. It is a region where this mode is best described as a polariton. Then, the frequency rises and the mode moves further away from the light line, approaching gradually an asymptotic limit, the surface plasmon resonant frequency $\omega_{SP} = \omega_p/\sqrt{1+\varepsilon_d}$ which translates in term of frequencies the condition $\varepsilon_m^{'} > -1$. This occurs when the permittivity of the metal and of the dielectric are of the same magnitude (but opposite sign), which is producing a pole in the dispersion relation.

By definition, for propagating waves (PW), $k_{PW} < k_0 = \omega/c$ (these waves have a dispersion relation above the light line) when for SP modes, $k_{SP} > k_0$. The wave vector corresponding to SP mode is always higher than the light line. We also say that the SP is a non-radiative mode. This is the evanescent behavior of these surface modes that forbids a direct excitation with a propagating electromagnetic

wave. A photon and a SP at the same energy level, never have the same quantity of motion.

There are two distinct ways to excite SP modes: with high energy electrons [76] or with electromagnetic waves. We will only consider the use of electromagnetic waves. In this case, classical techniques used to excite SP modes employ diffraction by gratings or attenuated total reflection (ATR). In this work, we will consider SPs supported by silver films and excited by electromagnetic waves using the ATR in the Kretschmann configuration [5], which will be presented in section 2.3.1.

2.1.3 SP length scales

The first important length characterizing the SP is its wavelength λ_{SP}, which corresponds to the period of the surface charge density oscillation and the field distribution of the mode. The wavelength λ_{SP} comes from the real part of the complex dispersion relation $k_{SP}^{'}$ (Eq. 2.10):

$$\lambda_{SP} = \frac{2\pi}{k_{SP}^{'}} = \lambda_0 \sqrt{\frac{\varepsilon_d + \varepsilon_m^{'}}{\varepsilon_d \varepsilon_m^{'}}}, \tag{2.11}$$

where λ_0 is the free space wavelength.

This SP wavelength is very similar, but always less than the free space wavelength λ_0. The fact that $\lambda_{SP} < \lambda_0$ is a consequence of the bound nature of the SP modes.

The propagation length

The propagation length δ_{SP} of the SP mode corresponds to the extension in the x-direction of the field along the surface [77, 78, 79]. It is defined by the distance over which the intensity of the mode decreases to $1/e$ of its initial value [80]. It is given by $\delta_{SP} = 1/2k_{SP}^{''}$. The imaginary part $k_{SP}^{''}$ is:

$$k_{SP}^{''} = k_0 \frac{\varepsilon_m^{''}}{2(\varepsilon_m^{'})^2} \left(\frac{\varepsilon_m^{'} \varepsilon_d}{\varepsilon_m^{'} + \varepsilon_d} \right)^{\frac{3}{2}}. \tag{2.12}$$

So then:

$$\delta_{SP} = \lambda_0 \frac{(\varepsilon_m^{'})^2}{2\pi \varepsilon_m^{''}} \left(\frac{\varepsilon_m^{'} + \varepsilon_d}{\varepsilon_m^{'} \varepsilon_d} \right)^{\frac{3}{2}}. \tag{2.13}$$

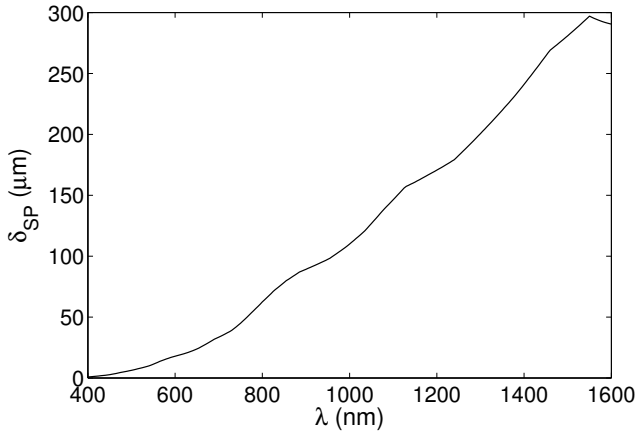

Figure 2.3: The SP propagation length δ_{SP} as a function of the free space wavelength λ which varies from visible to near-infrared range. The metal considered is silver, based on the Palik data [81] and the dielectric is air, $\varepsilon_d = 1$.

The SP propagation length δ_{SP} as a function of the free space wavelength is plotted in Fig. 2.3. The dielectric permittivity of the metal ε_m is taken from the Palik data set [81] (experimental data) for silver. This choice will be justified in Section 2.2. The increase of the propagation length is explained by the fact that for longer wavelengths, the metal becomes a better conductor. The SP wave vector is closer to the free space wave vector and, as it is shown with the dispersion curve, the mode is thus light-like. Consequently, the mode is less confined to the surface.

Furthermore, it is possible to approximate the propagation length when using low loss metal and when the condition $\mid \varepsilon_m^{'} \mid > \varepsilon_d$ is satisfied:

$$\delta_{SP} \approx \lambda_0 \frac{(\varepsilon_m^{'})^2}{2\pi\varepsilon_m^{''}}. \tag{2.14}$$

With this approximation, we can see that to have a much higher propagation length δ_{SP}, we need a large (negative) real part $\varepsilon_m^{'}$ and a small imaginary part $\varepsilon_m^{''}$. In the visible and near-infrared ranges, silver respects these properties.

The penetration depths

By definition, the penetration depths of a surface mode correspond to the spatial (vertical) extension of its field in both media in the y-direction [82]. For a material with a dielectric permittivity ε_i $(i = d, m)$, it is possible to express the total wave

vector with its components in the plane (the wave propagates in the y-direction):

$$\varepsilon_i k_0^2 = k_x^2 + k_y^2, \tag{2.15}$$

where k_0 is the wave vector for free space, k_x is the in-plane component and k_y is the perpendicular component to the plane.

If we consider now the particular case of surface plasmons, the in-plane wave vector k_x corresponds to k_{SP} (Eq. 2.10). Or as we noted, the SP wave vector always exceeds the wave vector of a photon in the adjacent medium, $k_{SP}^2 > \varepsilon_i k_0^2$. For this reason, the y-component of the wave vector in both media must be imaginary, and thus represent the exponential decay of the fields with distance into both media (Fig. 2.4).

From the dispersion relation (Eq. 2.10 with Eq. 2.15), the penetration depths δ_d and δ_m into the dielectric and the metal respectively can be written as:

$$\delta_d = \frac{1}{k_0}\sqrt{\frac{\mid \varepsilon_m^{'} + \varepsilon_d \mid}{\varepsilon_d^2}}, \tag{2.16}$$

$$\delta_m = \frac{1}{k_0}\sqrt{\frac{\mid \varepsilon_m^{'} + \varepsilon_d \mid}{(\varepsilon_m^{'})^2}}, \tag{2.17}$$

with the condition $\mid \varepsilon_m^{'} \mid >> \mid \varepsilon_m^{''} \mid$.

Fig. 2.5a illustrates the SP penetration depth into the dielectric δ_d (with $\varepsilon_d = 1$) plotted as a function of the wavelength. In the visible spectrum, δ_d is less than the free space wavelength; when in the near-infrared spectrum, it becomes more than it. The increase of the penetration depth is again explained by the fact that for longer wavelength, the metal becomes a better conductor and the mode is thus light-like.

The distance below the decay rate of molecules is enhanced by SP modes [83, 24] and is linked to δ_d. In many cases, this mode of decay is undesirable, as in the case in diodes where the efficiency can be reduced by the presence of metallic electrical contacts. To overcome this drawback, solutions such as the nanostructuring of the device have been studied [84].

The SP penetration depth into the metal, δ_m, as a function of the wavelength is plotted in Fig. 2.5b. This penetration depth is largely independent of the free

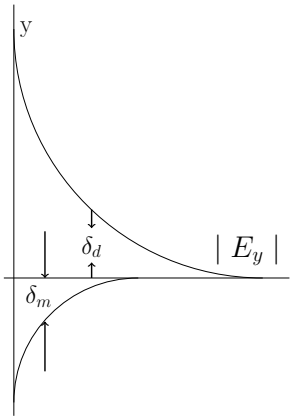

Figure 2.4: The field in the perpendicular direction is evanescent, reflecting the bound, non-radiative nature of SPs. This prevents power from propagating away from the surface. In the dielectric medium (typically air or glass), the penetration depth is δ_d, whereas the penetration length into the metal is δ_m.

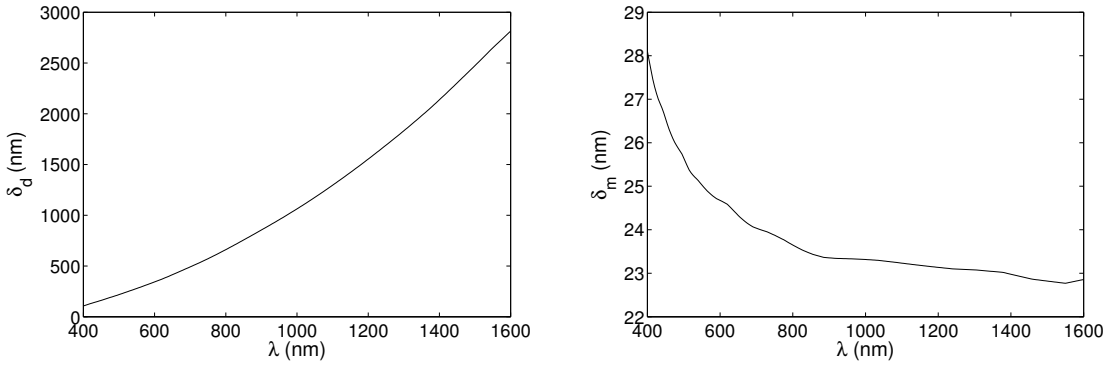

(a) (b)

Figure 2.5: The SP penetration depths as a function of the free space wavelength λ which varies from visible to near-infrared range. The metal considered is silver, based on the Palik data [81] and the dielectric is air, $\varepsilon_d = 1$. (a) The SP penetration depth into the dielectric δ_d. (b) The SP penetration depth into the metal δ_d.

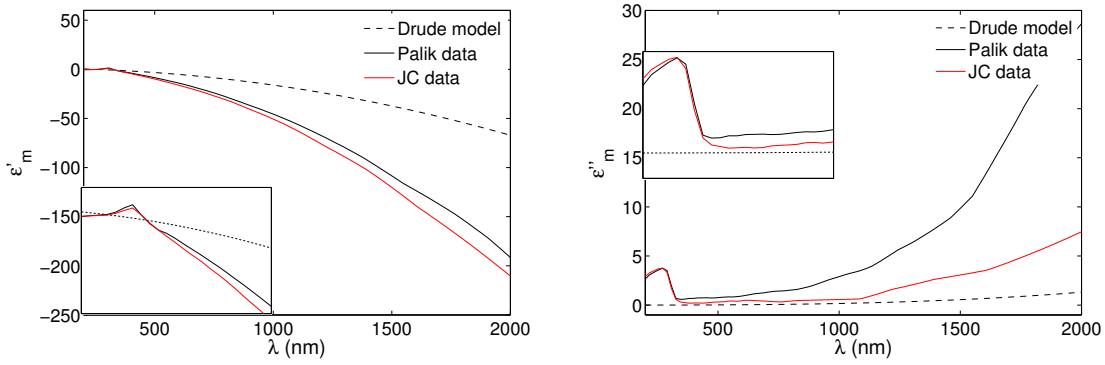

(a) (b)

Figure 2.6: The real (a) and imaginary (b) parts of the silver dielectric permittivity $\varepsilon_m(\omega) = \varepsilon_m^{'}(\omega) + \varepsilon_m^{''}(\omega)$ using the Drude model (gray dashed line), the Palik data [81] (black line) and the Johnson and Christy data [85] (red line). A zoom is made on the region of wavelengths between 200 nm and 600 nm.

space wavelength in this wavelength range. Indeed, in this range $\omega << \omega_p$ and we can approximate δ_m as:

$$\delta_m = \frac{\lambda_p}{2\pi}, \tag{2.18}$$

where λ_p is the wavelength corresponding to the plasma frequency ω_p. For silver, $\omega_p = 1.374 \times 10^{16}\ s^{-1}$ and the penetration depth in the metal is $\delta_m = 22$ nm, which is not so far from the average value in Fig. 2.5b. Note that the penetration depth rises for short wavelengths because the condition $\omega << \omega_p$ is no longer valid.

The parameter δ_m represents the necessary thickness for the metallic films that allows the coupling of a SP mode, as with propagating light in the prism coupling configuration (Kretschmann) or with another SP modes in a metallic thin film device.

2.2 Dielectric permittivity of metals

The Drude model presented in Section 2.1.1 allows to obtain the main properties of surface plasmons. However, it gives only an approximation of the dielectric permittivity of metals, and its validity is limited to near-infrared frequencies. We are going to compare it to experimentally determined dielectric permittivity of silver, as adopted from Johnson and Christy [85] and Palik [81] data sets.

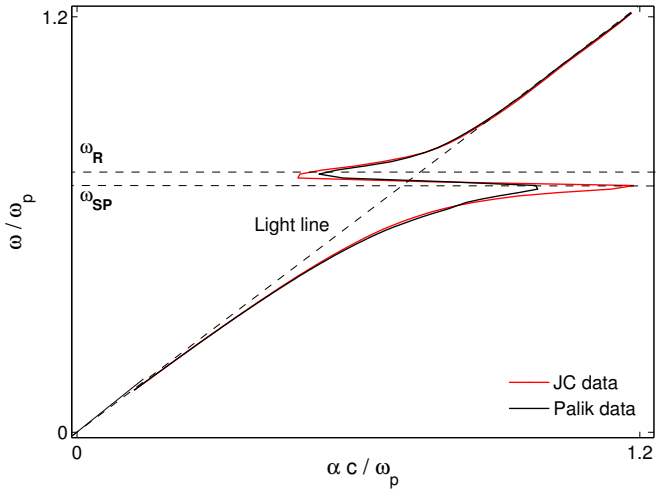

Figure 2.7: Dispersion relation of SP mode on the Ag/air interface with respectively the permittivities ε_m and $\varepsilon_d = 1$. The metal permittivity ε_m is determined from the Palik (black line) and the Johnson and Christy (red line) data sets. For frequencies below $\omega_{SP} = \omega_p/\sqrt{1+\varepsilon_d}$, the typical bound SP mode is observed below the light line plotted in dashed line (as in Fig. 2.2b). Above the asymptote at ω_R, there is the radiative plasmon polariton (RPP) mode. Between these two asymptotes, it is the plasmon bandgap where the plasmon wave vector is purely imaginary and the modes in this regime (called quasibound modes) are forbidden [86].

Fig. 2.6 shows the dielectric permittivity $\varepsilon_m(\omega) = \varepsilon_m^{'}(\omega) + i\varepsilon_m^{''}(\omega)$ of silver as derived from the Johnson and Christy (JC) data, the Palik data and the Drude model (Eq. 2.2). The JC and Palik data sets are in agreement for wavelengths between 200 nm and 600 nm. At greater wavelengths, $\varepsilon_m^{'}$ from JC data falls off faster and $\varepsilon_m^{''}$ grows more slowly than the corresponding results from the Palik data. With this difference, we have to compare the results of both data sets on a practical case, the dispersion relation of SP.

The dispersion curve of a SP supported at the interface between air ($\varepsilon_d = 1$) and a metal (ε_m) is presented in Fig. 2.7, both for the JC and the Palik data sets. As there are experimental results, the asymptote at $\omega_{SP} = \omega_p/\sqrt{1+\varepsilon_d}$ (defined by the wavelength where $\varepsilon_m^{'} = -\varepsilon_d$) does not go to infinity. Note here that ω_p is not well defined with its asymptote, an uncertainty still exists. For frequencies below this asymptote, the typical bound SP mode is observed (as in Fig. 2.2b). Above the asymptote at ω_R, there is the radiative plasmon polariton (RPP) mode. Between these two asymptotes, we have the plasmon bandgap where the plasmon wave vector is purely imaginary and the modes in this regime (called quasibound

modes) are forbidden [86]. The agreement between the two curves from JC and Palik data sets is satisfactory. We also chose to use the Palik data on silver in all computations unless otherwise specified.

2.3 Metallic film in non-symmetric medium

In this section, we will describe the properties of the surface plasmons supported by a metallic film in a non-symmetric medium. It is the most commonly used configuration to excite and exploit SPs. To begin, the optical methods used to excite them shall be detailed. Afterwards, two well known figures of merit of the surface plasmons will be presented: the characterized dip of reflectivity on the metallic surface for a specific angle of incidence; and the map of the magnetic field corresponding to the surface plasmon (in the transmitted medium).

2.3.1 Optical coupling of SPs

As we saw in the first section, SP modes are non-radiative modes. To couple these modes with light waves, special devices must to be employed [87]. Indeed, the coupling can be achieved using a coupling medium, such as a grating or a prism, to match the photon and surface plasmon wave vectors. A grating coupler matches the wave vectors by increasing the parallel wave vector component by an amount related to the grating period. A prism can be positioned very close to a metal surface in the Otto configuration or against a thin metallic film in the Kretschmann configuration. We will give more precisions for both of these methods.

Metallic gratings

Metallic gratings can be used to satisfy the energy and momentum matching conditions of the wave vectors. We consider an incident wave vector $k_i = k_0\sqrt{\varepsilon_i}$ with k_i^x its in-plane component and θ_i the incident angle of this wave. We recall that to excite a plasmon, we have to satisfy the condition:

$$k_i^x = k_{SP}(\omega). \tag{2.19}$$

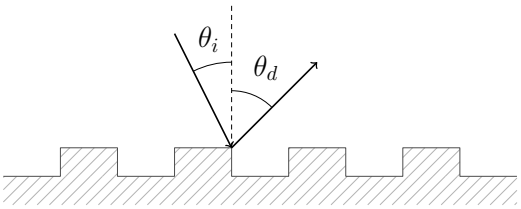

Figure 2.8: A metallic grating constituted by a periodic structure with a period Λ.

However, $k_i^x = \omega/c \sin\theta_i < \omega/c$ and $\omega/c <\mid k_{SP}(\omega) \mid$. A possibility for obtaining the equality 2.19 is to use the grating coupling [5].

A grating is a periodically corrugated surface modulation. It can be characterized by its periodicity or grating constant Λ. The periodic corrugation breaks the translational invariance of the metal surface. An incident plane wave can interact with the grating grooves, acting as an array of scattering centres. The total field can be generated from the constructive interference of the individual scattered waves, resulting in different diffraction orders. We consider a grating constituted by a periodic structure with a period Λ (Fig. 2.8). The wave vectors are equal modulo $2\pi/\Lambda$ (as a consequence of the Bloch theorem) and we can write:

$$k_0 \sin\theta_d = k_0 \sin\theta_i + p\frac{2\pi}{\Lambda}, \tag{2.20}$$

where $k_0 = \omega/c$ and p is a relative integer and represents the order of diffraction. It is always possible to find an order p where:

$$k_{SP}(\omega) = k_i^x + p\frac{2\pi}{\Lambda}. \tag{2.21}$$

It becomes possible to excite a SP with an incident electromagnetic plane wave. In this configuration, we have a total absorption: for a given frequency ω, we can find an incident angle θ_i which respects the condition 2.21 and the corresponding wave vector $k_i^x = \omega/c \sin\theta_i$ can match with k_{SP}. It is this method that was used in the first - accidental - observation of the SPs, and that is reported in [2] as Wood's anomalies. Indeed, in 1902, R. W. Wood observed sudden variations of the intensity in the light beam spectrum, reflected by a diffraction grating in the TM

polarization. The intensity of the incident beam being continuous, the spectrum had to be continuous too. These variations are due to the coupling between the propagating incident waves and the SP waves. Following this, gratings have been much studied by A. Hessel and A. A. Oliner [88], and more precisions are given by R. Petit [89] and H. Raether [5].

It is also possible to excite the SP mode with a high refractive index prism, as we are going to present.

Otto configuration

Two configurations are possible to excite SPs optically by employing a high refractive index prism. In the Otto configuration [5] (Fig. 2.9a), an incident beam is reflected on the base of a prism of high refractive index material ($\varepsilon_d > 1$). Near to the base, there is a gap of low refractive index material (we take $\varepsilon_a = 1$), with a thickness on the order of the incident beam wavelength [5, 90]. On the other side of the gap, there is a metallic film (ε_m). The ATR takes place when the incident angle θ_i is equal to, or larger than, the critical angle and creates an evanescent field. In the prism with a permittivity ε_d (we take glass, $\varepsilon_d = 2.25$), the in-plane component of the incident wave vector is $k_i^x = \sqrt{\varepsilon_d}\sin\theta_i$. It can be higher than k_0 because $\varepsilon_d > \varepsilon_a$. In these conditions, the incident wave can excite the SP modes on the air/metal interface. We plot the reflectivity as a function of the incident angle θ_i (Fig. 2.9b), and the coupling condition appears as a minimum of the reflectivity for $\theta_i = 43.7°$. This dip of the reflectivity represents the excitation on the SP mode.

This excitation is very sensitive to changes in the gap between the dielectric prism and the metallic film, which explains why the method is rather unused today.

Kretschmann configuration

The Kretschmann configuration [5] is the most commonly used method to couple light to surface plasmons because of its relative simplicity and robustness. As illustrated in Fig. 2.10a, an incident beam is reflected on the base of a high refractive index prism ($\varepsilon_d > 1$). A thin metallic film is located on the prism base. The thickness of the metal layer needs to be precisely controlled in order to obtain the most efficient coupling. Again, there is an ATR when the incident angle θ_i is

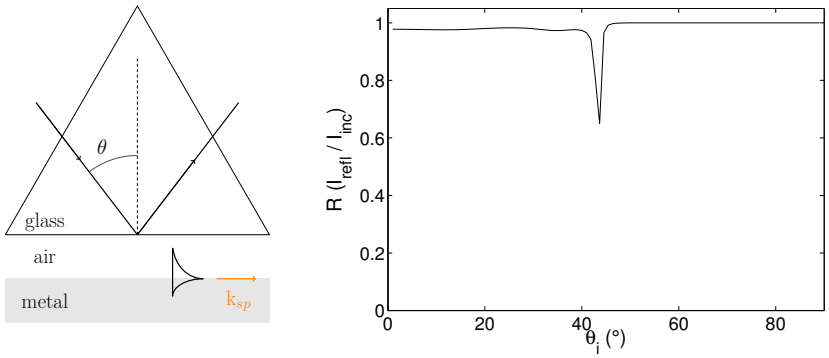

(a) (b)

Figure 2.9: (a) Prism coupling in the Otto configuration with the permittivities $\varepsilon_d = 2.25$ (glass), $\varepsilon_a = 1$ (air) and ε_m (metal), taken from the Palik data [81] for silver. (b) The reflectivity is plotted as a function of the incident angle θ_i, with a wavelength $\lambda = 632.8$ nm. The minimum of reflectivity occurs for an angle $\theta_i = 43.7°$, and corresponds to the excitation of the SP when the thickness of the spacer is on the order of the incident wavelength.

equal to, or larger than, the critical angle and creates an evanescent field.

The in-plane component of the incident wave vector k_i^x can be higher than k_0. In Fig. 2.10b, reflectivity is plotted as a function of the incident angle θ_i. Three cases are distinguished. The first extreme case, when there is no metallic film (in red), represent the total internal reflection of the field between the media with $\varepsilon_d = 2.25$ and $\varepsilon_a = 1$. The second case (in blue) corresponds to the situation where the metallic film is too thick (as a metallic bulk). The layer becomes opaque to the electromagnetic field and the system is like a mirror. The corresponding reflection is still high, but lower than 1 because of the metal absorption. Finally, when the metallic film thickness is $e_m = 45$ nm for $\lambda = 632.8$ nm, the coupling of the SP mode occurs for an angle $\theta_i = 43.7°$C.

The choice of the metallic film thickness occurs from the plot of the minimum reflectivity obtained as a function of the metallic thickness e_m (Fig. 2.12). The minimum occurs for $e_m = 45$ nm.

So, it is possible to match the propagating wave vector k_i^x with the wave vector k_{SP} corresponding to the interface metal/air (Fig. 2.11). The propagating electromagnetic wave in the dielectric is also able to excite SP modes which propagate in the air. An important point here is that a metallic film supports two plasmons. In the present case, there is a plasmon at the metal/air interface and

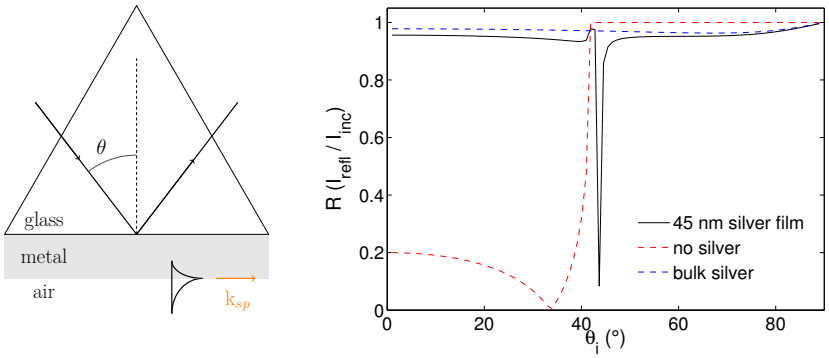

(a) (b)

Figure 2.10: (a) Prism coupling in the Kretschmann configuration with the permittivities $\varepsilon_d = 2.25$ (glass), $\varepsilon_a = 1$ (air) and ε_m (metal), taken from the Palik data [81] for silver. (b) Reflectivity plotted as a function of the incident angle θ_i with a wavelength $\lambda = 632.8$ nm. The minimum of reflectivity occurs for an angle $\theta_i = 43.7°$ and corresponds to the excitation of the SP when $e_m = 45$ nm. The red curve represents the case where there is no metallic film, the incident beam is reflected on the base of the prism towards the air. Because $\varepsilon_d > \varepsilon_a$, that is the classical case of total internal reflection. The blue curve represents the case where the metallic film is as a metal bulk. The system becomes like a mirror and it is impossible to excite the SP mode.

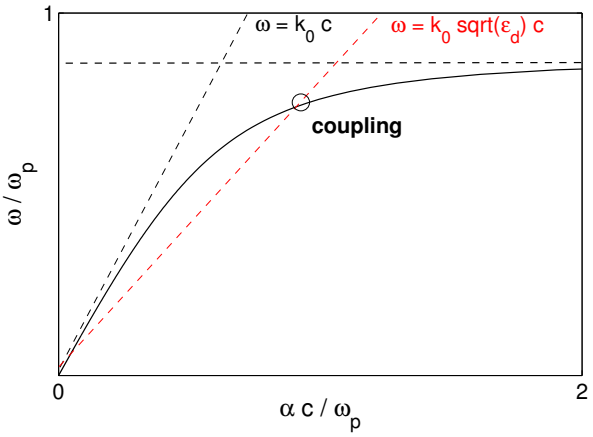

Figure 2.11: For light wave in vacuum, $\omega = k_0 c$, when in dielectric medium ($\varepsilon_d > 1$), $\omega = k_0\sqrt{\varepsilon_d}c = k_i^x c$. The in-plane component of the incident wave vector can be higher than k_0. There is a frequency for which $k_i^x = k_{SP}$ and the coupling between light wave and the SP mode, which exists at the interface metal/air becomes possible.

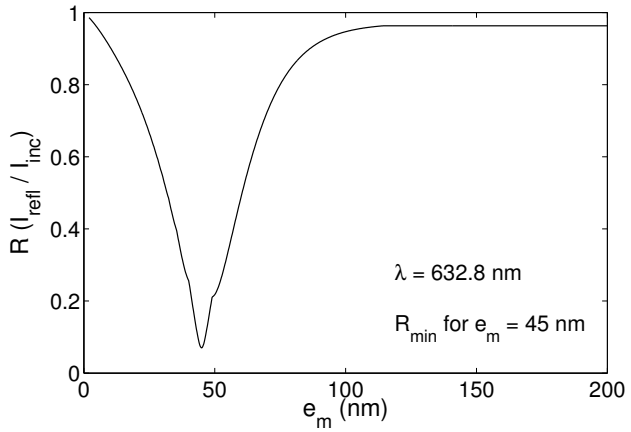

Figure 2.12: The reflectivity plotted as a function of the metallic thickness e_m at a wavelength $\lambda = 632.8$ nm for the structure of Fig. 2.10a. The minimum occurs for a thickness $e_m = 45$ nm.

another one at the dielectric/metal interface. This method of excitation allows the excitation of the plasmon at the metal/air interface, the other having again a too high propagation constant.

2.3.2 ATR configuration

The classical ATR configuration also corresponds to the Kretschmann configuration. We consider a metallic film, with a thickness e_m and a permittivity ε_m, embedded between two dielectric media with the permittivities ε_d and ε_a (Fig. 2.13). This film supports two SPs, one on the d/m interface and another on the m/a interface.

The more immediate way to determine the solutions is to consider the cancellation of the denominator of the coefficient of reflection r. We recall that the dispersion relation is given by $\alpha^2 + \beta_j^2 = k_0^2 \varepsilon_j$, $j = d, m$. We consider the TM-polarization and the time dependence $\exp(-i\omega t)$. The magnetic field can be written as $H(x, y) = [a_1 e^{-\beta_d y} + b_1 e^{\beta_d y}] e^{i\alpha x}$. By definition, the coefficient of reflection r is defined by $r = b_1/a_1$. It can also be written as:

$$r = \frac{r_{dm} + r_{ma} e^{2\beta_m e_m}}{1 + r_{dm} r_{ma} e^{2\beta_m e_m}}, \tag{2.22}$$

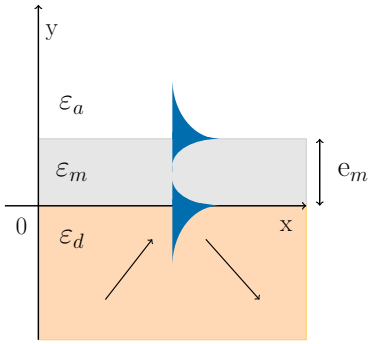

Figure 2.13: Silver film with a thickness e_m and a permittivity ε_m embedded between two dielectric media with the permittivities ε_d and ε_a. For computations, $\varepsilon_d = 2.25$, $\varepsilon_a = 1$, ε_m is taken from the Palik data [81], $e_m = 45$ nm and the incident wavelength is $\lambda = 632.8$ nm.

where:

$$r_{dm} = \frac{\frac{\beta_d}{\varepsilon_d} - \frac{\beta_m}{\varepsilon_m}}{\frac{\beta_d}{\varepsilon_d} + \frac{\beta_m}{\varepsilon_m}} \text{ and } r_{ma} = \frac{\frac{\beta_m}{\varepsilon_m} - \frac{\beta_a}{\varepsilon_a}}{\frac{\beta_m}{\varepsilon_m} + \frac{\beta_a}{\varepsilon_a}}. \tag{2.23}$$

A mode in this structure is defined by the existence of an outgoing field in absence of excitation. That means $b_1 \neq 0$, $a_1 = 0$ and corresponds to the equation $1 + r_{dm} r_{ma} e^{2\beta_m e_m} = 0$:

$$\left(\frac{\beta_d}{\varepsilon_d} + \frac{\beta_m}{\varepsilon_m}\right)\left(\frac{\beta_m}{\varepsilon_m} + \frac{\beta_a}{\varepsilon_a}\right) + \left(\frac{\beta_d}{\varepsilon_d} - \frac{\beta_m}{\varepsilon_m}\right)\left(\frac{\beta_m}{\varepsilon_m} - \frac{\beta_a}{\varepsilon_a}\right) e^{2\beta_m e_m} = 0. \tag{2.24}$$

In the case of a thick metallic film, the term of propagation becomes negligible, $|\exp(2\beta_m e_m)| << 1$ and Eq. 2.24 is simplified:

$$\left(\frac{\beta_d}{\varepsilon_d} + \frac{\beta_m}{\varepsilon_m}\right)\left(\frac{\beta_m}{\varepsilon_m} + \frac{\beta_a}{\varepsilon_a}\right) = 0. \tag{2.25}$$

Eq. 2.25 admits two solutions which correspond to SPs propagating without coupling along the d/m and m/a interfaces as the solution given by Eq. 2.9.

We consider now the case of a thin metallic film which corresponds to the Kretschmann configuration (section 2.3.1). In this case, $\varepsilon_d > \varepsilon_a$, and the metallic thickness is $e_m = 45$ nm for an incident beam with a wavelength $\lambda = 632.8$ nm (Fig 2.13). The modes propagating along each interface have different velocity and

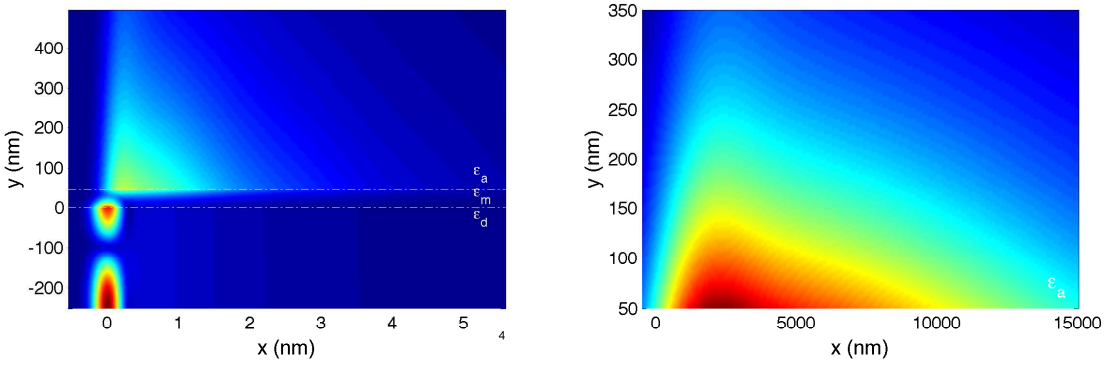

(a) (b)

Figure 2.14: (a) Map of the magnetic field in the structure corresponding to the Kretschmann configuration (Fig. 2.13) with $\varepsilon_d = 2.25$, $\varepsilon_a = 1$ and ε_m is taken from the Palik data [81] for silver. (b) Precise map of the transmitted magnetic field: the SP mode is excited and we can see its propagation length, as well as the exponential decay of the field in the air.

decay rates. An incident beam in the dielectric, with the angle $\theta_i = 43.7°$, allows the excitation of the surface plasmon in the air (Fig. 2.14a).

In Fig. 2.14b, the SP mode is very visible with its propagation length and the exponential decay of the field in the air. From Eq. 2.3, the propagation length is $\delta_{SP} \simeq 21\mu$m, and the corresponding propagation length from the map of the magnetic field is $\delta_{SP} \simeq 14\mu$m (see Fig. 2.14b). The calculated penetration depth (Eqs. 2.5a and 2.5b) are $\delta_{air} = 388$ nm and $\delta_m = 24.5$ nm, which are in agreement with the magnetic field map.

2.4 Metallic film in symmetric media

In this section, we will consider the case of a metallic film in a symmetric medium. For thin metallic film, the properties of the two coupled SP modes supported by the structure are presented. The involvement of the long range SP ($LRSP$) is explained through a review about it and the comparison between the length scales of this mode and the classical SP mode is made.

2.4.1 The dispersion relations

One way to extend the length scale of SP modes is to make use of the coupled SP modes supported by symmetrically thin metallic films [36]. When the metal is thin enough, the SP modes associated to the two metal surfaces may interact and form two coupled SP modes.

For a metallic film in a symmetric medium, $\varepsilon_d = \varepsilon_a$ and Eq. 2.24 is simplified as:

$$\left(\frac{\beta_m}{\varepsilon_m} + \frac{\beta_d}{\varepsilon_d}\right) \pm \left(\frac{\beta_m}{\varepsilon_m} - \frac{\beta_d}{\varepsilon_d}\right) e^{\beta_m e_m} = 0. \tag{2.26}$$

There are two solutions for guiding modes by the metallic film depending on the sign " $\pm$ " in Eq. 2.26. These solutions correspond to the dispersion relations:

$$\omega^+ \colon \beta_d \varepsilon_m + \beta_m \varepsilon_d \tanh\left(\frac{\beta_m e_m}{2}\right) = 0, \tag{2.27}$$

$$\omega^- \colon \beta_d \varepsilon_m + \beta_m \varepsilon_d \coth\left(\frac{\beta_m e_m}{2}\right) = 0. \tag{2.28}$$

In a symmetric medium, the SP frequency is the same on both sides of the metallic film, so that in the case of a thin film (below 50 nm [91]) the electromagnetic fields of both surfaces interact and the frequency splits into a low-frequency ω^- and a high frequency ω^+. The splitting is associated with asymmetric (ω^-) and symmetric (ω^+) electric field E_y distributions, as compared to the symmetry of the structure. For ω^-, the electric field is not cancelled in the metal, which increases absorption due to the losses in the metal. It attenuates rapidly during the propagation (Fig. 2.15a). This asymmetric mode is also called the short range surface plasmon polariton ($SRSP$). For ω^+, the electric field is cancelled in the metal, and the mode has a long propagation length as compared to the SP mode supported by a bulk metallic surface. Indeed, the electric field of these modes has a bigger depth penetration in the dielectric, and the losses by absorption in the metal decrease (Fig. 2.15b). This symmetric surface plasmon mode is called a long range surface plasmon polariton ($LRSP$).

There is a compromise between the propagation length and the penetration depth in a symmetric structure. It is possible to obtain high propagation length in comparison to the case of the single interface but at the expense of the penetration depth. The $LRSP$ mode that propagates very far will not still remain, a surface

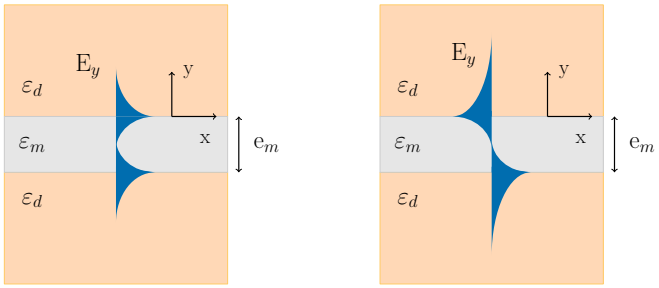

(a) (b)

Figure 2.15: (a) Symmetric electric field E_y corresponding to the $LRSP$. (b) Asymmetric electric field E_y corresponding to the $SRSP$.

mode if the the metallic film becomes too thin.

Fig. 2.16a represents the dispersion curves ω^+ and ω^- of the $LRSP$ and the $SRSP$ modes, respectively. These dispersion curves are obtained with the tetrachotomy method (see Chapter 1) for which the real part of the poles is noted α and corresponds to the propagation constant of the modes. Solutions for Eq. 2.26 are found for a silver film embedded in air. Palik data for silver is used for the metal. In the same conditions, the reflectivity is plotted as a function of the incident angle θ_i (Fig. 2.16b). The half-width of the mode ω^+ is smaller than the half-width of the mode ω^-. Thus, the absorption of the $LRSP$ mode is smaller than that of the $SRSP$ mode.

2.4.2 Review on LRSPs

In a symmetric structure, the most interesting surface mode supported by a metallic film in a symmetric media is the $LRSP$ mode because of its low absorption in comparison to the $SRSP$ mode.

The first theoretical study on the existence of the $LRSPs$ was done in the 1960s [92]. This prediction was then confirmed by electron-loss spectroscopy in the same decade. It was noticed that the damping of the ω^+ mode slightly decreased with a smaller thickness of the metallic film [93, 94, 95, 96, 97, 98, 34, 35]. We justify further on our choice of metallic thickness. In the 1980s, Sarid [37] confirmed and

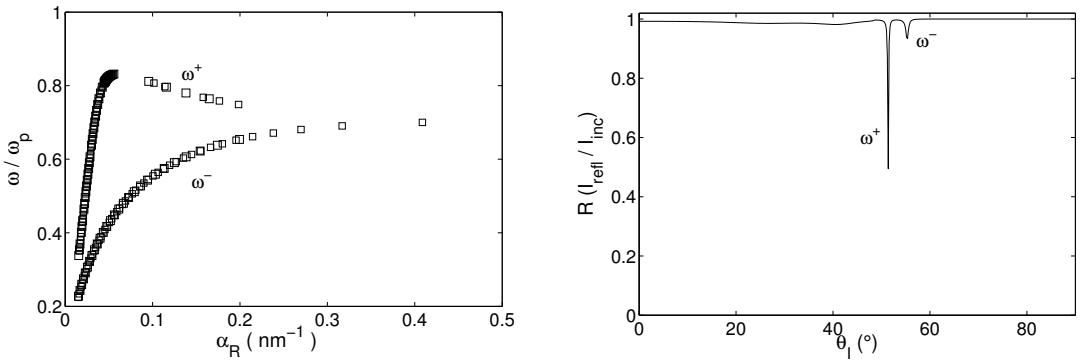

(a) (b)

Figure 2.16: (a) Dispersion curves ω^+ and ω^- of the $LRSP$ and the $SRSP$ modes, respectively. $\varepsilon_d = 1$ is the permittivity of vacuum and the permittivity of the metal ε_m is taken from the experimental data of Palik [81]. The metallic thickness is $e_m = 30$ nm. (b) In the same conditions, the reflectivity is plotted as a function of the incident angle θ_i. The half-width of the mode ω^+ is smaller than the half-width of the mode ω^-. Thus, the absorption of the $LRSP$ mode is smaller than that of the $SRSP$ mode.

established the main characteristics of $LRSPs$ as a measure of the propagation length of these modes, twenty-seven higher than the propagation length of a surface plasmon at the surface of a bulk metal [99, 100].

These plasmonic guides, despite the good propagation length (it can be measured in centimetres), are not interesting for optic guiding [101, 102, 103]. Indeed, the confinement is only in one dimension (perpendicular to the interfaces), which is a limitation for integrating these guides into electronic components. A possibility for using it would be to reduce the width of the metallic films [36].

Up until 2009, a large bibliography on $LRSPs$ was produced by P. Berini [36]. In the study of $LRSPs$, many methods have been employed, either based on Fresnel's coefficients [5], on Maxwell's equations with appropriate boundary conditions [91] or on the method of lines [104, 105]. The method we used to find the dispersion curves as in Fig. 2.16a, and to determine characteristic properties of our structures consists in finding the poles of the scattering matrix. This method is described in Chapter 1 as the tetrachotomy method.

The large range of recent applications [38, 106, 107, 108, 39, 40], such as in photonic crystals, stratified media, quantum systems or with anisotropy, appeal to us with respect to finding a way to excite $LRSP$ without the short mode, and are

	$\delta_{SP} = 1/2\text{Im}(k_{SP})$	Map of the magnetic field	Tetrachotomy algorithm
SP_{ATR}	21μm	14μm	25μm
$\text{LRSP}_{e_{m1}=30\text{nm}}$			262μm
$\text{LRSP}_{e_{m2}=20\text{nm}}$			8.2mm

Table 2.1: Compared propagation lengths between a SP mode in the ATR configuration and the $LRSP$ for two thicknesses $e_{m1} = 30$ nm and $e_{m2} = 20$ nm. The results tabulated here are obtained from the theoretical expression of the propagation length, the map of the magnetic field and the tetrachotomy algorithm. The order of size is correct.

experimentally feasible.

We theoretically demonstrate the equivalence between a metallic film embedded into a symmetric medium of thickness e_m, and a metallic film of thickness $e_m/2$ deposited on a perfect electric conductor substrate (PECS). The interesting point of this device is that it only supports a $LRSP$ and is less complicated to realize experimentally.

2.4.3 Comparison of the length scales

Table 2.1 shows the compared propagation lengths for a SP in the ATR configuration and a $LRSP$ with two metallic thicknesses $e_{m1} = 30$ nm and $e_{m2} = 20$ nm. The SP_{ATR} results are determined with $\lambda = 632.8$ nm, $e_m = 45$ nm, $\varepsilon_d = 2.25$ and $\varepsilon_a = 1$ (Fig. 2.13). The propagation length from the magnetic field map is slightly smaller than the calculated one, which in turn is shorter than the one from the tetrachotomy algorithm. The order of size is correct and the agreement is correct [79].

The propagation lengths for the $LRSP$ mode are determined with the tetrachotomy algorithm. They are truly higher than in the case of a single SP mode. It is for this reason that the study of this mode is interesting for many different applications.

2.5 Theoretical LRSP on PECS

In this section, we demonstrate the equivalence between a $LRSP$ mode in a symmetric structure and the guided mode which exists on a metallic layer deposited on a perfect electric conductor (PEC) substrate [109]. First, we consider the image

charge theory and adapt it to our configuration. Then, we present the theoretical equivalence with the compared dispersion relations of the classical $LRSP$ and the guided mode excited on a metallic film deposited on a PEC substrate. In perspective, we present that it would be possible to realize this device experimentally in the terahertz (THz) frequency range.

2.5.1 Reviewed image charge theory

The image charge theory is a problem of boundary conditions [110]. We consider a charge $+q$ localized at a distance $y = d$ from a perfect electric conducting plane (Fig. 2.17a). The boundary conditions imply that the tangential components of the electric field have vanished on the surface of the PEC. The classical illustration of this theory uses the electrostatic dipole, where a charge $-q$ is localized symmetrically on the other side of the plane, at a distance $y = -d$. The field lines observed in the half-space containing the charge $+q$ correspond to the field lines of an electrical dipole, with a dipolar moment $2dq$. Fig. 2.17b illustrates the equivalent system.

That is the image charge theory that implies the equivalence between the two configuration. In practice, the charge $+q$ attracts the free electrons, and a density of non-uniform surface negative charge is induced at the surface of the PEC [111]. The normal component of the field, created by the positive charge at a point P, located on the PEC plane at a distance r from the origin (see Fig. 2.17a), can be written as:

$$\vec{E}_{n_{q+}}(P) = \vec{E}_{n_{q+}}(r) = -\frac{1}{4\pi\varepsilon_0}\frac{\mathrm{d}q}{(d^2+r^2)^{3/2}}\vec{e}_z. \tag{2.29}$$

The field created by the negative charge at the point P, which cancels the tangential components on the surface of the PEC, is given by:

$$\vec{E}_{n_{q-}}(P) = \vec{E}_{n_{q-}}(r) = -\frac{1}{4\pi\varepsilon_0}\frac{\mathrm{d}q}{(d^2+r^2)^{3/2}}\vec{e}_z. \tag{2.30}$$

The surface charge density at P is also:

$$\sigma_S(P) = \sigma_S(r) = \varepsilon_0 E(r) = \varepsilon_0(E_{n_{q+}}(r) + E_{n_{q-}}(r)) = -\frac{1}{4\pi}\frac{2dq}{(d^2+r^2)^{3/2}}. \tag{2.31}$$

The integration of the last expression for the charge on the surface is equal to

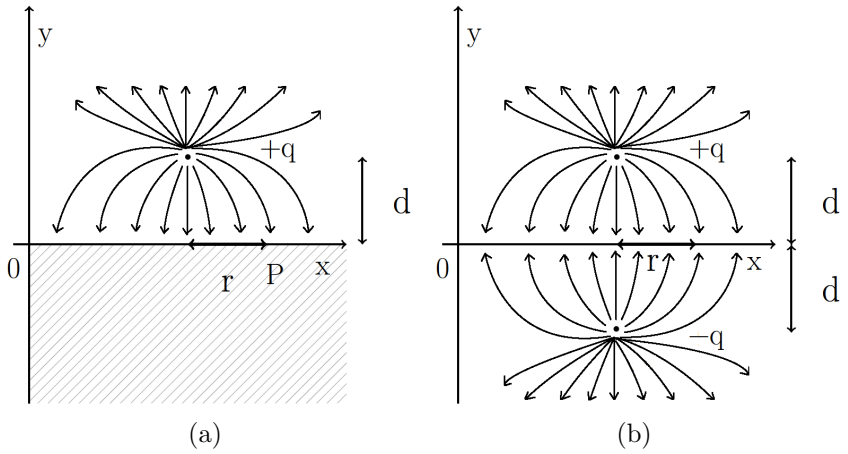

Figure 2.17: (a) Field lines created by an electric charge $+q$ near a PEC substrate. (b) Field lines created by on electric dipole with a dipolar moment $2dq$.

$-q$. Indeed, the conducting plane is an asymmetric plane for charges. A fictitious charge on the other side of the plane is created at a same distance from the surface, d. This result can be generalized to an object with an assembly of charges $+q$. If that distribution of charges is placed at a distance $y = d/2$ from the conducting plane, an equal and opposite distribution of charges exists at $y = -d/2$. With these fictitious charges, the system becomes equivalent to a dipole with a dipolar moment dq.

This theory can be extend to our configuration. In this case, a symmetric metallic film with a thickness e_m has the same properties as a metallic film of thickness $e_m/2$ deposited on a PEC substrate.

From an experimental point of view, it is difficult to deposit homogeneous metallic film of less than 15 nm thickness since metals form nanoscale islands in the initial deposition process [112]. That is why we will consider a metallic layer of thickness $e_m = 30$ nm in the symmetric structure to obtain the limit case where the metallic layer of thickness $e_m/2 = 15$ nm will be deposited on a PEC substrate. However, recent studies show new possibilities for depositing thinner metallic layers [113] but the foremost goal is to demonstrate the equivalence by using common devices.

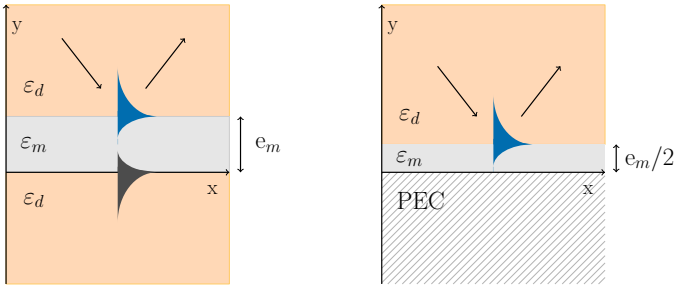

(a) (b)

Figure 2.18: (a) A metallic film embedded in a symmetric medium with a thickness e_m and (b) a metallic layer with a thickness $e_m/2$ deposited on a PEC substrate.

2.5.2 Equivalence of the structures

We recall that the dispersion relation corresponding to the $LRSP$ with a metallic thickness e_m is (Fig. 2.18a):

$$\omega_+ :\ \beta_d\varepsilon_m + \beta_m\varepsilon_d \tanh\left(\frac{\beta_m e_m}{2}\right) = 0. \tag{2.32}$$

The dispersion relation corresponding to the case of a metallic film deposited on a PEC substrate can be deduced from the expression of the field in the different layers (in TM polarization with the time dependence $e^{-i\omega t}$):

$$\begin{cases} y \geq d/2 :\ H_d(x,y) = a_2 e^{i\alpha x} e^{\beta_d' y}, \\ 0 \leq y \leq d/2 :\ H_m(x,y) = e^{i\alpha x}(a_1 e^{\beta_m' y} + b_1 e^{-\beta_m' y}), \end{cases} \tag{2.33}$$

and the magnetic field in the PEC ($y < 0$) is zero. We recall that $\beta_d' > 0$. Let's consider the boundary conditions in the TM polarization. First, for $y = 0$, $\frac{1}{\varepsilon_m}\partial_y H_m = 0$:

$$a_1 = b_1. \tag{2.34}$$

And the magnetic fields become:

$$\begin{cases} H_d(x,y) = a_2 e^{i\alpha x} e^{\beta_d' y}, \\ H_m(x,y) = 2a_1 e^{i\alpha x} \mathrm{ch}(\beta_m' y). \end{cases} \tag{2.35}$$

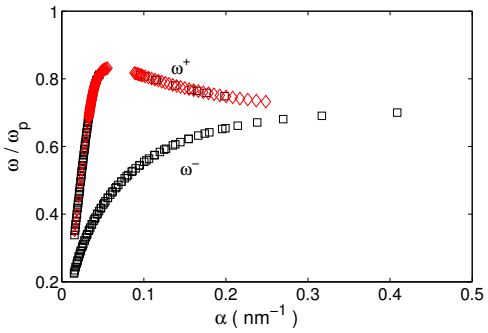

Figure 2.19: The dispersion curve obtained in Fig. 2.16a in black points with a thickness $e_m = 30$ nm and in red points, the dispersion curve corresponding to a metallic layer deposited on the PEC substrate with a metallic thickness $e_m/2 = 15$ nm.

Then, for $y = d/2$, $H_m = H_d$ and $\frac{1}{\varepsilon_m}\partial_y H_m = \frac{1}{\varepsilon_d}\partial_y H_d$:

$$\begin{cases} -2a_1 \frac{\beta_m'}{\varepsilon_m} \mathrm{sh}(\beta_m' d/2) = a_2 \frac{\beta_d'}{\varepsilon_d} e^{\beta_d' d/2}, \\ 2a_1 \mathrm{ch}(\beta_m' d/2) = a_2 e^{\beta_d' d/2}. \end{cases} \tag{2.36}$$

Thus, the dispersion relation is:

$$\frac{\beta_m'}{\varepsilon_m} \tanh\left(\frac{\beta_m' d}{2}\right) + \frac{\beta_d'}{\varepsilon_d} = 0. \tag{2.37}$$

Eqs. 2.32 and 2.37 are equivalent for $\beta_j' = \beta_j$, $j = d, m$.

Fig. 2.19 illustrates the comparison between the corresponding dispersion curves. This shows the equivalence between the dispersion relation ω^+ of a $LRSP$ (upper black-squares curve), supported by a metallic layer embedded in a symmetric medium, and the dispersion relation of the SP mode supported by a metallic layer deposited on PECS (red-squares curve).

The advantage is that it is simpler to deposit a metallic layer on a plane than to have a perfect symmetric medium around a metallic film, especially a medium as such air. Indeed, with this configuration, it is possible to directly excite the $LRSP$ in air. This permits to extend its use to the enhancement of the decay rate of molecules, for example.

The difficulty comes from the lack of availability of a PEC in the visible range.

In theory, it is possible to use supraconductors[2], but an immediate solution is to consider the THz frequency range. Indeed, in this range, a doped-semiconductor (DSC) can have the behavior of a metal in the visible range and support a SP mode [114, 115, 116]. Metal also has the behavior of a PEC (a very high negative real value of permittivity) [116, 109]. This study will be the subject of a future publication.

[2]At wavelength range shorter than their gap.

Chapter 3

Coupling Dielectric Waveguides

OVERVIEW Dielectric waveguides provide simple models for the confining mechanism of waves propagating in optical devices. The coupling of waveguides has been intensively studied, in particular with the coupled-mode theory [49, 50, 51, 52, 53]. After a recall concerning the dielectric slab waveguides, we present the coupled-mode theory. This theory can be derived from the variational principle for the frequencies of the system. When a trial solution is introduced to the electric field in a lossless electromagnetic system such as the linear superposition of modes, the coupled-mode theory gives the result. This theory is also presented in TM polarization, an unpublished result in the state-of-the-art. The last section relates to the case of two optical waveguides which respect the parity time (PT) symmetry. This symmetry has been demonstrated in quantum mechanics by C. M. Bender [54] but it can also be applied to optical devices. A numerical application is also presented.

3.1 Symmetric dielectric waveguides

A symmetric dielectric waveguide is a slab of dielectric material surrounded by media of lower refractive indices. The light is guided inside the slab by total internal reflection. The inner medium and outer media may be the "core" and the "cladding" of the waveguide, respectively. Rather than the metallic waveguides, the waves propagate along the structure without being totally confined. This is

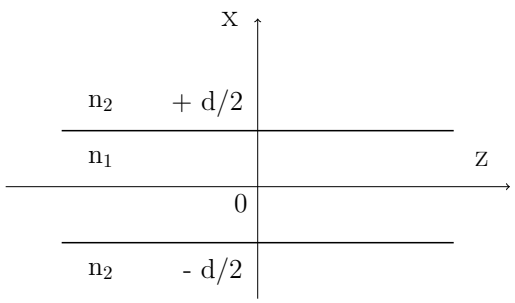

Figure 3.1: A symmetric dielectric waveguide structure. The wave is propagating along the $+z$ direction.

the basic idea underlying dielectric waveguide structures [117, 118, 119].

The waveguides have different forms such as planar waveguides, optical fibers or channel waveguides, for example. In this section, we study the propagation of light in a symmetric planar dielectric waveguide made of a slab of width d and refractive index n_1, surrounded by a cladding of smaller refractive index n_2, as illustrated in Fig. 3.1. All materials are assumed to be lossless.

The propagating fields are confined and guided primarily inside the slab. Only a certain reflection angle θ will constructively interfere in the waveguide and hence only certain waves can exist in the waveguide. Evanescent waves outside it also exist, decaying exponentially with distance from the slab. Fig. 3.2 shows a typical electric field pattern as a function of x.

3.1.1 Expression of the modes

To determine the waveguide modes, a formal approach may be pursued by developing solutions to Maxwell's equations in the inner and outer media with the appropriate boundary conditions. We will consider the transverse magnetic (TM) polarization. Time harmonic modes, with the magnetic field linearly polarized along a direction transverse to the direction of propagation z, are also considered. We denote the magnetic field as $\mathbf{H} = H(x, z)\mathbf{e}_y$ and the time dependence is $e^{-i\omega t}$. We note $H(x, z) = e^{ik_z z} H_x(x)$ and the field $H_x(x)$ satisfied the following equations:

$$\begin{aligned} x < -d/2\text{:}\ & \frac{\partial^2 H_x}{\partial x^2} + (k_2^2 - k_z^2)H_x = 0, \\ -d/2 < x < d/2\text{:}\ & \frac{\partial^2 H_x}{\partial x^2} + (k_1^2 - k_z^2)H_x = 0, \\ x > d/2\text{:}\ & \frac{\partial^2 H_x}{\partial x^2} + (k_2^2 - k_z^2)H_x = 0, \end{aligned} \tag{3.1}$$

where $k_{1,2}^2 = k_0^2\varepsilon_{1,2}$ is the wave vector in the media 1 and 2. We have the dispersion relation $k_{x,j}^2 + k_z^2 = k_0^2\varepsilon_j$ $(j = 1, 2))$ and $k_{x,j}$ takes different values inside and outside the guide.

For waves that remain confined in the near vicinity of the slab, the quantity $k_{x,2}$ must be *imaginary* (if it is real, the field would propagate at large x distances from the slab). We can note $k_{x,2} = -ik_c$ and the solutions outside the core take the form $e^{\pm k_c x}$. If k_c is positive, the physically acceptable solutions are $e^{-k_c x}$ for $x > d/2$ and $e^{+k_c x}$ for $x < -d/2$. The interesting modes are oscillatory modes inside the core and exponentially decaying modes outside, and the corresponding expression of the field is:

$$H_x = \begin{cases} Ae^{+k_c x} & \text{for } x \le -d/2, \\ Be^{+ik_x x} + Ce^{-ik_x x} & \text{for } -d/2 \le x \le d/2, \\ De^{-k_c x} & \text{for } x \ge d/2, \end{cases} \tag{3.2}$$

where $k_c = \sqrt{k_z^2 - k_2^2}$, $k_x = \sqrt{k_1^2 - k_z^2}$ and $k_{1,2} = k_0\sqrt{\varepsilon_{1,2}}$.

It is possible to identify two types of solutions, the even modes (where the magnetic field is symmetric at $x = 0$) and the odd modes (where the magnetic field is antisymmetric at $x = 0$). The even modes can be written as:

$$H_x = \begin{cases} Ae^{+k_c(x+d/2)} & \text{for } x \le -d/2, \\ B\cos(k_x x) & \text{for } -d/2 \le x \le d/2, \\ Ae^{-k_c(x-d/2)} & \text{for } x \ge d/2. \end{cases} \tag{3.3}$$

And the odd modes can be written as:

$$H_x = \begin{cases} -Ae^{+k_c(x+d/2)} & \text{for } x \le -d/2, \\ B\sin(k_x x) & \text{for } -d/2 \le x \le d/2, \\ Ae^{-k_c(x-d/2)} & \text{for } x \ge d/2. \end{cases} \tag{3.4}$$

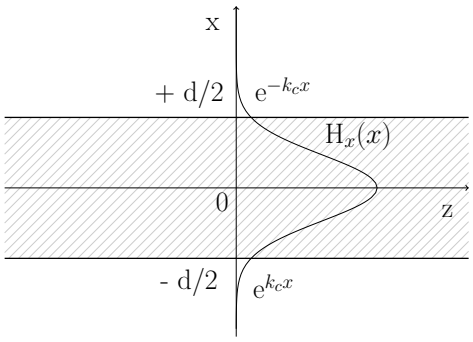

Figure 3.2: A symmetric dielectric waveguide structure. The wave is propagating along the $+z$ direction.

3.1.2 Graphical solutions

At $x = \pm d/2$, H_x and $\frac{1}{\varepsilon_j}\partial_y H_x$ must be conserved in the TM polarization:

$$H_{x,1}(\pm d/2) = H_{x,2}(\pm d/2) \Leftrightarrow \left| \begin{array}{ll} A = B\cos(k_x d/2) & \text{for even modes.} \\ A = B\sin(k_x d/2) & \text{for odd modes.} \end{array} \right. \tag{3.5}$$

$$\begin{aligned} &\frac{1}{\varepsilon_1}\partial_x H_{x,1}(x = \pm d/2) = \frac{1}{\varepsilon_2}\partial_x H_{x,2}(x = \pm d/2) \\ &\Leftrightarrow \left| \begin{array}{ll} Ak_c = Bk_x\sin(k_x d/2) & \text{for even modes.} \\ -Ak_c = Bk_x\cos(k_x d/2) & \text{for odd modes.} \end{array} \right. \end{aligned} \tag{3.6}$$

The Eq. 3.5 and 3.6 allow to find the following transcendental equations:

$$\frac{k_c d}{2} = \frac{\varepsilon_2}{\varepsilon_1}\frac{k_x d}{2}\tan\left(\frac{k_x d}{2}\right), \tag{3.7}$$

$$-\frac{k_c d}{2} = \frac{\varepsilon_2}{\varepsilon_1}\frac{k_x d}{2}\cot\left(\frac{k_x d}{2}\right), \tag{3.8}$$

for the even and the odd modes, respectively. The solutions of these equations can

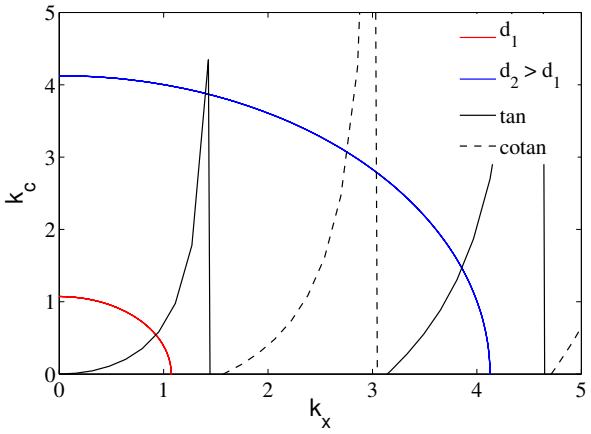

Figure 3.3: Graphical solutions for the guidance conditions. The solutions of the transcendental equations 3.7 and 3.8 are the intersections of the circles with the tangent (for even modes, in solid black curves) and the cotangent (for odd modes, in dashed black curves), respectively.

be found by considering their definitions $k_c = \sqrt{k_z^2 - k_2^2}$ and $k_x = \sqrt{k_1^2 - k_z^2}$:

$$\begin{aligned}\left(\frac{k_c d}{2}\right)^2 + \left(\frac{k_x d}{2}\right)^2 &= \frac{(k_z^2 - k_2^2)d^2}{4} + \frac{(k_1^2 - k_z^2)d^2}{4} \\ &= \frac{(k_1^2 - k_2^2)d^2}{4} \\ &= \frac{\omega^2(\mu_1\varepsilon_1 - \mu_2\varepsilon_2)d^2}{4} = \frac{\omega^2\mu_0\varepsilon_0(n_1^2 - n_2^2)d^2}{4} \\ &= (n_1^2 - n_2^2)\left(\frac{k_0 d}{2}\right)^2 \\ &= R^2,\end{aligned} \tag{3.9}$$

where $k_0 = \omega\sqrt{\mu_0\varepsilon_0}$ is the propagation constant in vacuum. This last relation describes a circle of radius R in the plane defined by (k_c, k_x). The solutions of the transcendental equations will be the intersections of this circle and the tangent (Eq. 3.7) and cotangent (Eq. 3.8) for each parity as illustrated in Fig. 3.3.

To determine the number of TM modes supported by the dielectric waveguide, we examine the graphical solutions (Fig. 3.3). R is the ratio of the thickness of the core on the wavelength in vacuum. Depending on its values, only a limited number of modes can exist. The number of modes increases with the thickness d of the core of the waveguide.

A mode is only allowed when the intersection is on the abscissae, i.e. for

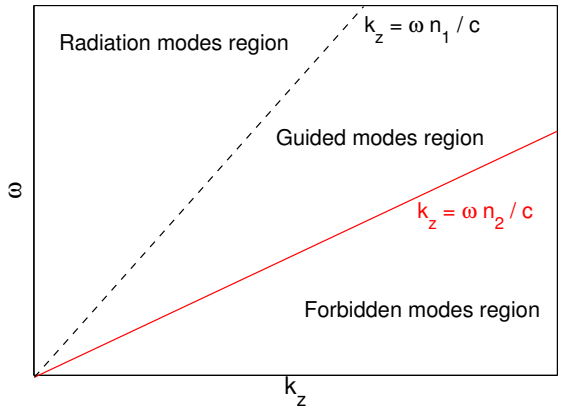

Figure 3.4: Forbidden modes, radiation modes and guided modes regions in the (k_z, ω) plane.

$k_x d/2 = m\pi/2$. It exists only for structures with a thickness:

$$\frac{m\pi}{2} \neq \sqrt{n_1^2 - n_2^2}\frac{\pi d}{\lambda_0}. \tag{3.10}$$

So,

$$\frac{d}{\lambda_0} \geq \frac{m}{2\sqrt{n_1^2 - n_2^2}}. \tag{3.11}$$

For a given thickness, a *cut-off* exists of each mode, except for the fundamental one, noted TM_0. It is the only possible mode when:

$$\frac{d}{\lambda_0} \neq \frac{1}{2\sqrt{n_1^2 - n_2^2}}. \tag{3.12}$$

The waveguide is then a single mode waveguide. This occurs when the slab is sufficiently thin or the wavelength is sufficiently long. Unlike the mirror waveguide, the dielectric waveguide has no absolute cut-off wavelength (or cut-off frequency). In a dielectric waveguide, there is at least one TM mode, the fundamental mode.

3.1.3 Low and high frequency limits

As illustrated in Fig. 3.4, the guided modes are confined to the region between the two dispersion light curves of both media.

At low frequency limit (Fig. 3.5a), we have $(\pi d/\lambda_0)\sqrt{n_1^2 - n_2^2} = m\pi/2$ at the

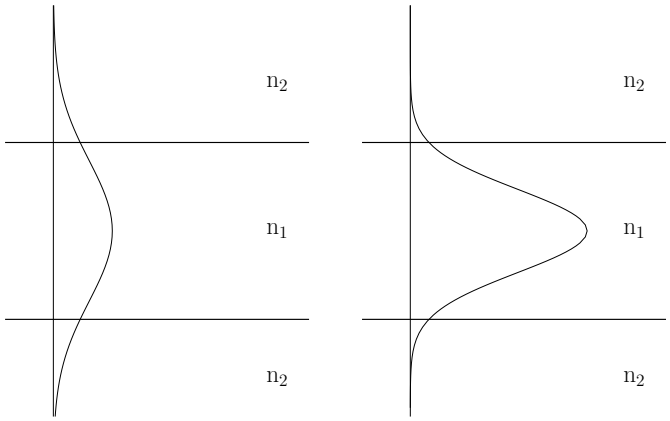

Figure 3.5: The profile of the guided mode in the low (a) and high (b) frequency limits.

cut-off, as we can see with the graphical solutions. Therefore, the propagation constant of the guided mode k_z is near the light line corresponding to the cladding (n_2) outside the waveguide. That means the waveguide mode does not really decay outside the guide. Almost all of the mode power propagates outside the guide and the velocity of this mode is equal to the speed of light outside the guide.

At high frequency limit (Fig. 3.5b), $R \to \infty$ and the graphical solutions show that the propagation constant k_z approaches the light line corresponding to the core (n_1). In this case, the mode decays rapidly outside the guide. Most of the mode power is guided inside it.

3.2 Coupled dielectric waveguides

In this section, we discuss how light can be coupled between two parallel dielectric waveguides. More precisely, we present the coupled-mode theory for wave propagation modes in these parallel waveguides [51, 49, 50, 120].

This theory can be derived from the variational principle for the frequencies of the system [121]. When a trial solution is introduced into the electric field in a lossless electromagnetic system as the linear superposition of modes, the coupled-mode theory gives the result.

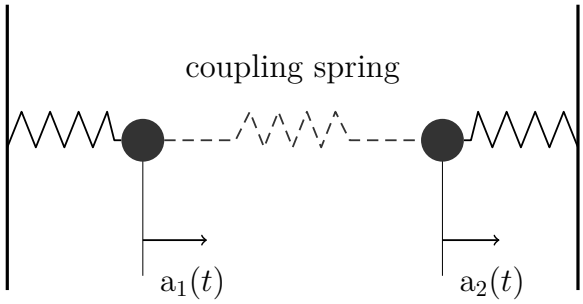

Figure 3.6: Two coupled oscillators with the amplitudes $a_1(t)$ and $a_2(t)$.

3.2.1 Coupling of modes in time

We consider lossless coupling of two modes in time as optical resonators [52, 53]. An analogy of this coupling between the two propagation modes in dielectric waveguides is coupled oscillators (Fig. 3.6). With a time dependence $e^{i\omega t}$, the system consists on two differential equations for the amplitudes:

$$\frac{\mathrm{d}a_1}{\mathrm{d}t} = i\omega_1 a_1, \tag{3.13}$$

$$\frac{\mathrm{d}a_2}{\mathrm{d}t} = i\omega_2 a_2. \tag{3.14}$$

With the coupling coefficients between the two resonators, we can write:

$$\begin{cases} \dfrac{\mathrm{d}a_1}{\mathrm{d}t} = i\omega_1 a_1 + i\kappa_{12} a_2, \\ \dfrac{\mathrm{d}a_2}{\mathrm{d}t} = i\omega_2 a_2 + i\kappa_{21} a_1. \end{cases} \tag{3.15}$$

This assumes that the coupling is weak; thus the coupling coefficients $\mid \kappa_{12} \mid << \omega_1$ and $\mid \kappa_{21} \mid << \omega_2$. An assumption made in the conventional coupled-mode theory is that the modes of the uncoupled systems are orthogonal to each other. Therefore, energy conservation imposes that the eigenfrequencies are real and the

total energy in the two resonators stays constant [122, 123, 124]:

$$\frac{\mathrm{d}}{\mathrm{d}t}(\mid a_1 \mid^2 + \mid a_2 \mid^2) = a_1 a_2^* i(\kappa_{21} - \kappa_{12}^*) + a_1^* a_2 i(\kappa_{12} - \kappa_{21}^*) = 0. \tag{3.16}$$

Since a_1 and a_2 are arbitrarily defined, Eq. 3.16 can only be satisfied for:

$$\kappa_{12} = \kappa_{21}^* = \kappa. \tag{3.17}$$

To find the eigenstate solution of the coupled resonator, we assume that the form of the solution is $a_p(t) = A_p e^{i\omega t}$ with $p = 1, 2$ and ω is the sought frequency of the entire coupled system. Substituting these solutions, in Eqs. 3.15, we obtain a linear system of equations for which the determinant should vanish to obtain non trivial solutions, for $A_{1,2}$. The solutions are also:

$$\omega_\pm = \frac{\omega_1 + \omega_2}{2} \pm \sqrt{\left(\frac{\omega_1 - \omega_2}{2}\right)^2 + \mid \kappa \mid^2}. \tag{3.18}$$

We denote from now:

$$\Phi = \frac{\omega_1 + \omega_2}{2}, \quad \Omega = \sqrt{\Delta^2 + \mid \kappa \mid^2} \quad \text{and } \Delta = \frac{\omega_1 - \omega_2}{2}.$$

Thus, the general solution for $a_1(t)$ and $a_2(t)$ can be written as:

$$\begin{pmatrix} a_1(t) \\ a_2(t) \end{pmatrix} = C_1 \begin{pmatrix} \kappa \\ \Delta + \Omega \end{pmatrix} e^{i\omega_+ t} + C_2 \begin{pmatrix} \kappa \\ \Delta - \Omega \end{pmatrix} e^{i\omega_- t}. \tag{3.19}$$

The solution consists of the beating between two new modes with the frequencies ω_+ and ω_-. We denote $a_1(t = 0) = a_{10}$ and $a_2(t = 0) = a_{20}$. At the time $t = 0$, $a_{10} = (C_1 + C_2)\kappa$ and $a_{20} = C_1(\Delta + \Omega) + C_2(\Delta - \Omega)$. Eq. 3.19 can be written as:

$$\begin{pmatrix} a_1(t) \\ a_2(t) \end{pmatrix} = e^{i\Phi t} \begin{pmatrix} \cos\Omega t - i\frac{\Delta}{\Omega}\sin\Omega t & i\frac{\kappa_{12}}{\Omega}\sin\Omega t \\ i\frac{\kappa_{21}}{\Omega}\sin\Omega t & \cos\Omega t + i\frac{\Delta}{\Omega}\sin\Omega t \end{pmatrix} \begin{pmatrix} a_1(0) \\ a_2(0) \end{pmatrix}. \tag{3.20}$$

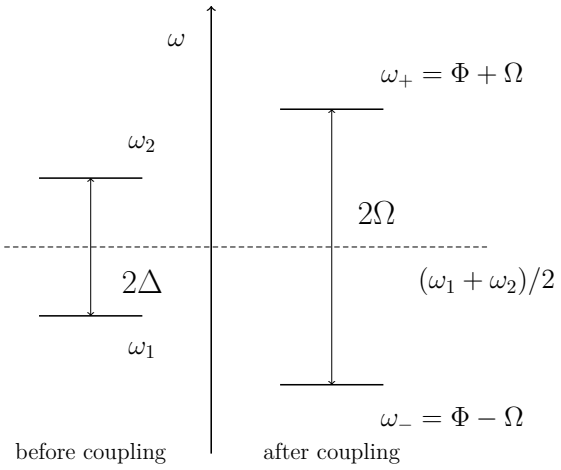

Figure 3.7: The frequency splitting in the case of asynchronous coupling, $\omega_1 \neq \omega_2$.

We assume now that $a_2(0) = 0$ and $\mid a_1 \mid^2 = 1$. The solutions become:

$$\begin{cases} a_1(t) = a_1(0)\left(\cos\Omega t - i\dfrac{\Delta}{\Omega}\sin\Omega t\right)e^{i\Phi t}, \\ a_2(t) = a_1(0) i\dfrac{\kappa_{21}}{\Omega}\sin\Omega t e^{i\Phi t}. \end{cases} \tag{3.21}$$

Two cases can be distinguished as a function of the initial frequencies. If $\omega_1 \neq \omega_2$, we have an *asynchronous* coupling:

$$\mid a_2(t) \mid^2 = \mid \frac{\kappa_{21}}{\Omega} \mid^2 \sin^2\Omega t, \tag{3.22}$$

$$\mid a_1(t) \mid^2 = 1 - \mid a_2(t) \mid^2 . \tag{3.23}$$

In this configuration, the energy is never completely transferred from resonator 1 to 2. The energies $\mid a_1(t) \mid^2$ and $\mid a_2(t) \mid^2$ are plotted in Fig. 3.8a. The energy oscillates periodically between the two resonators with a period π/Ω. We can define a "beat" angular frequency $\omega_B = \omega_+ - \omega_- = 2\Omega$ which characterises the energy exchange rate. Fig. 3.7 illustrates the fact that this frequency splitting is larger than the frequency splitting before the coupling $\omega_2 - \omega_1 = 2\Delta$.

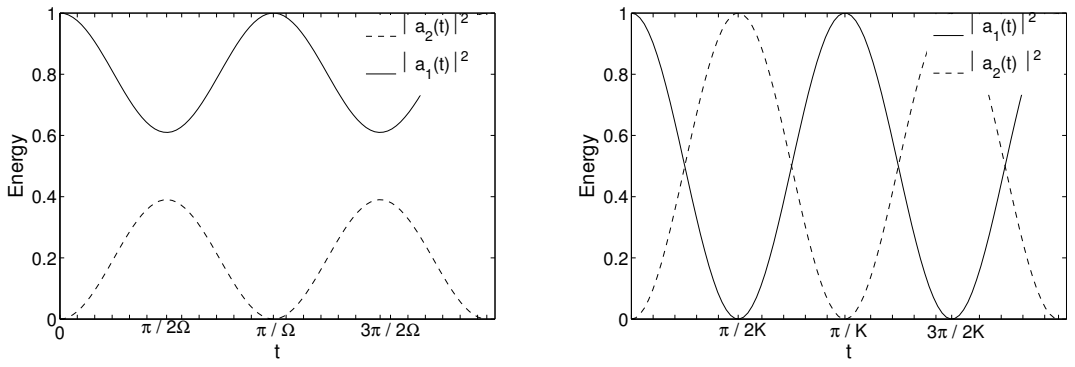

(a) (b)

Figure 3.8: Energies in the resonators 1 and 2, $\mid a_1(t) \mid^2$ and $\mid a_2(t) \mid^2$, as a function of time. (a) For asynchronous coupling, $\omega_1 \neq \omega_2$ where the energy transfer is incomplete. (b) For synchronous coupling, $\omega_1 = \omega_2$ where the energy transfer is complete for the first time $t = \pi/(2\kappa)$.

If $\omega_1 = \omega_2$, we have a *synchronous* coupling:

$$\mid a_1(t) \mid^2 = \cos^2 \kappa t, \tag{3.24}$$

$$\mid a_2(t) \mid^2 = \sin^2 \kappa t. \tag{3.25}$$

At the time $t = (n + 1/2)\pi/\kappa$ (n is an integer), the energy is completely transferred from resonator 1 to 2. The energies $\mid a_1(t) \mid^2$ and $\mid a_2(t) \mid^2$ are plotted in Fig. 3.8b. The one beat period is π/κ and the beat angular frequency is $\omega_B = \omega_+ - \omega_- = 2\kappa$, as shown in Fig 3.9. The initial degenerate frequency ($\omega_1 = \omega_2$) splits into two resonant frequencies, ω_+ and ω_-. The energy splitting is $2 \mid \kappa \mid$, twice the magnitude of the coupling coefficient.

3.2.2 Coupling optical waveguides

At present, the coupled-mode theory is especially useful to study the coupling of identical optical waveguides [125, 51].

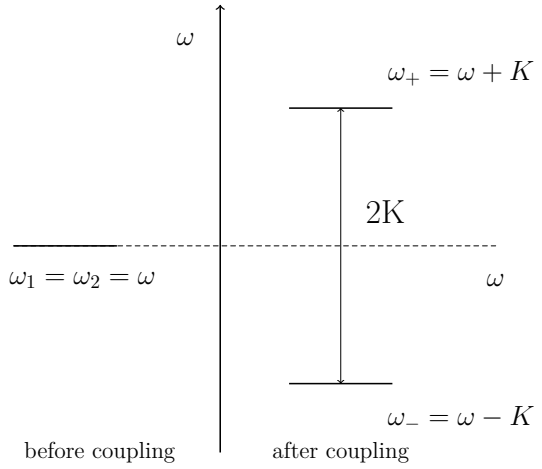

Figure 3.9: The frequency splitting in the case of synchronous coupling, $\omega_1 = \omega_2$.

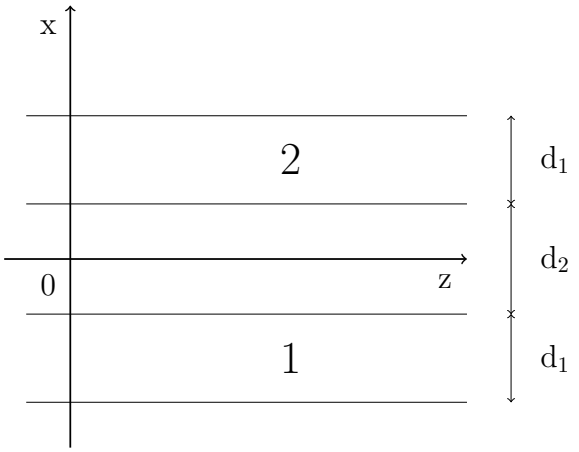

Figure 3.10: Two dielectric parallel waveguides in a symmetric media.

TE polarization

We consider two coupled parallel waveguides, 1 and 2, in the TE polarization (Fig. 3.10). Without coupling, the expressions of the electric and magnetic fields contain the following amplitudes:

$$a_1(z) = a_{01}e^{i\beta_1 z}, \tag{3.26}$$

$$a_2(z) = a_{02}e^{i\beta_2 z}. \tag{3.27}$$

And these amplitudes are satisfactory for propagation in the $+z$ direction in the following system:

$$\frac{\mathrm{d}a_1(z)}{\mathrm{d}z} = i\beta_1 a_1(z), \tag{3.28}$$

$$\frac{\mathrm{d}a_2(z)}{\mathrm{d}z} = i\beta_2 a_2(z). \tag{3.29}$$

With the coupling between the two dielectric waveguides, the field of the system can be written as a linear combination of the individual waveguide modes:

$$\begin{cases} \mathbf{E}(x,y,z) = a_1(z)\mathbf{E}_1(x,y) + a_2(z)\mathbf{E}_2(x,y), \\ \mathbf{H}(x,y,z) = a_1(z)\mathbf{H}_1(x,y) + a_2(z)\mathbf{H}_2(x,y). \end{cases} \tag{3.30}$$

The amplitudes $a_1(z)$ and $a_2(z)$ satisfy the following coupled system:

$$\begin{cases} \dfrac{\mathrm{d}a_1(z)}{\mathrm{d}z} = i\beta_1 a_1(z) + i\kappa_{12}a_2(z), \\ \dfrac{\mathrm{d}a_2(z)}{\mathrm{d}z} = i\kappa_{21}a_1(z) + i\beta_2 a_2(z), \end{cases} \tag{3.31}$$

with κ_{12} and κ_{21}, the coupling coefficients.

The total guided power is:

$$\begin{aligned} P &= \tfrac{1}{2}\mathrm{Re}\int\int \mathbf{E}\times\mathbf{H}^*(x,y)\cdot\mathbf{z}\mathrm{d}x\mathrm{d}y \\ &= s_1 \mid a_1(z)\mid^2 + s_2 \mid a_2(z)\mid^2 + \mathrm{Re}[a_1(z)a_2^*(z)C_{21} + a_2(z)a_1^*(z)C_{12}], \end{aligned} \tag{3.32}$$

with the cross overlap integrals:

$$C_{pq} = \frac{1}{2}\int\int_{-\infty}^{\infty} \mathbf{E}^q(x,y)\times\mathbf{H}^{(p)*}(x,y)\cdot\mathrm{d}x\mathrm{d}y. \tag{3.33}$$

$s_1, s_2 = +1$ for propagation in the $+z$ direction, and -1 for propagation in the $-z$ direction.

We assume that the coupling is weak, so the cross overlap integrals C_{12} and C_{21} are negligible. The total power becomes:

$$P = s_1 \mid a_1(z) \mid^2 + s_2 \mid a_2(z) \mid^2 . \tag{3.34}$$

For a lossless system, the power conservation implies:

$$\frac{\mathrm{d}P}{\mathrm{d}z} = 0 \tag{3.35}$$

Using Eqs. 3.31, this condition can be written as:

$$\kappa_{12} = \kappa_{21}^* \quad \text{if } s_1 s_2 > 0 \quad \text{(codirectional coupling)}, \tag{3.36}$$

$$\kappa_{12} = -\kappa_{21}^* \quad \text{if } s_1 s_2 < 0 \quad \text{(contradirectional coupling)}. \tag{3.37}$$

Under matrix form, the coupled equations 3.31 become:

$$\frac{\mathrm{d}}{\mathrm{d}z}\begin{pmatrix} a_1 \\ a_2 \end{pmatrix} = iM\begin{pmatrix} a_1 \\ a_2 \end{pmatrix} \Leftrightarrow \frac{\mathrm{d}}{\mathrm{d}z}\begin{pmatrix} a_1 \\ a_2 \end{pmatrix} = i\begin{pmatrix} \beta_1 & \kappa_{12} \\ \kappa_{21} & \beta_2 \end{pmatrix}\begin{pmatrix} a_1 \\ a_2 \end{pmatrix}. \tag{3.38}$$

The solutions take the form:

$$\begin{pmatrix} a_1 \\ a_2 \end{pmatrix} = \begin{pmatrix} A_1 \\ A_2 \end{pmatrix} e^{i\beta z} \tag{3.39}$$

The two corresponding eigenvalues for β are:

$$\beta = \frac{\beta_1 + \beta_2}{2} \pm \Psi, \tag{3.40}$$

with:

$$\Psi = \sqrt{\Delta^2 + \kappa_{12}\kappa_{21}}, \tag{3.41}$$

$$\Delta = \frac{\beta_2 - \beta_1}{2}. \tag{3.42}$$

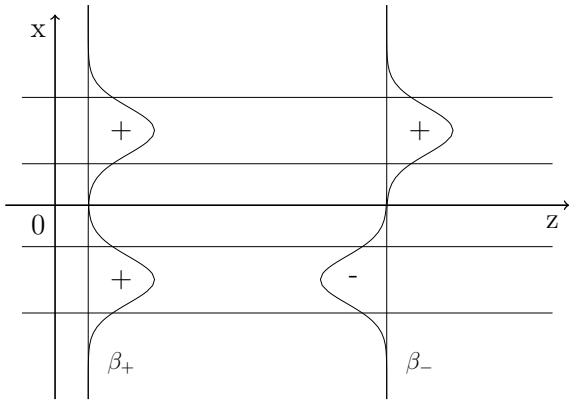

Figure 3.11: Diagram of the two new modes of the system β_+ and β_-.

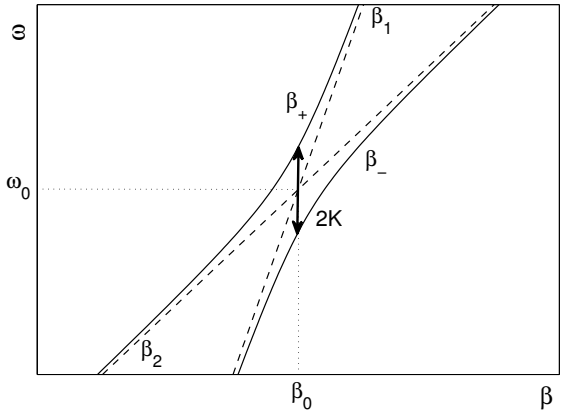

Figure 3.12: Anticrossing of the dispersion curves β_+ and β_- for codirectional coupling. The splitting $(\beta_+ - \beta_-)$ is 2κ.

For codirectional coupling, $\kappa_{21} = \kappa_{12}^*$, Ψ is real for a lossless system. The energy conservation implies that the eigenvalues for β are real and the form of the two new modes is represented in Fig. 3.11. However, Fig. 3.12 illustrates in the plane (β, ω) the corresponding dispersion curves for β_1 and β_2 in dashed curves, in comparison to the dispersion curves of eigensolutions β_+ and β_- of the coupled system, in solid curves. β_1 and β_2 intersect at a given value (β_0, ω_0) when the eigenvalues β_+ and β_- split. Their dispersion curves do not intersect anymore, $\Psi =\mid \kappa_{12} \mid = \kappa$ and the splitting $(\beta_+ - \beta_-)$ is 2κ.

The general solution for $a_1(z)$ and $a_2(z)$ can be written as:

$$\begin{pmatrix} a_1(z) \\ a_2(z) \end{pmatrix} = e^{i\frac{\beta_1+\beta_2}{2}z} \begin{pmatrix} \cos\Psi z - i\frac{\Delta}{\Psi}\sin\Psi z & i\frac{\kappa_{12}}{\Psi}\sin\Psi z \\ i\frac{\kappa_{21}}{\Psi}\sin\Psi z & \cos\Psi z + i\frac{\Delta}{\Psi}\sin\Psi z \end{pmatrix} \begin{pmatrix} a_1(0) \\ a_2(0) \end{pmatrix}. \tag{3.43}$$

We assume that $a_1(0) = 1$, $a_2(0) = 0$ and we find:

$$\mid a_2(z) \mid^2 = \mid \frac{\kappa_{21}}{\Psi} \mid^2 \sin^2 \Psi z, \tag{3.44}$$

$$\mid a_1(z) \mid^2 = 1 - \mid a_2(z) \mid^2 . \tag{3.45}$$

The power transfer is complete for $\Psi z = (2n+1)\pi/2$, where n is an integer. This is the synchronous coupling when $\beta_1 = \beta_2$ (Fig. 3.13b). We have $\Psi =\mid \kappa_{12} \mid$ and the solutions become:

$$\begin{cases} a_1(z) = \cos\kappa z e^{i\beta z}, \\ a_2(z) = i\sin\kappa z e^{i\beta z}, \end{cases} \tag{3.46}$$

where $\kappa = \kappa_{12} = \kappa_{21}$ and $\beta = \beta_1 = \beta_2$.

When $\beta_1 \neq \beta_2$, we have an asynchronous coupling:

$$\mid \frac{\kappa_{12}}{\Psi} \mid^2 = \frac{\mid \kappa_2 1 \mid^2}{[(\beta_2 - \beta_1)/2]^2 + \mid \kappa_{21} \mid^2} < 1. \tag{3.47}$$

The power transfer is never complete in this case (Fig. 3.13a). We take initial

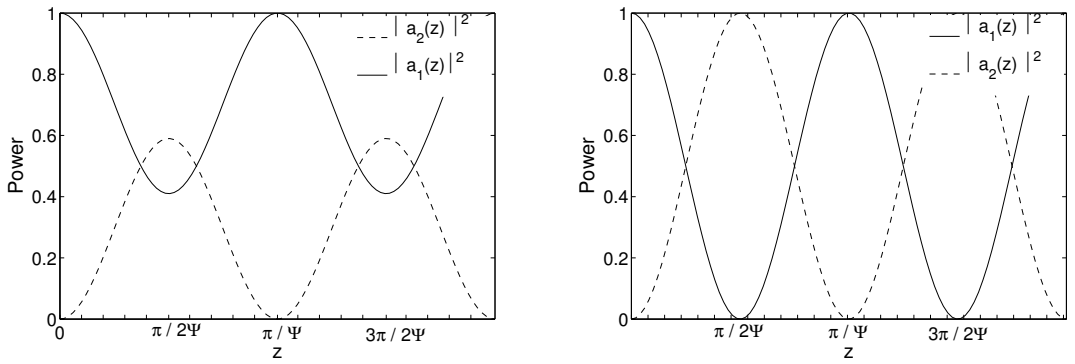

(a) (b)

Figure 3.13: Guided powers, $\mid a_1(z) \mid^2$ and $\mid a_2(z) \mid^2$, as a function of z. (a) For asynchronous coupling, $\beta_1 \neq \beta_2$ where the power transfer is incomplete. (b) For synchronous coupling, $\beta_1 = \beta_2$ where the power transfer can be complete.

values that allow a power transfer in comparison to the case of asynchronous coupling in time (Fig. 3.8a); but whatever the initial conditions, if $\beta_1 \neq \beta_2$, the transfer cannot be complete.

TM polarization

The coupled-mode theory is always presented for TE polarization and for two identical waveguides. In this section, we will present this theory in the case of the TM polarization for the same structure (Fig. 3.10). Finally, we will discuss the difficulty of applying this theory if the two modes are not identical.

As denoted in the previous section, the magnetic field is $\mathbf{H} = u(x,z)\mathbf{e}_y$. The permittivity for all the structure is ε. For the two modes taken separately, the permittivities are ε_1 and ε_2, respectively. We present an advantageous form of Maxwell's equations that linearises the equations in TM polarization:

$$\begin{aligned} &\mathrm{div}(\chi) = -k_0^2, \\ &\nabla u = \varepsilon \chi. \end{aligned} \tag{3.48}$$

We recall that in this form, Maxwell's equations in TE polarization would be $\mathrm{div}(\chi) = -k_0^2 \varepsilon u$ and $\nabla u = \chi$.

The mode for the first waveguide is written (u_1, χ_1) with:

$$u_1(x,z) = \upsilon_1(x)e^{i\gamma_1 z}, \quad \chi_1(x,z) = X_1(x)e^{i\gamma_1 z}, \tag{3.49}$$

and the mode for the second one is written (u_2, χ_2) with:

$$u_2(x,z) = \upsilon_2(x)e^{i\gamma_2 z}, \quad \chi_2(x,z) = X_2(x)e^{i\gamma_2 z}. \tag{3.50}$$

We have the relations:

$$\begin{cases} \mathrm{div}(\chi_1) = -k_0^2 u_1, & \nabla u_1 = \varepsilon_1 \chi_1, \\ \mathrm{div}(\chi_2) = -k_0^2 u_2, & \nabla u_2 = \varepsilon_2 \chi_2. \end{cases} \tag{3.51}$$

The mode of the structure is sought with the ansatz:

$$(u, \chi) = a_1(z)(u_1, \chi_1) + a_2(z)(u_2, \chi_2). \tag{3.52}$$

Maxwell's equations can be rewritten as:

$$\begin{cases} a_1 \mathrm{div}(\chi_1) + a_2 \mathrm{div}(\chi_2) + \nabla a_1 \cdot \chi_1 + \nabla a_2 \cdot \chi_2 = -k_0^2(a_1 u_1 + a_2 u_2), \\ a_1 \nabla u_1 + a_2 \nabla u_2 + u_1 \nabla a_1 + u_2 \nabla a_2 = \varepsilon(a_1 \chi_1 + a_2 \chi_2). \end{cases} \tag{3.53}$$

We simplify and project on z the coupled equations with $\delta_1 = \varepsilon - \varepsilon_1$, $\delta_2 = \varepsilon - \varepsilon_2$:

$$\begin{cases} \chi_{1z}\partial_z a_1 + \chi_{2z}\partial_z a_2 = 0, \\ u_1 \partial_z a_1 + u_2 \partial_z a_2 = \delta_1 \chi_{1z} a_1 + \delta_2 \chi_{2z} a_2. \end{cases} \tag{3.54}$$

The Poynting vector is defined by $\mathrm{P}_z = \mathrm{Im}(\bar{u}\chi_z)$. To extract the Poynting vector from the coupled equations, we begin by multiplying the first equation by $\bar{u}_1$ and the second one by $\bar{\chi}_{1z}$:

$$\begin{cases} \bar{u}_1 \chi_{1z} \partial_z a_1 + \bar{u}_1 \chi_{2z} \partial_z a_2 = 0, \\ \bar{\chi}_1 z u_1 \partial_z a_1 + \bar{\chi}_1 z u_2 \partial_z a_2 = \delta_1 \mid \chi_{1z} \mid^2 a_1 + \delta_2 \bar{\chi}_{1z} \chi_{2z} a_2. \end{cases} \tag{3.55}$$

We subtract:

$$\begin{gathered}(\bar{u}_1\chi_{1z} - \bar{\chi}_{1z}u_1)\partial_z a_1 + (\bar{u}_1\chi_{2z} - \bar{\chi}_1 z u_2)\partial_z a_2 = -\delta_1 \mid \chi_{1z} \mid^2 a_1 - \delta_2\bar{\chi}_{1z}\chi_{2z}a_2, \\ \Leftrightarrow \\ 2i\mathrm{P}_{1z}\partial_z a_1 + (\bar{u}_1\chi_{2z} - \bar{\chi}_1 z u_2)\partial_z a_2 = -\delta_1 \mid \chi_{1z} \mid^2 a_1 - \delta_2\bar{\chi}_{1z}\chi_{2z}a_2.\end{gathered} \tag{3.56}$$

Then, we multiply the first equation by $\bar{u_2}$ and the second one by $\bar{\chi_{2z}}$ to obtain:

$$(\bar{u}_2\chi_{1z} - \bar{\chi}_{2z}u_1)\partial_z a_1 + 2i\mathrm{P}_{2z}\partial_z a_2 = -\delta_2 \mid \chi_{2z} \mid^2 -\delta\bar{\chi}_{2z}\chi_{1z}a_1. \tag{3.57}$$

We also have the following system:

$$\begin{cases} 2i\mathrm{P}_{1z}\partial_z a_1 + (\bar{u}_1\chi_{2z} - \bar{\chi}_1 z u_2)\partial_z a_2 = -\delta_1 \mid \chi_{1z} \mid^2 a_1 - \delta_2\bar{\chi}_{1z}\chi_{2z}a_2. \\ (\bar{u}_2\chi_{1z} - \bar{\chi}_{2z}u_1)\partial_z a_1 + 2i\mathrm{P}_{2z}\partial_z a_2 = -\delta_2 \mid \chi_{2z} \mid^2 -\delta\bar{\chi}_{2z}\chi_{1z}a_1. \end{cases} \tag{3.58}$$

Under matrix form, it becomes:

$$\begin{gathered}\begin{pmatrix} 2i\mathrm{P}_{1z} & \bar{u}_1\chi_{2z} - \bar{\chi}_{1z}u_2 \\ \bar{u}_2\chi_{1z} - \bar{\chi}_{2z}u_1 & 2i\mathrm{P}_{2z} \end{pmatrix} \begin{pmatrix} \partial_z a_1 \\ \partial_z a_2 \end{pmatrix} \\ = \begin{pmatrix} \delta_1 \mid \chi_{1z} \mid^2 & \delta_2\bar{\chi}_{1z}\chi_{2z} \\ \delta_1\bar{\chi}_{2z}\chi_{1z} & \delta_2 \mid \chi_{2z} \mid^2 \end{pmatrix} \begin{pmatrix} a_1 \\ a_2 \end{pmatrix}\end{gathered} \tag{3.59}$$

The matrix in front of $\partial_z a_p$ is hermitian. We integrate in x with the relations $u(x,z) = \upsilon(x)e^{i\gamma z}$, $\chi(x,z) = X(x)e^{i\gamma z}$:

$$\begin{gathered}\begin{pmatrix} 2i\mathrm{P}_{1z} & \bar{u}_1\chi_{2z} - \bar{\chi}_{1z}u_2 \\ \bar{u}_2\chi_{1z} - \bar{\chi}_{2z}u_1 & 2i\mathrm{P}_{2z} \end{pmatrix} \\ = \begin{pmatrix} 2i\mathrm{P}_{1z} & (\bar{\upsilon}_1 X_{2z} - \bar{X}_{1z}\upsilon_2)e^{i(\gamma_2-\gamma_1)z} \\ (\bar{\upsilon}_2 X_{1z} - \bar{X}_{2z}\upsilon_1)e^{i(\gamma_1-\gamma_2)z} & 2i\mathrm{P}_{2z} \end{pmatrix},\end{gathered} \tag{3.60}$$

and:

$$\begin{pmatrix} \delta_1 \mid \chi_{1z} \mid^2 & \delta_2\bar{\chi}_{1z}\chi_{2z} \\ \delta_1\bar{\chi}_{2z}\chi_{1z} & \delta_2 \mid \chi_{2z} \mid^2 \end{pmatrix} = \begin{pmatrix} \delta_1 \mid X_{1z} \mid^2 & \delta_2\bar{X}_{1z}X_{2z}e^{i(\gamma_2-\gamma_1)z} \\ \delta_1\bar{X}_{2z}X_{1z}e^{i(\gamma_1-\gamma_2)z} & \delta_2 \mid X_{2z} \mid^2 \end{pmatrix}. \tag{3.61}$$

We consider the following notations:

$$\Delta = \gamma_2 - \gamma_1, \quad R = \int (\bar{v}_1 X_{2z} - \bar{X}_{1z} v_2) \mathrm{d}x,$$

$$T = \bar{X}_{1z} X_{2z}, \quad t_2 = \int \delta_2 T \mathrm{d}x, \quad t_1 = \int \delta_1 \bar{T} \mathrm{d}x,$$

$$W_1 = \int \delta_1 \mid X_{1z} \mid^2 \mathrm{d}x, \quad W_2 = \int \delta_2 \mid X_{2z} \mid^2 \mathrm{d}x,$$

$$P_2 = \int \mathrm{P}_{2z} \mathrm{d}z, \quad P_1 = \int \mathrm{P}_{1z} \mathrm{d}z.$$

And the system under the matrix form becomes:

$$\begin{pmatrix} 2iP_1 & R \\ -\bar{R} & 2iP_2 \end{pmatrix} \begin{pmatrix} \partial_z a_1 \\ e^{i\Delta z} \partial_z a_2 \end{pmatrix} = \begin{pmatrix} W_1 & t_2 \\ t_1 & W_2 \end{pmatrix} \begin{pmatrix} a_1 \\ e^{i\Delta z} a_2 \end{pmatrix} \tag{3.62}$$

i.e.:

$$\begin{pmatrix} \partial_z a_1 \\ e^{i\Delta z} \partial_z a_2 \end{pmatrix} = \begin{pmatrix} \frac{2iP_2 W_1 - R t_1}{4P_1 P_2 - |R|^2} & \frac{2iP_2 t_2 - R W_2}{4P_1 P_2 - |R|^2} \\ \frac{2iP_1 t_1 + W_1 \bar{R}}{4P_1 P_2 - |R|^2} & \frac{2iP_1 W_2 + t_2 \bar{R}}{4P_1 P_2 - |R|^2} \end{pmatrix} \begin{pmatrix} a_1 \\ e^{i\Delta z} a_2 \end{pmatrix}. \tag{3.63}$$

We note that the modes 1 and 2 are defined up to a multiplicative constant. We take $2\mathrm{P}_{2z} = 2\mathrm{P}_{1z} = 1$.

$$\begin{pmatrix} \partial_z a_1 \\ e^{i\Delta z} \partial_z a_2 \end{pmatrix} = \begin{pmatrix} \frac{iW_1 - R t_1}{1 - |R|^2} & \frac{i t_2 - R W_2}{1 - |R|^2} \\ \frac{i t_1 + W_1 \bar{R}}{1 - |R|^2} & \frac{i W_2 + t_2 \bar{R}}{1 - |R|^2} \end{pmatrix} \begin{pmatrix} a_1 \\ e^{i\Delta z} a_2 \end{pmatrix}. \tag{3.64}$$

We assume that W_1 and W_2 are negligible and simplify the coupled equations. The solutions have the same form as in the case of TE polarization, but with modified variables:

$$\begin{pmatrix} \partial_z a_1 \\ e^{i\Delta z} \partial_z a_2 \end{pmatrix} = \frac{1}{1 - \mid R \mid^2} \begin{pmatrix} -R t_1 & i t_2 \\ i t_1 & t_2 \bar{R} \end{pmatrix} \begin{pmatrix} a_1 \\ e^{i\Delta z} a_2 \end{pmatrix}. \tag{3.65}$$

The solutions take the form $A_p e^{i\gamma z}$ $(p = 1, 2)$ and the two eigenvalues for γ are:

$$\gamma = \Upsilon \pm \Gamma, \tag{3.66}$$

where:

$$\Gamma = \sqrt{\Upsilon^2 - \frac{t_1 t_2}{1 - \mid R \mid^2}}, \tag{3.67}$$

$$\Upsilon = \frac{\bar{R} t_2 - R t_1}{2(1 - \mid R \mid^2)}. \tag{3.68}$$

To obtain physical solutions, we also need $t_1 = t_2$. In other words, we are still in the case of two similarly coupled waveguides. This form of the theory does not allow for the treatment of asymmetric coupled structures.

In the last section, we will discuss the case of parity-time (PT) symmetric waveguides. In this type of structures, the two guides are identical at the beginning. Then, gain is applied to one guide and losses are applied to the other (with the same opposite value).

3.3 PT-Symmetry

In recent years, C. M. Bender published work that allows a continuity of the quantum mechanics into the complex plane [54]. He explored the spectra of non-Hermitian Hamiltonians and found that in fact, many non-Hermitian Hamiltonians can produce entirely real spectra, provided they possess something known as parity-time (PT) symmetry [126, 127, 128].

In quantum mechanics, the fundamental condition of Hermicity of the Hamiltonian operator associated with the physically observable implies real eigenvalues (and probability conservation). The PT symmetry extends the study of the class of non-Hermitian Hamiltonians. The properties of PT symmetry in quantum mechanics is still studied nowadays. In optics, it was also demonstrated in symmetric coupler [129, 130], and in optical lattices [131, 132]. Experimental observations have also been realized [133, 134].

3.3.1 In quantum mechanics

First, we begin with basic aspects of this symmetry in quantum mechanics [134]. The Hermicity of the Hamiltonian in conventional quantum mechanics is replaced by the PT symmetry with non-Hermitian Hamiltonians. The actions of the parity

P and time T operators are defined as follows:

$$P : \hat{p} \to -\hat{p}, \hat{x} \to -\hat{x}, \tag{3.69}$$

$$T : \hat{p} \to -\hat{p}, \hat{x} \to \hat{x}, \hat{i} \to -\hat{i}, \tag{3.70}$$

where $\hat{p}$ and $\hat{x}$ are the momentum and position operators, respectively.

In general, a Hamiltonian $\hat{H}$ can be written as:

$$\hat{H} = \frac{\hat{p}^2}{2m} + V(\hat{x}), \tag{3.71}$$

where $\hat{x}$ and $\hat{p}$ are position and momentum operators respectively, m is mass and V is the potential.

This Hamiltonian is PT symmetric if it shares the same eigenfunctions as the PT operator and satisfies $PT\hat{H} = \hat{H}PT$ [135, 136, 137, 138]. This condition corresponds to an exact or *unbroken* PT symmetry, as opposed to that of *broken* PT symmetry, where, even though this condition is still valid, $\hat{H}$ and PT have different eigenvectors [139].

PT symmetry requires that the Hamiltonian $\hat{H}$ commutes with the PT operator. This implies that the real part of the potential V is an even function of the position x and its imaginary part is an odd one. The Hamiltonian becomes:

$$\hat{H} = \frac{\hat{p}^2}{2m} + V_R(\hat{x}) + i\varepsilon V_I(\hat{x}), \tag{3.72}$$

where $V_{R,I}$ are the symmetric and antisymmetric components of the potential V, respectively [129, 140, 131].

An important property of the PT-symmetric operators appears for the transition from a completely real spectrum to a non strictly one. The transition between an exact PT symmetry to broken PT symmetry is controlled with the parameter ε, which is a measure of the non-Hermicity in the Hamiltonian. If $\varepsilon = 0$, this Hamiltonian is Hermitian. It is also possible to demonstrate that as long as ε is below a critical threshold, noted $\varepsilon < \varepsilon_{th}$, this class of potentials can still describe a real spectra. If this limit is crossed, $\varepsilon > \varepsilon_{th}$, the spectrum is not real any more and starts to involve imaginary eigenvalues. This is the phase transition from the

exact to broken-PT phase [130, 137]. We can speak of a *spontaneous PT symmetry breaking*.

3.3.2 In optics

In optics, several physical processes have an equivalent form to the Schrödinger equation in quantum mechanics such as the spatial diffraction and temporal dispersion. Indeed, K. G. Makris *et al.* [140] suggested that complex PT-symmetric structures could be realized within an optical framework, and in particular through the paraxial theory of diffraction. In order to have a PT symmetric optical model, it is necessary (but not sufficient) to impose the commutation between the Hamiltonian $\hat{H}$ and the PT operator. This is also a constraint on the potential:

$$\hat{H}PT = \frac{\hat{p}^2}{m} + V(x), \tag{3.73}$$

$$PT\hat{H} = \frac{\hat{p}^2}{m} + V^*(-x), \tag{3.74}$$

$$\hat{H}PT = \hat{H}PT, \tag{3.75}$$

which implies:

$$V(x) = V^*(-x). \tag{3.76}$$

By writing the condition of commutation of the operators like that, it is easier to understand that a PT symmetric waveguide can be realized with a symmetric index guiding profile and an antisymmetric gain/loss profile for the refractive index [129]:

$$n(x) = n^*(-x), \tag{3.77}$$

where $n(x)$ plays the part of the potential and we can consider two coupled planar waveguides as illustrated in Fig. 3.15, for which the refractive index only varies in the x direction. The direction of propagation in the waveguides is along the z axis.

We write the complex refractive index distribution $n(x)$ as a sum of its real

and imaginary parts and a constant index n_0:

$$n(x) = n_0 + n_R(x) + in_I(x). \tag{3.78}$$

For a PT symmetric Hamiltonian, the refractive index $n_R(x)$ is then an even function, and the gain/loss distribution $n_I(x)$ an odd function of the position [130, 129, 140, 132]. We must also satisfy the conditions $n_R(x) = n_R(-x)$ and $n_I(x) = -n_I(-x)$.

In the past years, the double-channel waveguide structure has been studied extensively, and the results have shown that the coupler can support symmetry preserving solutions, which have linear counterparts, and symmetry breaking solutions without any linear counterparts [141, 142, 143].

K. G. Makris *et al.* [140] achieved the construction of a coupled system with two channels, one of which would receive gain, G, through optical pumping and the other only loss, L. For optical beams, the electric envelope E is governed by the paraxial equation of diffraction:

$$i\partial_z E + \frac{1}{2k_0 n_0}\partial_x^2 E + k_0[n_R(x) + in_I(x)]E = 0, \tag{3.79}$$

where $k_0 = 2\pi/\lambda$, with λ the wavelength.

Under these conditions and by using the coupled-mode approach, the optical field dynamics in the two coupled waveguides are described by:

$$i\frac{\mathrm{d}E_1}{\mathrm{d}z} - i\frac{\gamma_{Geff}}{2}E_1 + \kappa E_2 = 0, \tag{3.80}$$

$$i\frac{\mathrm{d}E_2}{\mathrm{d}z} + i\frac{\gamma_{Geff}}{2}E_2 + \kappa E_1 = 0, \tag{3.81}$$

with $E_{1,2}$ the field amplitudes in the respective channels, $\kappa = \pi/2L_c$ the coupling constant with coupling length L_c and $\gamma_{Geff} = \gamma_G - \gamma_L$ the effective gain. To have a PT symmetric system, we need $\gamma_{Geff} = \gamma_L = \gamma$.

The PT symmetric coupled equations in matrix form with the non-Hermitian Hamiltonian are written as:

$$i\frac{\mathrm{d}}{\mathrm{d}z}\begin{bmatrix} E_1(z) \\ E_2(z) \end{bmatrix} = H\begin{bmatrix} E_1(z) \\ E_2(z) \end{bmatrix}, \tag{3.82}$$

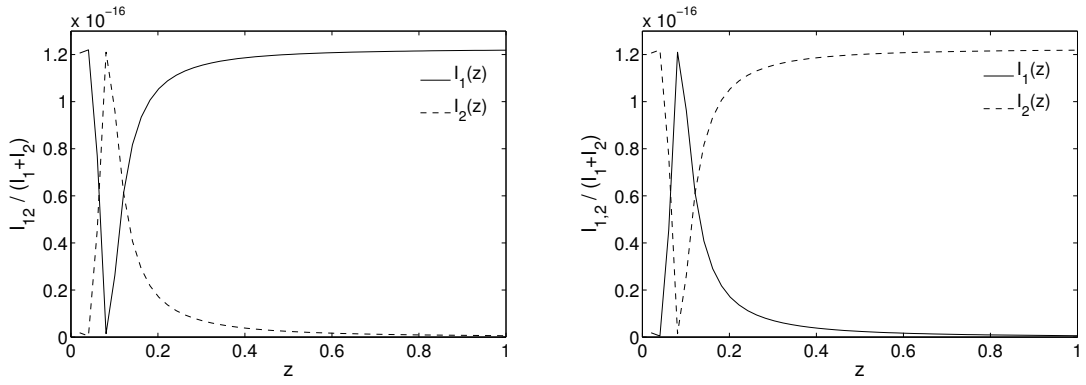

(a) (b)

Figure 3.14: Intensity at the output with the analytic solutions of the coupled equations 3.85 and 3.86. (a) The channel 1 is excited. (b) The channel 2 is excited.

with

$$H = \begin{bmatrix} \frac{1}{2}i\gamma & -\kappa \\ -\kappa & \frac{1}{2}i\gamma \end{bmatrix}. \tag{3.83}$$

The solutions can be written as:

$$\begin{bmatrix} E_1(z) \\ E_2(z) \end{bmatrix} = e^{-iHt} \begin{bmatrix} E_1(0) \\ E_2(0) \end{bmatrix}. \tag{3.84}$$

Thus, the electric fields $E_{1,2}(z)$ are a function of the initial states $E_1(0)$ and $E_2(0)$:

$$E_1(z) = \left(\cosh(1/2\xi(z)) + \frac{\gamma z \sinh(1/2\xi(z))}{\xi(z)} \right) E_1(0) + \frac{2iz \sinh(1/2\xi(z))\kappa}{\xi(z)} E_2(0), \tag{3.85}$$

$$\begin{aligned} E_2(z) = \left(-\cosh(1/2\xi(z)) + \frac{\gamma z \sinh(1/2\xi(z))}{\xi(z)} \right) E_2(0) \\ + \frac{2iz \sinh((1/2\xi(z))\kappa)}{\xi(z)} E_1(0), \end{aligned} \tag{3.86}$$

with $\xi(z) = \sqrt{z^2(-4\kappa^2 + \gamma^2)}$.

In addition, it is possible to measure and plot the intensity distribution at the output. Fig. 3.14 illustrates the intensities $E_{1,2}$ as a function of the distance z.

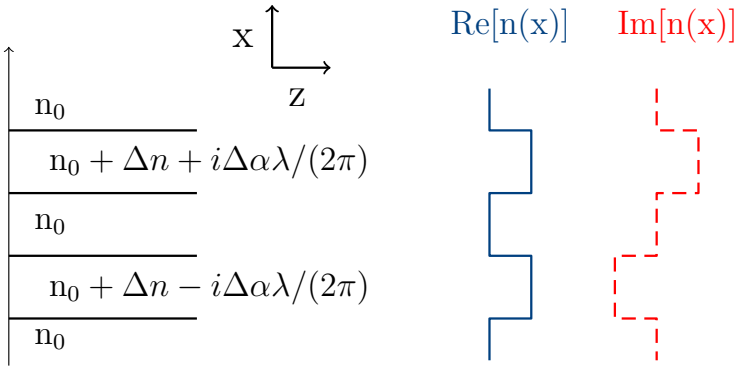

Figure 3.15: Two coupled waveguides where one waveguide has gain (with a negative imaginary part of the refractive index) and the other has losses (with a positive imaginary part of the refractive index) [130].

3.3.3 Numerical application

We consider the following optical PT symmetric structures, illustrated in Fig. 3.15. This consists of two coupled waveguides where one waveguide has gain (with a positive imaginary part of the refractive index), and the other has losses (with a negative imaginary part of the refractive index) [130]. The separation between the waveguides and their thickness are taken to be the same, noted d [129]. It was demonstrated that the coupling between the two PT symmetric waveguides is an increasing function of the separation between the waveguides, as in the case with classical directional waveguides.

We use the result in [130] where the background index is $n_0 = 3.3$, the incident wavelength in vacuum is $\lambda = 1.55\mu$m. The real part of the refractive index for the two waveguides is $n_0 + 10^{-3}$ and the separation between the waveguides is $d = 5\mu$m. It has been demonstrated that these parameters allows the existence of only a single guided modes in the two waveguides. Then, imaginary parts for the refractive index are added into the two waveguides: $\Delta\alpha\lambda/(2\pi)$, that adds losses in the first guide; and $-\Delta\alpha\lambda/(2\pi)$, that adds gain in the other.

The propagation constants of the two modes are plotted in Fig. 3.16 as a function of the non-Hermicity parameter $\Delta\alpha$. When $\Delta\alpha$ increases, the propagation constants of the two modes move towards a critical point $\Delta\alpha_c$. Such a point in the spectrum is often referred to as an *exceptional point* [144]. The two guided modes

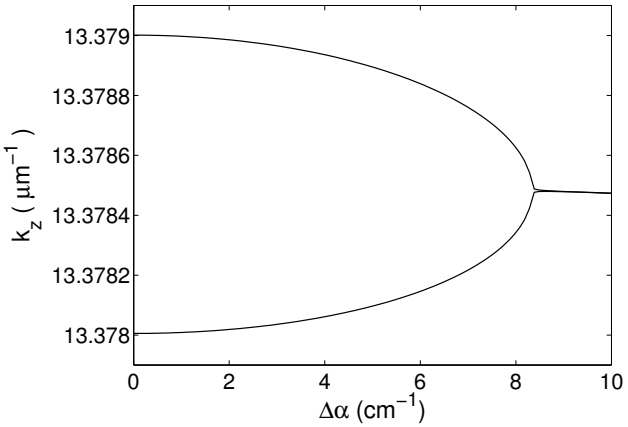

Figure 3.16: The propagation constant k_z as a function of the non-Hermicity parameter $\Delta\alpha$. The eigenmodes approach each other up to a critical point $\Delta\alpha_c \sim 8.4$ [130]. Beyond this critical point, the propagation constants become complex conjugates of one another and the PT symmetry breaks.

are always PT symmetric. At this critical point, the propagation constants of the two modes and the corresponding electric field become equal. Beyond this critical point, the propagation constants become complex conjugates of one another and we can see a break in the PT symmetry. The behavior of the propagation constant can be also illustrated in the complex plane $(\mathrm{Re}[k_z], \mathrm{Im}[k_z])$ as in Fig. 3.17. The breaking of the PT symmetry arises when the two modes have the same real value. The imaginary part grows towards surrealistic values of gain.

The evolution of the two coupled modes is obtained by considering the power distribution:

$$\mid E_y(x,z) \mid^2 = \mid \frac{1}{\sqrt{2}}[\mathcal{E}_1(x)e^{-i\beta_1 z} + \mathcal{E}_2(x)e^{-i\beta_2 z}] \mid^2, \tag{3.87}$$

for three values of $\Delta\alpha$ (Fig. 3.18). When $\Delta\alpha$ increases and goes to the critical value, the beat length increases. It is an interesting way to observe the movement of the propagation constants on the real axis. At the critical value $\Delta\alpha$, there are no longer oscillations between the waveguides, but a simultaneous propagation in both waveguides. An interpretation of this phenomenon is that the critical value of $\Delta\alpha$ corresponds to the maximum value of the matching index profile, which can still be treated with the perturbation theory.

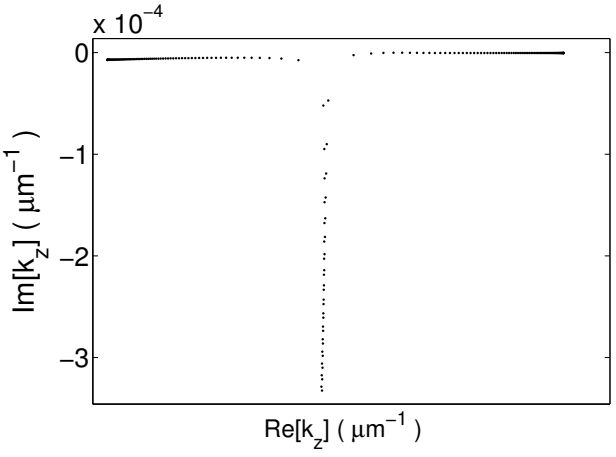

(a)

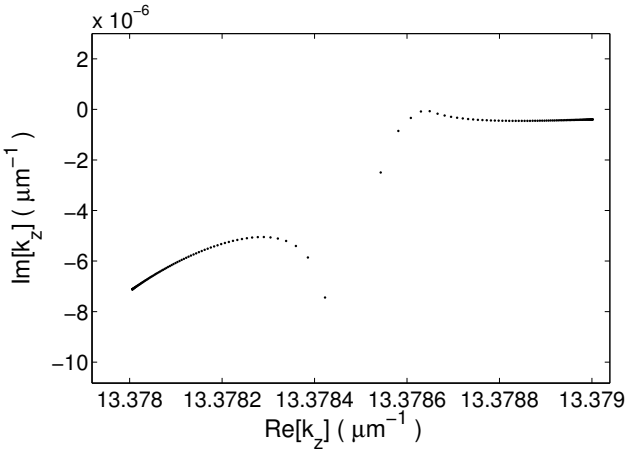

(b)

Figure 3.17: The propagation constant in the complex plane $(\mathrm{Re}[k_z], \mathrm{Im}[k_z])$ with a global view in (a) and a zoom in (b). After the breaking of the PT symmetry, the imaginary parts grow towards surrealistic values.

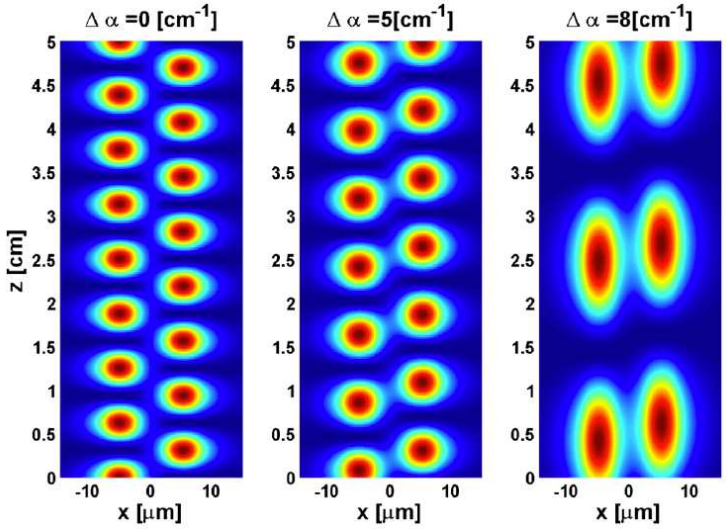

Figure 3.18: Color maps of the field for three values of $\Delta\alpha$. The beat length increases with the value of $\Delta\alpha$ until the critical point [130].

Chapter 4

Strong Coupling Surface Plasmon Polaritons

Overview When the emitter-photon interaction becomes larger than the linewidths of either the cavity photon or the exciton, the strong coupling regime occurs. This regime has been intensively studied since the work of C. Weisbuch *et al.* [55]. In this case, the irreversible spontaneous emission is replaced by a reversible exchange of energy between the emitter and the photon. The strong coupling is manifest by an anticrossing between the emitter and the cavity mode dispersion relations, characterized by a vacuum Rabi splitting [56]. The energy exchange is periodic with time-scales shorter than the inverse cavity field decay rate. In the first section, we introduce the characteristics of the strong coupling regime with the classical case of two coupled oscillators. Then, the properties of the strong coupling regime in microcavities are presented until recent works involving surface plasmons. Finally, we will demonstrate the strong coupling regime between SP modes and guided modes in a layered structure. We study more precisely the features of the new modes to justify the interest in this kind of structure and add gain to enhance the plasmon emission.

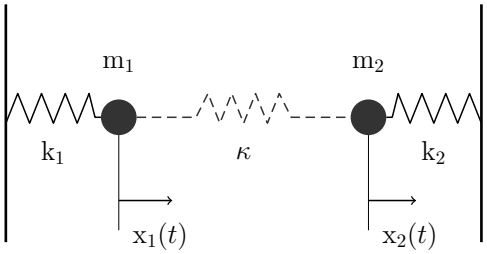

Figure 4.1: Two coupled oscillators with a coupling constant κ.

4.1 Classical coupled oscillators

We consider a classical coupled oscillator model as a canonical example for strong coupling [145, 146]. Firstly, we consider two identical coupled oscillators with damping to shed light in the transition between the weak coupling regime to the strong coupling regime, as well as to show the oscillations between the two strongly coupled modes. Then, we study the case of two different oscillators without damping in order to present the characteristic anticrossing of the dispersion curves in the strong coupling regime.

4.1.1 Strong coupling transition

In the absence of coupling ($\kappa = 0$), the two oscillators have the eigenfrequencies $\omega_1^0 = \sqrt{k_1/m_1}$ and $\omega_2^0 = \sqrt{k_2/m_2}$, with m_p and k_p, where $p = 1, 2$ are the masses and the spring constants of the oscillators, respectively. In the presence of coupling ($\kappa \neq 0$) as illustrated in Fig. 4.1, the equations of the motion become:

$$\begin{cases} m_1\ddot{x}_1 + k_1x_1 + \kappa(x_1 - x_2) = -\gamma_1\dot{x}_1, \\ m_2\ddot{x}_2 + k_2x_2 + \kappa(x_2 - x_1) = -\gamma_2\dot{x}_2, \end{cases} \tag{4.1}$$

where $\gamma_1\dot{x}_1$ and $\gamma_2\dot{x}_2$ are frictional terms representing the damping of the two oscillators.

We are looking for the solution to the form $x_p(t) = x_p^0 e^{i\omega_\pm t}$, where $\omega_\pm$ are the new eigenfrequencies of the coupled system. We note $\omega_p^2 = (k_p + \kappa)/m_p$ and

$\kappa/m_p = \omega_p\Omega$ with $p = 1, 2$. We insert this ansatz into Eq. 4.1 and the two coupled linear equations for x_1^0 and x_2^0 are:

$$\begin{pmatrix} \omega^2 - \omega_1^2 - i\omega\gamma_1 & \omega_1\Omega \\ \omega_2\Omega & \omega^2 - \omega_2^2 - i\omega\gamma_2 \end{pmatrix} \begin{pmatrix} x_1^0 \\ x_2^0 \end{pmatrix} = 0. \tag{4.2}$$

Let us consider that the two oscillators are the same, $m_1 = m_2 = m_0$, $k_1 = k_2 = k_0$ and $\omega_1^2 = \omega_2^2 = \omega_0^2$. Near the resonance, the sought eigenfrequency is $\omega \sim \omega_0$. We denote $\Delta = \omega - \omega_0$ and $\omega^2 - \omega_0^2 = (\omega - \omega_0)(\omega + \omega_0) \sim 2\omega_0\Delta$.

In matrix form such as $M[x_1^0 x_2^0]^T = 0$, the two coupled linear equations become:

$$\begin{pmatrix} 2\Delta - i\gamma_1 & \Omega \\ \Omega & 2\Delta - i\gamma_2 \end{pmatrix} \begin{pmatrix} x_1^0 \\ x_2^0 \end{pmatrix} = 0. \tag{4.3}$$

Non-trivial solutions $\Delta_\pm$ correspond to $\det[M] = 0$. The reduced discriminant is also $\Omega^2 - (\gamma_1 - \gamma_2)^2$ and the solutions $\Delta_\pm$ depend on the sign of the square root. We denoted $\Omega_c =\mid \gamma_1 + \gamma_2 \mid /2$ the critical coupling value.

If $\Omega < \Omega_c$, the system is in the weak coupling regime and the solutions are:

$$\Delta_\pm = \frac{i}{4}(\gamma_1 + \gamma_2) \pm \frac{i}{4}\sqrt{\left(\frac{\gamma_1 - \gamma_2}{2}\right)^2 - \Omega^2}. \tag{4.4}$$

The corresponding eigenfrequencies $\omega_\pm$ and damping coefficients $\gamma_\pm$ are:

$$\omega_\pm = \mathrm{Re}(\omega_0 + \Delta_\pm) = \omega_0, \tag{4.5}$$

$$\gamma_\pm = 2\mathrm{Im}(\omega_0 + \Delta_\pm) = \frac{\gamma_1 + \gamma_2}{2} \pm \frac{1}{2}\sqrt{\left(\frac{\gamma_1 - \gamma_2}{2}\right)^2 - \Omega^2}. \tag{4.6}$$

The two modes have also the same eigenfrequency ω_0 and different damping coefficients which change from γ_1 to γ_2 with no coupling ($\Omega = 0$). At the critical coupling value Ω_c, the damping coefficients have a unique value $(\gamma_1 + \gamma_2)/2$.

If $\Omega > \Omega_c$, the system is in the strong coupling regime and the solutions are:

$$\Delta_\pm = \frac{i}{4}(\gamma_1 + \gamma_2) \pm \frac{1}{4}\sqrt{\Omega^2 - \left(\frac{\gamma_1 - \gamma_2}{2}\right)^2}. \tag{4.7}$$

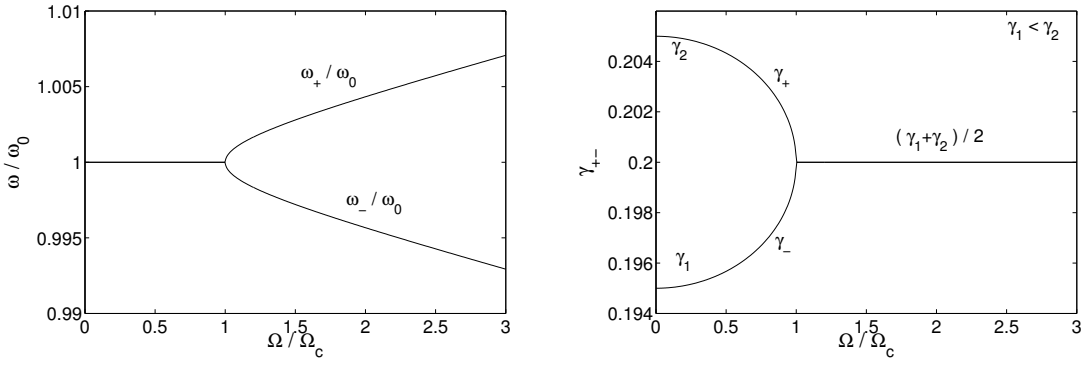

(a) (b)

Figure 4.2: (a) Variation of the eigenfrequencies $\omega_\pm$ and (b) variation of the damping coefficients $\gamma_\pm$ as a function of the coupling coefficient Ω. We take $\omega_0 = 1$, $\Omega_c/\omega_0 = 0.01$, $\gamma_1/\omega_0 = 0.1$ and $\gamma_2/\omega_0 = 0.3$. At the critical coupling value Ω_c, the eigenfrequencies are splitting, whereas the damping coefficients become equal.

The corresponding eigenfrequencies $\omega_\pm$ and damping coefficients $\gamma_\pm$ are:

$$\omega_\pm = \omega_0 \pm \frac{1}{4}\sqrt{\Omega^2 - \left(\frac{\gamma_1 - \gamma_2}{2}\right)^2}, \tag{4.8}$$

$$\gamma_\pm = \frac{\gamma_1 + \gamma_2}{2} = \gamma. \tag{4.9}$$

The two modes also have eigenfrequencies for which the gap increases with the coupling, and a same damping coefficient equal to the mean of the non-coupled oscillators' damping coefficients.

Figs. 4.2a and 4.2b respectively illustrate the variation of the eigenfrequencies $\omega_{/pm}$ and the damping coefficients $\gamma_\pm$ as a function of the coupling coefficient Ω, with $\Omega_c/\omega_0 = 0.01$ [147]. For $\omega_\pm$, we consider the following adimensioned expressions:

$$\frac{\omega_\pm}{\omega_0} = 1 \pm \frac{\Omega_c}{4\omega_0}\sqrt{\left(\frac{\Omega}{\Omega_c}\right)^2 - 1}. \tag{4.10}$$

Before the critical coupling value Ω_c, the modes have the same eigenfrequency. At Ω_c, the eigenfrequencies split into ω_+ and ω_-. In the strong coupling regime, the initial uncoupled modes do not exist anymore, two new states of the system replace

them with the corresponding frequencies ω_+ and ω_- for new eigenfrequencies. This splitting is commonly called a *Rabi splitting*.

For $\gamma_\pm$, we also consider the following adimensioned expressions:

$$\gamma_\pm = \gamma \pm \frac{\Omega_c}{2}\sqrt{1-\left(\frac{\Omega}{\Omega_c}\right)^2}. \tag{4.11}$$

Before the critical coupling value Ω_c, the modes have different damping coefficients γ_- and γ_+, that start from γ_1 and γ_2, respectively, if $\gamma_1 > \gamma_2$. At Ω_c, the damping coefficients become equal to the value $(\gamma_1+\gamma_2)/2$. In the strong coupling regime, the damping in the system cannot be considered separately anymore.

4.1.2 Temporal oscillations

From now on, we only consider the case of a strong coupling regime and we suppose that $\Omega >> \Omega_c$. The sought solutions have the form $x_p(t) = x_p^0 e^{i\omega_\pm t}$, $p = 1, 2$ that can be rewritten as:

$$x_1(t) = \mathrm{Re}(x_1^0 e^{i\tilde{\omega}t}) \text{ with } x_1^0 = b_1 e^{i\phi_1},$$

$$x_2(t) = \mathrm{Re}(x_2^0 e^{i\tilde{\omega}t}) \text{ with } x_2^0 = b_2 e^{i\phi_2},$$

with $\tilde{\omega} = \omega + i\frac{\gamma}{2}$, where $\omega > 0$ is the frequency and $\gamma > 0$, the damping coefficient of the system. Its amplitude decreases such as $exp(-\frac{\gamma}{2}t)$ and its energy decreases such as $exp(-\gamma t)$.

The general solutions can be written as:

$$x_1(t) = A_+ e^{-\frac{\gamma}{2}t}\cos(\omega_+ t + \phi_+) + A_- e^{-\frac{\gamma}{2}t}\cos(\omega_- t + \phi_-), \tag{4.12}$$

$$x_2(t) = -A_+ e^{-\frac{\gamma}{2}t}\cos(\omega_+ t + \phi_+) + A_- e^{-\frac{\gamma}{2}t}\cos(\omega_- t + \phi_-). \tag{4.13}$$

In the case when only one mode is excited, we have the following expressions:

$$\text{mode } \omega_+ \text{:} \begin{cases} x_1(t) = A_+ e^{-\frac{\gamma}{2}t}\cos(\omega_+ t + \phi_+), \\ x_2(t) = -A_+ e^{-\frac{\gamma}{2}t}\cos(\omega_+ t + \phi_+). \end{cases} \tag{4.14}$$

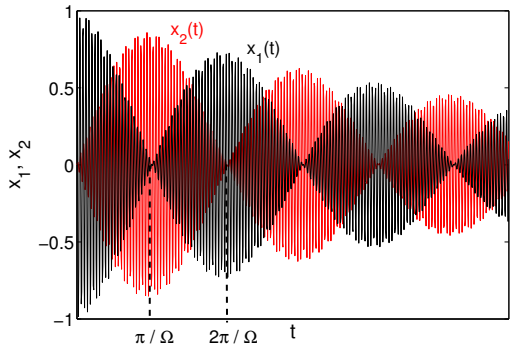

Figure 4.3: Temporal evolution of the modes $x_1(t)$ and $x_2(t)$ with the initial conditions $x_1(0) = x_0$, $x_2(0) = 0$, $\partial_t x_1(0) = 0$ and $\partial_t x_2(0) = 0$. We take $\omega_0 = 1$, $\Omega/\omega_0 = 0.02$, $\gamma/\omega_0 = 0.002$, $\Omega >> \Omega_c$ and $x_0/w_0 = 2$. Each mode is the sum of a sinusoidal amplitude with a different frequency but with the same damping. The energy of the oscillator 1 is completely transferred to the other oscillator after a time equal to π/Ω. It is totally back after a time equal to $2\pi/\Omega$. The two modes have the same amplitude for an impulsion of $\pi/2$, after a time equal to $\pi/(2\Omega)$.

And:

$$\text{mode } \omega_-: \quad \begin{cases} x_1(t) = A_- e^{-\frac{\gamma}{2}t} \cos(\omega_- t + \phi_-), \\ x_2(t) = A_- e^{-\frac{\gamma}{2}t} \cos(\omega_- t + \phi_-). \end{cases} \tag{4.15}$$

At the time $t = 0$, the oscillator 1 is excited and the initial conditions are $x_1(0) = x_0$, $x_2(0) = 0$, $\partial_t x_1(0) = 0$ and $\partial_t x_2(0) = 0$. The solutions become:

$$\begin{cases} x_1(t) = x_0 e^{-\frac{\gamma}{2}t} \cos\left(\frac{\sqrt{\Omega^2 - \Omega_c^2}}{2}\right) \cos(\omega_0 t), \\ x_2(t) = x_0 e^{-\frac{\gamma}{2}t} \sin\left(\frac{\sqrt{\Omega^2 - \Omega_c^2}}{2}\right) \sin(\omega_0 t), \end{cases} \tag{4.16}$$

and Fig. 4.3 illustrates the result. We observe coherent oscillations between the modes. Each mode is the sum of a sinusoidal amplitude with a different frequency but with the same damping. The energy of the oscillator 1 is completely transferred to the other oscillator after a time equal to π/Ω. It is totally back after a time equal to $2\pi/\Omega$. The two modes have the same amplitude for an impulsion of $\pi/2$, after a time equal to $\pi/(2\Omega)$. Theses oscillations are called *Rabi oscillations*.

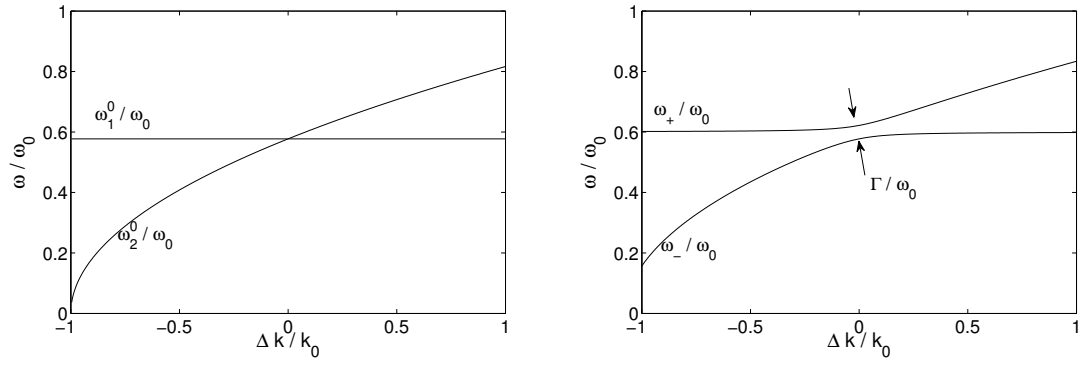

(a) (b)

Figure 4.4: Eigenfrequencies of the two oscillators as a function of the coefficient Δk. Their spring constants are k_0 and $k_0 + \Delta k$, respectively, and their masses are equal. We take $k_0 = 1$. (a) In the uncoupled case ($\kappa = 0$), the dispersion curves intersect for $\Delta k = 0$. (b) In the coupled case ($\kappa = 0.08k_0$), the strong coupling regime is characterized by an anticrossing of the dispersion curves with a frequency splitting $[\omega_+ - \omega_-] = \Gamma$.

4.1.3 Anticrossing of the dispersion curves

Let's consider the two oscillators without damping ($\gamma_p = 0$, $p = 1, 2$) and with different spring constants (Fig. 4.1). The corresponding eigenfrequencies $\omega_\pm$ become:

$$\omega_\pm = \frac{1}{2}[\omega_1^2 + \omega_2^2 \pm \sqrt{(\omega_1^2 - \omega_2^2)^2 + 4\Gamma^2\omega_1\omega_2}], \tag{4.17}$$

where $\omega_1 = \sqrt{(k_1 + \kappa)/m_1}$, $\omega_2 = \sqrt{(k_2 + \kappa)/m_2}$ and:

$$\Gamma = \frac{\sqrt{\kappa/m_1}\sqrt{\kappa/m_2}}{\sqrt{\omega_1\omega_2}}. \tag{4.18}$$

We seek solutions for Eq. 4.17 with $k_1 = k_0$, $k_2 = k_0 + \Delta k$ and $m_1 = m_2 = m_0$. Fig. 4.4a illustrates the case where there is no coupling ($\kappa = 0$). When the coefficient Δk is increased from $-k_0$ to k_0, the frequency of the oscillator 1 stays constant and the frequency of the oscillator 2 increases from zero to $\sqrt{2}\omega_0$. At $\Delta k = 0$, the two dispersion curves intersect.

Fig. 4.4b shows the dispersion curves corresponding to the presence of coupling ($\kappa \neq 0$). In this case, the two curves do not intersect any more. Instead, there is

a characteristic *anticrossing* of the dispersion curves with a:

$$[\omega_+ - \omega_-] = \Gamma. \tag{4.19}$$

This anticrossing is the main proof of the strong coupling regime. We note that Γ is proportional to κ and that the Rabi splitting increases with the coupling strength.

4.2 Microcavity polaritons

4.2.1 Definition in quantum physics

In this section, the physics of semiconductor microcavities in the strong coupling regime, known as microcavity polaritons, will be reviewed. We take the point of view of the quantum mechanics to express the features of the strong coupling in terms of energy [148].

We consider an atomic system with two levels, a ground level $|g\rangle$ and an excited level $|e\rangle$ with the energies E_1 and E_2 from the ground level. This system is considered in an optical cavity, with an electromagnetic resonant mode with the transition $e - g$. We only consider two possible states in the cavity: the state $|0\rangle$ without photon, and the state $|1\rangle$ with a photon in the cavity. The atom-photon system with the Hamiltonian H_0 has two excited states with the same energy, $|e, 0\rangle$ (the atom is in its excited state without photon) and $|g, 1\rangle$ (the atom is in its ground state with a photon), above the ground state $|g, 0\rangle$ (Fig. 4.5). The eigenvalues E_1 and E_2 of the Hamiltonian H_0 are also:

$$\begin{cases} H_0 |e, 0\rangle = E_1 |e, 0\rangle , \\ H_0 |g, 1\rangle = E_2 |g, 1\rangle . \end{cases} \tag{4.20}$$

To take into account an external perturbation of the system, we denote a new Hamiltonian as:

$$H = H_0 + W. \tag{4.21}$$

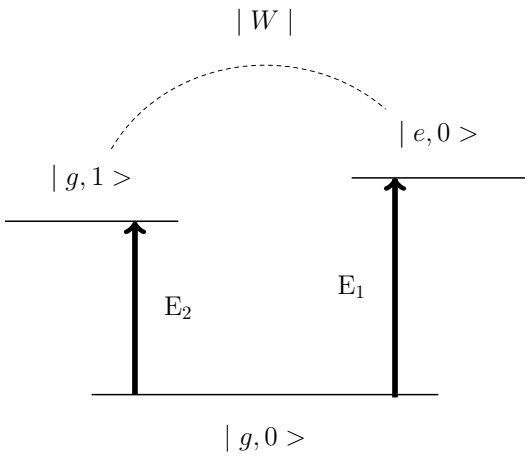

Figure 4.5: Energy diagram of the atom-cavity system.

The eigenstates and eigenvalues of H are $|\Phi_\pm\rangle$ and $E_\pm$, respectively:

$$\begin{cases} H\left|\Phi_+\right\rangle = E_+\left|\Phi_+\right\rangle, \\ H\left|\Phi_-\right\rangle = E_-\left|\Phi_-\right\rangle. \end{cases} \tag{4.22}$$

H_0 is called the non-perturbed Hamiltonian, and W is the perturbation, also called the coupling. We suppose that W does not depend on the time. In the basis $\{|e,0\rangle, |g,1\rangle\}$ of the eigenstates of H_0, W is the following hermitian matrix:

$$W = \begin{pmatrix} W_{11} & W_{12} \\ W_{21} & W_{22} \end{pmatrix}, \tag{4.23}$$

where W_{11} and W_{22} are real and $W_{12} = W_{21}^*$.

In the absence of coupling, E_1 and E_2 are the energies of the system, and $|e,0\rangle$ and $|g,1\rangle$ are stationary states. The problem consists in determining the modifications due to the coupling W. A consequence of the coupling is that a measure of the energy of the system can only give one of the eigenvalues E_+ and E_- of the Hamiltonian H. These eigenvalues are generally not equal to E_1 and E_2.

The first step in the resolution of this problem consists to calculate E_+ and E_- as a function of E_1, E_2 and the matrix elements of W. We also study the effect

of the coupling on the position of the energy levels. The next step consists in to determining the corresponding eigenstates $|\Phi_+\rangle$ and $|\Phi_-\rangle$ of the system.

So, in the base $\{|e,0\rangle, |g,1\rangle\}$, the Hamiltonian in the matrix form is:

$$H = \begin{pmatrix} E_1 + W_{11} & W_{12} \\ W_{21} & E_2 + W_{22} \end{pmatrix}. \tag{4.24}$$

The corresponding eigenvalues are:

$$E_\pm = \frac{1}{2}(E_1 + W_{11} + E_2 + W_{22}) \pm \frac{1}{2}\sqrt{(E_1 + W_{11} - E_2 - W_{22})^2 + 4 \mid W_{12} \mid^2}, \tag{4.25}$$

and the corresponding eigenstates are:

$$\begin{cases} |\Phi_+\rangle = \cos\frac{\theta}{2}|e,0\rangle + \sin\frac{\theta}{2}|g,1\rangle, \\ |\Phi_-\rangle = -\sin\frac{\theta}{2}|e,0\rangle + \cos\frac{\theta}{2}|g,1\rangle, \end{cases} \tag{4.26}$$

where the angle θ is defined as:

$$\tan\theta = \frac{2 \mid W_{12} \mid}{E_1 + W_{11} - E_2 - W_{22}} \quad \text{with } 0 \leq \theta < \pi. \tag{4.27}$$

We admit now that the light-matter coupling between the two states only includes the non-diagonal terms, which are positive and real:

$$\begin{cases} \langle g,1|W|e,0\rangle = \langle e,0|W|g,1\rangle > 0, \\ \langle e,0|W|e,0\rangle = \langle g,1|W|g,1\rangle = 0. \end{cases} \tag{4.28}$$

Eqs. 4.25 and 4.27 become:

$$E_\pm = \frac{1}{2}(E_1 + E_2) \pm \frac{1}{2}\sqrt{(E_1 - E_2)^2 + 4 \mid W_{12} \mid^2}, \tag{4.29}$$

$$\tan\theta = \frac{2 \mid W_{12} \mid}{E_1 - E_2} \quad \text{with } 0 \leq \theta < \pi. \tag{4.30}$$

We denote $E_m = (E_1 + E_2)/2$ and $\Delta = (E_1 - E_2)/2$. The variation of the parameter E_m implies to put the origin on the energy axis. The eigenstates do not depend on E_m. The significant parameter is Δ. As a function of Δ, the two

energies of the system are:

$$E_{\pm} = E_m \pm \sqrt{\Delta^2 + \mid W_{12} \mid^2}. \tag{4.31}$$

The energies E_+ and E_- are two branches of a symmetric hyperbola separated by a distance $2 \mid W_{12} \mid$. In absence of coupling, the two curves for E_1 and E_2 intersect at $\Delta = 0$. In the presence of coupling, the two curves for E_+ and E_- do not intersect anymore. There is again the characteristic anticrossing of the strong coupling regime.

Thus, whatever the value of Δ, we always have $\mid E_+ - E_- \mid > \mid E_1 - E_2 \mid$. The coupling of the system increases the distance between the eigenfrequencies. The separation between them is the Rabi splitting, noted W_{12} here.

Near the asymptotes, $\mid \Delta \mid >> \mid W_{12} \mid$ and the eigenvalues can be written as:

$$E_{\pm} = E_m \pm \Delta \left(1 + \frac{1}{2} \mid \frac{{W_{12}}^2}{\Delta} + \cdots \right). \tag{4.32}$$

The characteristic angle (Eq. 4.30) becomes $\theta \simeq 0$ (we suppose $\Delta \geq 0$) and the eigenstates are:

$$\begin{cases} |\Phi_+\rangle = |e,0\rangle + \dfrac{\mid W_{12} \mid}{\Delta} |g,1\rangle + \cdots \\ |\Phi_-\rangle = |g,1\rangle - \dfrac{\mid W_{12} \mid}{\Delta} |e,0\rangle + \cdots \end{cases} \tag{4.33}$$

In this case, the perturbed states are not really different to the non-perturbed ones. The strong coupling cannot be established in these regions.

In the center of the hyperbola, of $\Delta = 0$ ($E_1 = E_2$), the coupling becomes strong and eigenvalues are:

$$E_{\pm} = E_m \pm \mid W_{12} \mid . \tag{4.34}$$

The effect of the coupling is more important when the two levels have the same energy. The characteristic angle (Eq. 4.30) becomes $\theta \simeq \pi/2$ and the eigenstates are:

$$\begin{cases} |\Phi_+\rangle = \dfrac{1}{\sqrt{2}}[|e,0\rangle + |g,0\rangle], \\ |\Phi_-\rangle = \dfrac{1}{\sqrt{2}}[-|e,0\rangle + |g,0\rangle]. \end{cases} \tag{4.35}$$

In the strong coupling, the perturbed states become really different to the non-

perturbed ones. They are a linear superposition of the initial eigenstates.

The temporal evolution of the system is found by considering Schrödinger's equation:

$$i\hbar\frac{\mathrm{d}}{\mathrm{d}t}\left|\Phi(t)\right\rangle = (H_0 + W)\left|\Phi(t)\right\rangle, \tag{4.36}$$

where $\left|\Phi(t)\right\rangle = a_1(t)\left|e,0\right\rangle + a_2(t)\left|g,1\right\rangle$ is the eigenstate of the system at the time t. In the base $\{\left|e,0\right\rangle, \left|g,1\right\rangle\}$:

$$\begin{cases} i\hbar\dfrac{\mathrm{d}}{\mathrm{d}t}a_1(t) = E_1 a_1(t) + W_{12}a_2(t), \\ i\hbar\dfrac{\mathrm{d}}{\mathrm{d}t}a_2(t) = W_{21}a_1(t) + E_2 a_2(t). \end{cases} \tag{4.37}$$

In the presence of coupling ($\mid W_{12} \mid \neq 0$), these equations constitute a linear system of homogeneous differential coupled equations. To determine the temporal evolution of the states, we consider the system in the state $\left|\Phi(0)\right\rangle = \left|e,0\right\rangle$ at $t = 0$. In the base $\{\left|\Phi_+\right\rangle, \left|\Phi_-\right\rangle\}$, $\left|\Phi(0)\right\rangle$ can be written as:

$$\left|\Phi(0)\right\rangle = \cos\left(\frac{\theta}{2}\right)\left|\Phi_+\right\rangle - \sin\left(\frac{\theta}{2}\right)\left|\Phi_-\right\rangle. \tag{4.38}$$

At a given time t, the system is in the state $\left|\Phi(t)\right\rangle$:

$$\left|\Phi(t)\right\rangle = \cos\left(\frac{\theta}{2}\right)e^{-iE_+t/\hbar}\left|\Phi_+\right\rangle - \sin\left(\frac{\theta}{2}\right)e^{-iE_-t/\hbar}\left|\Phi_-\right\rangle. \tag{4.39}$$

The probability $P_{12}(t)$ to find the system in the state $\left|g,1\right\rangle$ is deduced from $P_{12}(t) = \mid \left\langle g,1 \mid \Phi(t)\right\rangle \mid^2$:

$$P_{12}(t) = \frac{1}{2}\sin^2\theta\left[1 - \cos\left(\frac{E_+ - E_-}{\hbar}t\right)\right] = \sin^2\theta\sin^2\left(\frac{E_+ - E_-}{2\hbar}t\right). \tag{4.40}$$

With Eqs 4.29, the probability $P_{12}(t)$ becomes:

$$P_{12}(t) = \frac{4 \mid W_{12} \mid^2}{4 \mid W_{12} \mid^2 + (E_1 - E_2)^2}\sin^2\left[\sqrt{4 \mid W_{12} \mid^2 + (E_1 - E_2)^2}\frac{t}{2\hbar}\right]. \tag{4.41}$$

This expression of the probability is called the Rabi formula.

4.2.2 Review on the strong coupling regime

In microcavities

When a single emitter is placed in a cavity, it is demonstrated that the spontaneous emission rate can be greatly modified due to the Purcell effect, and even vacuum Rabi splitting can be achieved. The Rabi splitting is illustrated in the previous section and simply called a "frequency splitting". Indeed, if we consider a system with two coupled states of energy, the electromagnetic field periodically oscillates between two localized states inside the structure [55, 149, 150, 151]. In quantum semiconductor microcavity, the Rabi oscillations were first experimentally observed in 1994 [152].

In the weak coupling regime, the interaction between the exciton and the cavity photon is irreversible, as an excited exciton cannot transfer its energy back to the cavity and the oscillations exponentially decrease. As a consequence of the Purcell effect, the optical properties of an electronic state are not intrinsic to the state but depend on the electromagnetic field that couples the state. Fermi's golden rule states that the rate of spontaneous emission is proportional to the density of photon states at the spatial position of the exciton. The radiative lifetime of an exciton in an optical microcavity can either be extended or reduced with respect to its lifetime in vacuum.

The strong coupling regime occurs if the coupling coefficient is larger than any of the dissipation rates in the system. This regime was first experimentally demonstrated in GaAs quantum wells by C. Weisbuch [55]. The research on the strong coupling regime has been strongly extended due to the interest in coherent and stimulated effects in such systems, which can lead to optical devices, as it is shown in the overview by R. Houdré *et al.* [153]. Strong coupling implies a periodic exchange between the energies of the atom and the cavity at the Rabi splitting, under the resonant condition, where the Rabi frequency in turn depends on the coupling factor of the system [154, 155, 156]. The time evolution and the interaction between the emitter and the cavity can no longer be described by Fermi's golden rule. The excitonic and confined photon modes cannot be considered independent eigenmodes of the system. The normal modes are a linear and coherent superposition of the exciton and photon states. The anticrossing between the exciton and the photon modes is also related to the Rabi splitting.

With organic materials

The excitonic state has a low saturation density [157] and can generally be ionized at room temperature. These features often limit the observation and study of the strongly coupled state to low temperatures and small excitation densities. The low exciton oscillator strength results in small Rabi splittings that are typically 6-10 meV [158, 159]. The strong coupling regime in microcavities recently has expanded been to microcavities containing thin layers of organic materials [160], such as J-aggregates of cyanine dyes or zinc-porphyrin [161, 162]. Organic materials possess a number of interesting physical properties relevant to strong coupling that contrast with those of inorganic semiconductors. Because of the relatively large oscillator strengths of the organic exciton, anticrossings larger than 100 meV at room temperature have been reported [163, 164, 165].

Strong coupling was first demonstrated in organic materials by D. G. Lidzey *et al.* [161] using tetra-(2,6-t butyl) phenol-porphyrin zinc (4TBPPZn), in polystyrene located in a planar microcavity. This demonstration took place at room temperature, with a Rabi splitting > 100 meV. The large Rabi splitting obtained in organic microcavities are of particular significance for current efforts to achieve polariton lasing in microcavities at room temperature, because it will be possible to maintain the strong coupling at 300K.

An even more interesting organic material still is the J-aggregates for which the strong coupling was also demonstrated by D. G. Lidzey [166]. Indeed, this organic material has narrow absorption in the red and near infrared frequencies which makes many applications possible. The Rabi splitting is increased with a large oscillator strength [167, 168], but also with the possibility of increasing the absorption coefficient [169].

Concerning the methods, the majority of these experiments has been carried out at room temperature with angular-resolved reflectivity measurements corroborated by transfer-matrix simulations [170, 171, 168, 161, 162, 169].

Involving surface plasmons

In the strong coupling regime, Fermi's golden rule fails and coherent dynamics dominate. SP modes provide an alternative route to enhance the coupling and extend to nanoscale. The corresponding Rabi splitting, for example in the strong

coupling between SP modes and J-aggregates which have a particularly narrow absorption linewidth, is demonstrated in [172, 173, 174] and is always higher than 100 meV.

Using the Kretschmann geometry [5, 13], the strong coupling regime with SP mode is possible with a wide variety of organic molecules, such as the Rhodamine 6G, for which the Rabi splitting can be equal to 400 meV [175, 176]. It is also demonstrated that the coupling strength is proportional to the square root of the molecular density, which is an important mechanism for SERS (Surface enhanced Raman scattering) [177]. In addition, it is proved that the high local field amplitudes generated by SPs of the metallic structures also has an important impact on the result, and more precisely, on the value of the Rabi splitting. The strong coupling of SP modes with a sulforhodamine 101 dye [178] or β-carotene in a nanolayered system [179] extend the potential applications in biology, with a Rabi splitting that remains high, between 130 meV and 360 meV. Other possibilities involve a Fabry-Pérot metallic device [180], metallic nanowire [181, 182] or metamaterials [183], with a Rabi splitting higher than 250 meV.

The values of the measured Rabi splitting have to be taken with precaution as reminded in [184]. Indeed, due to the large interaction energies, the calculations at a constant angle can induce an overestimation of the Rabi splitting of more than a factor of 2. Most of the experiments consist of the measurement of the reflectivity as a function of the incidence angle [185, 172, 186, 176, 182] (angle-resolved reflectivity spectra) within a theoretical model based on the transfer matrix method [187]. Some works also present the absorption curves in order to study the evolution of the losses of the modes when the strong coupling regime occurs [186, 176].

But the stringent condition of strong coupling requires that the coupling coefficient be larger than any of the dissipation rates in the system. A key feature of many approaches is to reduce the effective mode volume of the cavity, thereby achieving a substantial increase in the coupling strength, which is inversely proportional to the square root of the mode volume [188]. Compared with a normal photonic cavity, a plasmonic cavity has smaller mode volumes and higher field enhancement to provide an important platform for cavity quantum electrodynamics investigations [189, 190]. For applications such as quantum information processing, a large Rabi splitting is especially important for coherent manipulation of mixed

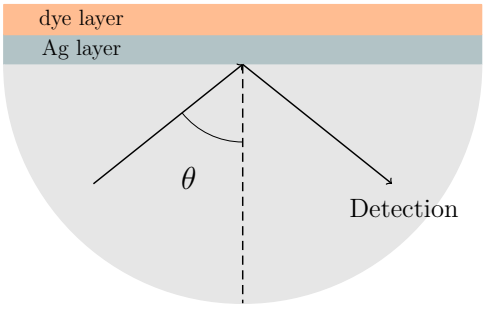

Figure 4.6: Illustration of the device used to allow reflectometry experiment and to obtain a strong coupling regime between surface plasmons (Ag) and excitons (J-aggregates): a dielectric prism with a silver film of thickness $e_m = 45$ nm, a small layer of TiO_2 of thickness $e_{TiO_2} = 2$ nm, and a layer containing the cyanide dye J-aggregates of thickness $e_c = 35$ nm.

states [191].

Otherwise, another interesting configuration implies Tamm plasmon-polaritons [46]. These modes can be directly excited with light wave because their in-plane wave vector is less than the wave vector of light in vacuum. They can also be formed in both TM and TE polarizations. Their existence was theoretically demonstrated at the interface between two periodic dielectric planar multilayer structures [192] and more recently at the interface between a metallic layer and a Bragg mirror [193]. Their first experimental observation between a metal and dielectric Bragg reflector was reported in [47] and their experimental observation in strong coupling regime with an exciton from inorganic quantum wells was reported in [194]. A Rabi splitting energy of 11.5 meV was found.

From now, we consider more precisely the strong coupling between surface plasmons and excitons in an organic semiconductor [172, 184, 186]. We use the tetrachotomy method to find the same results, and thus, to validate our method. First, the device consists of a layer containing the cyanide dye J-aggregates which has been deposited on a silver film (Fig. 4.6), the whole being embedded between a dielectric (a prism) and air. A very small layer of TiO_2 is placed between the dye and the metallic layers in order to allow the experimental realization of the device. The SP is excited in a similar way as in the ATR structure. It is on the interface between the active layer and the air (see Fig. 4.6).

In order to observe the interaction between the surface plasmon and the exci-

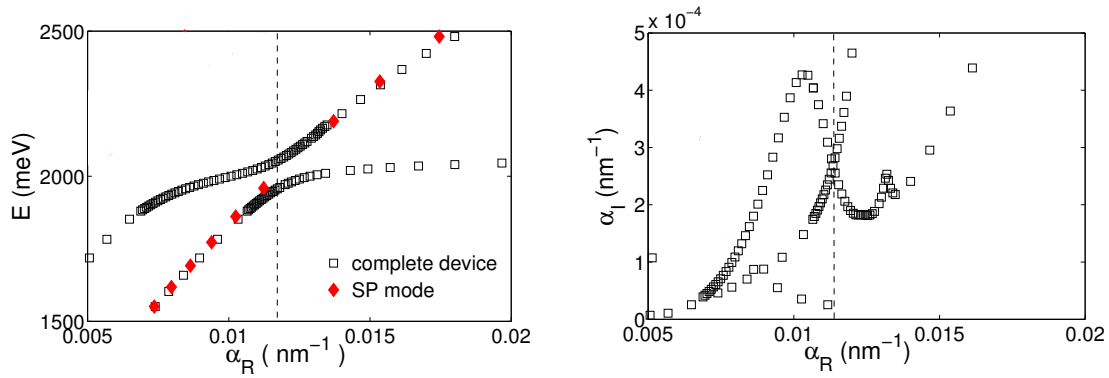

(a) (b)

Figure 4.7: Dispersion and absorption relations obtained with the tetrachotomy: (a) Energy dependence of the modes E as a function of the propagation constant α_R with an anticrossing of the dispersion curves. In red, the dispersion curve of the SP mode in the device without the dye layer. The Rabi splitting is $E_R = 174$ meV [172]. (b) The absorption of the modes α_I as a function of α_R with a crossing of the absorption curves at the same value of the anticrossing of the dispersion curves. The modes exchange energy and are hybrid modes, mixed modes of the initial ones.

tons, it is necessary that the dispersion curves of the SP mode and the exciton mode can cross. With the J-aggregates, the exciton does not have dispersion. Its energy is constant and equal to approximately 2100 meV. It is possible to demonstrate that if a too thin dye layer is used, the absorption is not sufficient to obtain a strong coupling regime. The metallic thickness is equal to approximately 35 nm which is not a too important thickness as compared to the penetration depth $\delta_{dye} = 23$ nm, which allows the SP excitation (at the wavelength $\lambda = 600$ nm).

The result we obtained is plotted in Fig. 4.7a. There is an anticrossing of the dispersion curves associated with a crossing of the absorption curves (obtained with the imaginary part of the propagation constant), at the same propagation constant (Fig. 4.7b). Theses two phenomena are proof of the strong coupling regime between the plasmon and the exciton modes. The crossing of the absorption curves is necessary to justify the transfer of energy between the modes. The Rabi splitting expected is 180 meV [172]. We found a Rabi splitting $E_R = 174$ meV, in keeping with its value.

4.3 Strongly coupled SP and guided modes

Most structures that have been used to enhance the plasmon emission consist of adding gain in a dielectric medium, with a metallic film directly deposited on it [41, 42]. The only progress in the field has been in the depth penetration of the plasmon in the two media. This is a drawback that needs to improved, as we want the SP emission, and it is necessary to use relatively high values of gain in order to obtain a notable enhancement. The configuration we propose here allows to put gain into the medium between the SP mode which is strongly coupled with a guided mode. The strong coupling regime allows a very significant improvement of the SP emission, as we will discuss in Section 4.4. In this section, we demonstrate the strong coupling regime between the guided and SP modes, and study the properties of the hybrid modes which are created.

4.3.1 The device

We consider the structure as illustrated in Fig. 4.8. This is a stratified medium which is composed of a dielectric waveguide, which contains a guided mode GM deposited on a metallic film which supports two surface plasmons, SP_u and SP_d. This configuration allows the interaction between the guided mode GM and the SP_d mode as we are going to show.

The dielectric waveguide is composed of the experimental values of the permittivities. The core of the waveguide has a dielectric permittivity $\varepsilon_g = 4.84$ ($n_g = 2.20$) which corresponds to the permittivity of SiO_2 at the wavelength $\lambda = 650$ nm. The cladding of the waveguide also has a dielectric permittivity $\varepsilon_d = 2.1025$ ($n_d = 1.45$), which corresponds to the permittivity of TiO_2 at the same wavelength. The two materials are possible to be experimentally made in thin films, as it is showed in [195].

The dielectric permittivity for the metallic film is again taken from the Palik data [81] for silver and the dielectric permittivity for the transmitted medium is $\varepsilon_t = 3$. This last value is arbitrary and allows to keep down the dispersion curve of the SP_u mode so as to not hinder the other dispersion curves. The choice of taking into consideration a metallic film rather than an semi-infinite metallic bulk is justified by the aim of obtaining a more realistic result. The influence of the SP_u mode is negligible so long as the dielectric medium (with ε_t) has a dielectric

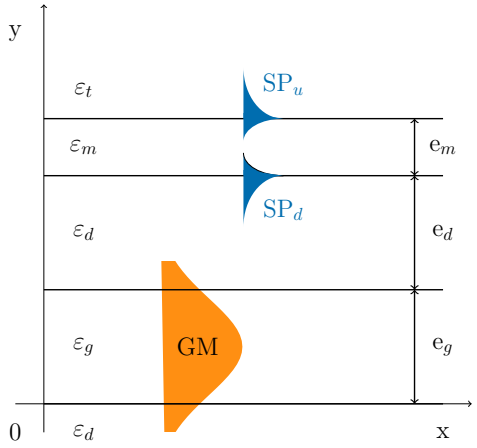

Figure 4.8: Planar guided structure which allows a strong coupling regime between the surface plasmon SP_d and the guided mode GM. The permittivities of each of the layers are $\varepsilon_d = 2.1025$, $\varepsilon_g = 4.84$, $\varepsilon_t = 3$, and ε_m is taken from the Palik data [81] for silver. The thickness of the core of the waveguide e_g and the metallic thickness e_m are fixed. Only the thickness e_d, the distance between the two coupled modes, has to change in order to determine the best configuration for the strong coupling regime.

permittivity higher than the cladding of the waveguide (with ε_d).

The coupled plasmons/guided mode dispersions can be represented with a coupled oscillator model [196]. The dispersion relations are obtained by diagonalizing the plasmons-guided mode Hamiltonians:

$$H = \begin{pmatrix} E_{GM} - i\gamma_{GM} & V_{SP_d}/2 & 0 \\ V_{SP_d} & E_{SP_d} - i\gamma_{SP_d} & 0 \\ 0 & 0 & E_{SP_u} - i\gamma_{SP_u} \end{pmatrix}, \tag{4.42}$$

where E_{GM} is the guided mode energy, γ_{GM} is the guided mode linewidth, E_{SP_d} and E_{SP_u} are the SP modes energies, γ_{SP_d} and γ_{SP_u} are the plasmon linewidth and V_{SP_d} is the interaction energy between the SP_d mode and the guided mode GM.

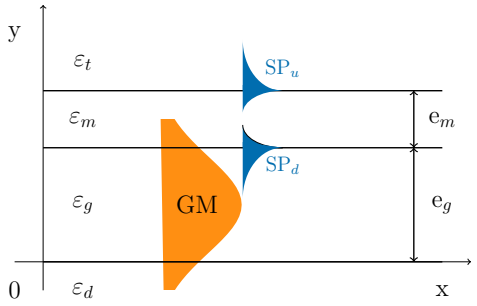

Figure 4.9: Planar guided structure when $e_d = 0$ nm. This configuration does not allow an interaction between the surface plasmon SP_d and the guided mode GM.

4.3.2 Variation of the characteristic parameters

Variation of the thickness e_d

In our study, we always consider a real frequency ω and a complex propagation constant, defined by $\alpha = \alpha_R + i\alpha_I$. α_R is the real part and corresponds to the usual propagation constant. That is why, we will always directly name it the propagation constant.

We take into account the structure of Fig. 4.8 and fix the thicknesses e_g and e_m. The distance e_g is chosen to have a quasi mono-mode in the waveguide in the visible range, $e_g = 130$ nm. The thickness of the metallic film is $e_m = 45$ nm, a usual thickness for a metallic layer.

We recall that the strong coupling regime is characterized by an anticrossing of the dispersion curves and a crossing of the absorption curves. Plotting the dispersion curves corresponding to Fig. 4.8 with different values for e_d allows to see the characteristic anticrossing of the dispersion curves.

First, if $e_d = 0$ nm, the metallic film is directly deposited on the core of the waveguide (Fig. 4.9). The corresponding dispersion curves and absorption curves are plotted in Fig. 4.10. The dispersion curve of GM is confined between the two light lines and the dispersion curve of SP_d is always below the dashed light line

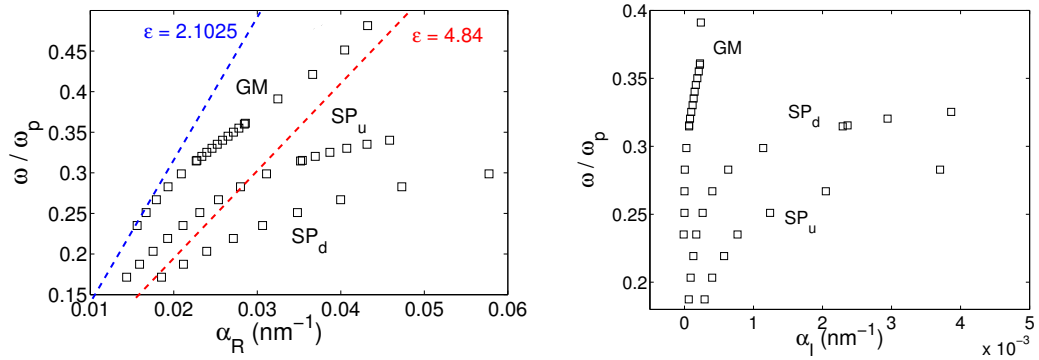

(a) (b)

Figure 4.10: (a) Dispersion curves if $e_d = 0$ nm: the frequency ω, normalized to the plasma frequency ω_p, as a function of the propagation constant α_R. The dotted line and the dashed line represent the light lines for $\varepsilon_d = 2.1025$ and $\varepsilon_g = 4.84$, respectively. The dispersion curve of GM is confined between the two light lines and the dispersion curve of SP_d is always below the dashed light line ($\varepsilon_g = 4.84$) because of the intrinsic properties of the surface plasmons which are non-radiative modes. In this case, the GM and SP_d modes cannot interact. (b) Absorption curves if $e_d = 0$ nm: the frequency ω, normalized to the plasma frequency ω_p, as a function of the imaginary part of the propagation constant α_I.

($\varepsilon_g = 4.84$), because of the intrinsic properties of the surface plasmons which are non-radiative modes. There exists an inherent momentum mismatch between the two modes GM and SP_d, so they do not interact. The absorption curves also do not cross, there is no coupling.

Next, the other extreme case is if e_d is too large. The corresponding dispersion curves and absorption curves are plotted in Fig. 4.11. The two parts of the structure can be considered separately (Fig. 4.12): in black points, the dispersion curves of the structure when $e_d = 200$ nm; in red and blue crosses, the dispersion curves of the two parts of the structure determined independently. The dispersion curves are pretty equivalent, the crossing occurs at $\alpha_R = 0.028$ nm^{-1}. This is the uncoupled case.

We note the value of the propagation constant corresponding to the crossing of the dispersion curves in Fig. 4.11a: $\alpha = 0.028$ nm^{-1} for a wavelength $\lambda = 421.5$ nm ($\omega/\omega_p = 0.325$ with $\omega_p = 1.374 \times 10^{16}$ for silver). This is the region for which the modes can interact. The dielectric permittivity of the metallic layer taken from the Palik data [81] for $\lambda = 421.5$ nm is $\varepsilon_m = -4.8 + 0.728 * i$. Note that the absolute value of the effective index corresponding to the SP_d and GM modes are almost

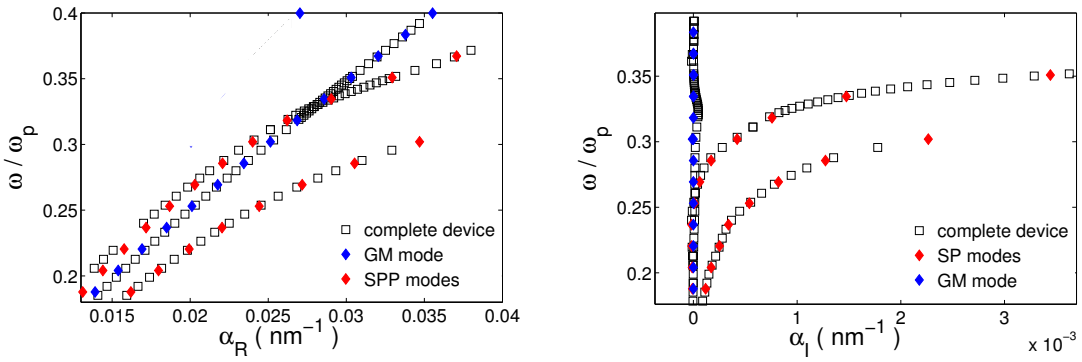

(a) (b)

Figure 4.11: (a) Dispersion curves if $e_d = 200$ nm: the frequency ω, normalized to the plasma frequency ω_p, is plotted as a function of the propagation constant α_R. The black-square curve represents the dispersion relation of all the structure illustrated in Fig. 4.8. The red- and blue-diamond curves represent the dispersion relations for the two parts of the structure considered independently: in red, a metallic film embedded between media with the dielectric permittivities ε_d and ε_t; in blue, a waveguide with the dielectric permittivities ε_g and ε_d (Fig. 4.12). (b) Absorption curves if $e_d = 200$ nm: the frequency ω, normalized to the plasma frequency ω_p, is plotted as a function of the imaginary part of the propagation constant α_I.

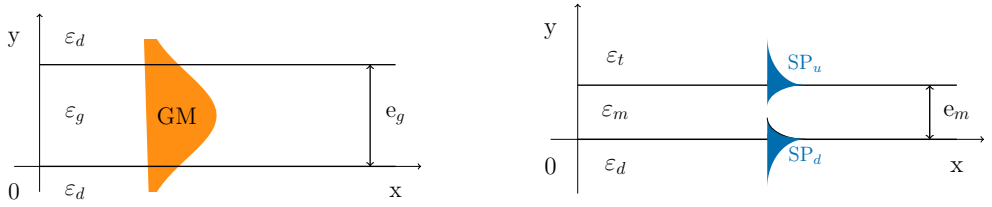

(a) (b)

Figure 4.12: The two parts of the complete structure considered separately: (a) the dielectric waveguide; (b) the metallic film in a non-symmetric medium.

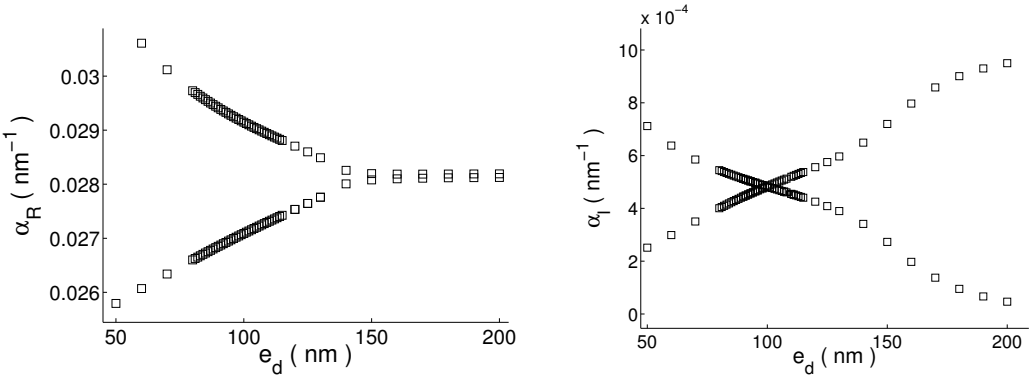

(a) (b)

Figure 4.13: (a) The propagation constant α_R as a function of the distance e_d. The splitting between the curves for the GM and SP_d modes decreases with the increase of e_d. (b) The imaginary part of the propagation constant α_I as a function of the distance e_d. The crossing of the absorption curves for the GM and the SP_d modes occurs at $e_d = 100$ nm, the optimal value to obtain a strong coupling regime between the GM and SP_d modes.

equal at this wavelength. This is an important condition in order to obtain the coupling. We plot the propagation constants of the three modes as a function of the thickness e_d at the wavelength $\lambda = 421.5$ nm in Fig. 4.13a. Without surprise, the splitting between the GM and SP_d modes decreases with the increase of the distance e_d.

To find the corresponding value of the strong coupling regime, we have to consider the absorption curves which are deduced from the imaginary parts α_I of the propagation constant. This is the reason why the tetrachotomy method is useful, since it allows to find the poles of the S-matrix with simultaneously the real and imaginary parts. Fig. 4.13b shows the imaginary parts α_I corresponding to the propagation constants as a function of the distance e_d. The crossing of the two absorption curves for GM and SP_d corresponds to the strong coupling between the two modes. The GM mode sees its absorption increases, when the absorption for the SP_d mode decreases, until the intersection for $e_d = 100$ nm.

The structure evolves from the case in which the SP_d mode cannot be directly excited by the GM when $e_d = 0$ nm, to the uncoupled case where the two modes are too far from each other to interact. Between these two extreme cases, there is a range for the distance e_d where the SP_d mode can exist in the medium characterized by ε_d, because e_d becomes higher than its penetration length. In this range, the

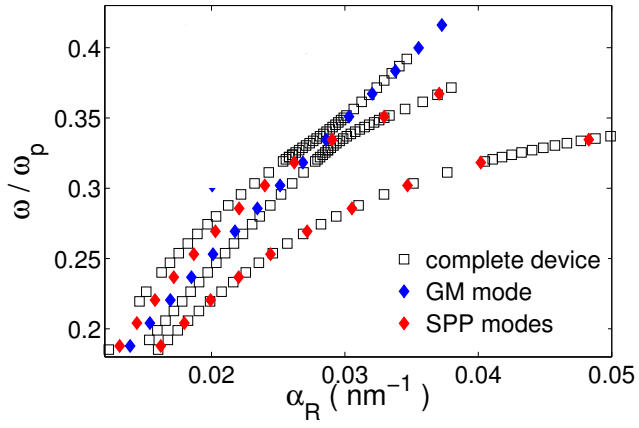

Figure 4.14: Dispersion curves if $e_d = 100$ nm, the optimal thickness for obtaining the strong coupling regime: the frequency ω, normalized to the plasma frequency ω_p, is plotted as a function of the propagation constant α_R. In blue and red, the dispersion curves of the modes before the coupling with a crossing between them. The anticrossing of the dispersion curves (black squares) is a feature of the strong coupling between the GM and SP_d modes. The new modes also created are hybrid modes between the initial ones. The Rabi splitting is $E_R = 134$ meV.

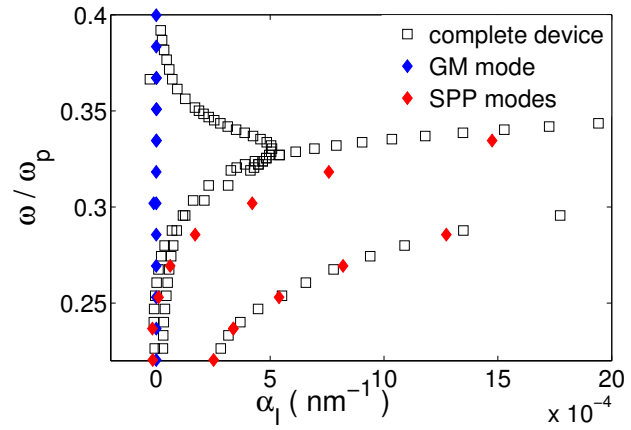

Figure 4.15: Absorption curves if $e_d = 100$ nm, the optimal thickness for obtaining the strong coupling regime: the frequency ω, normalized to the plasma frequency ω_p, is plotted as a function of the imaginary part of propagation constant α_I. The crossing of the absorption curves is another feature of the strong coupling between the GM and SP_d modes. GM exchanges energy with SP_d and its losses increase when the losses for the surface plasmon decrease if we compare with the blue and red curves corresponding of the modes before the coupling.

SP_d mode can interact with the GM mode. Its dispersion curve can cross the one of the guided mode. We note that the behavior of the SP_u mode is independent from the parameter e_d.

We plot the dispersion curves and the absorption curves for $e_d = 100$ nm in Figs. 4.14 and 4.15, respectively. We also see the characteristic anticrossing of the dispersion curves of GM and SP_d, with a deformation of the curves as compared to the uncoupled ones. The two modes corresponding to the propagation constant $\alpha_R = 0.028$ nm^{-1} are new modes of the structure, hybrid modes between the initial modes. We denote them $SP_{d,c}$ and GM_c the lower and the higher modes at the wavelength $\lambda_l = 421.5$ nm and $\lambda_h = 405$ nm, respectively. The Rabi splitting is $E_R = 134$ meV.

This anticrossing is associated to the crossing of the absorption curves at the same value of the propagation constant $\alpha_R = 0.028$ nm^{-1}. The frequency is plotted as a function of the imaginary part of the propagation constant, so as to better see the movement of the absorption curves between the uncoupling case and the strong coupling case with the crossing. This crossing is another feature of the strong coupling regime. However, the coupling implies a guided mode which does not have losses and a surface plasmon which has intrinsic losses. We also see that the exchange of energy between these modes involves an increase of the losses for GM and, at the same time, the decrease of the losses for SP_d. GM gives energy to SP_u. The propagation length has to be enhanced in this configuration, as we will see.

The possibility of obtaining a strong coupling regime between SP_d and GM modes has been demonstrated. We will study the properties of the hybrid modes $SP_{d,c}$ and GM_c in Part 4.3.3. In particular, we need to verify whether or not the $SP_{d,c}$ mode is still a surface mode, and to quantify its confinement.

Variation of the range of frequency

The result obtained previously can be transposed to other ranges of frequency without losing in generalities. The strong coupling regime can be obtained with an appropriate modulation of the distance between the core of the waveguide and the metallic film.

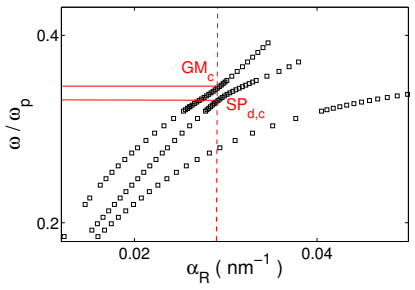

Figure 4.16: Range of the frequencies enabling to observe temporal oscillations in the strong coupling regime at the propagation constant $\alpha_R = 0.028$ nm^{-1}.

4.3.3 Numerical results for the optimal coupling

Temporal oscillations of the modes

The direct consequence of the strong coupling regime is temporal oscillations. Theses oscillations correspond to the case in which we consider a constant value of the propagation constant and observe the variations of the corresponding frequencies as illustrated in Fig 4.16. These can be observed with the Finite Difference Time Domain (FDTD) method. We adapt it to the case of dispersive media to take the metallic film into account. Details about the implementation of the FDTD method are given in appendix A.

We consider the complete device (Fig. 4.8) in the case of the strong coupling regime between the SP_d and the GM modes when the distance $e_d = 100$ nm. The temporal oscillations between the hybrid modes $SP_{d,c}$ and GM_c are represented in Fig. 4.17. The size of the cell is $\Delta l = 5$ nm and the corresponding time step is $\Delta t = \Delta l/(2c)$, with c the speed of light in vacuum. The permittivity of the metallic layer is taken from the Drude model. The magnitude of the field corresponding to the plasmon mode is lower than the magnitude of the field in the waveguide. The period of the oscillations is $T_t = 30.7$ fs[1].

Fig. 4.18 illustrates snapshots of the structure when the elapsed time is $t_1 = 62.5$ fs and $t_2 = 83$ fs. In Fig. 4.18a, the $SP_{d,c}$ mode is excited for the first time when in Fig. 4.18b, the surface plasmon mode is excited again after one period T_t.

[1]If we consider the energy as $E = \hbar\omega = \hbar 2 * pi/T_t$, we find $E_R = 134.7$ meV.

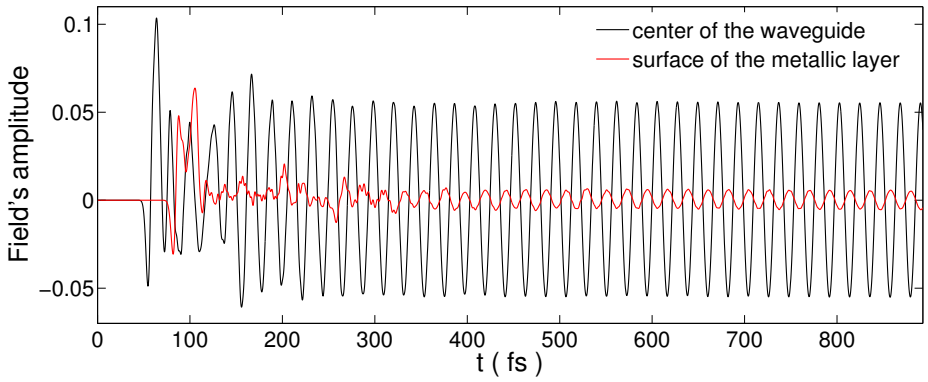

Figure 4.17: Temporal oscillations between the hybrid modes deduced from the FDTD calculations. The period of the oscillations is $T_t = 30.7$ fs.

Spatial oscillations of the modes

In the case of the strong coupling between plasmons and excitons recalled in the previous section, the initial excitons do not have dispersion so their dispersion relation is constant depending on the propagation constant. The temporal oscillations between the modes can be easily observed or determined with the coupled-mode theory. In the case of our complete device (Fig. 4.8), which allows the strong coupling between plasmons and guided modes, the inclination of the dispersion relations in comparison with the non-dispersive plane implies the possibility of observing spatial oscillations, as we will present in this part.

The aim is to excite only the modes in a precise range of the propagation constant, including the two hybrid modes (Fig. 4.19). The range of the gaussian beam is reduced and we name it an evanescent gaussian beam.

We consider the complete device (Fig. 4.8) in the case of the strong coupling regime between the SP_d and the GM modes when the distance $e_d = 100$ nm. The spatial oscillations between the hybrid modes $SP_{d,c}$ and GM_c are represented in Fig. 4.20, with a dielectric permittivity of the metallic film taken from the Drude model. We see oscillations between the two modes and can already observe a good confinement for the hybrid $SP_{d,c}$ mode, the energy of the guided mode being transferred to the hybrid plasmon $SP_{d,c}$ which spends twice less time on the metallic surface. Its intrinsic decay has to be reduced.

This result is calculated from the Drude model and is idealized. If we consider

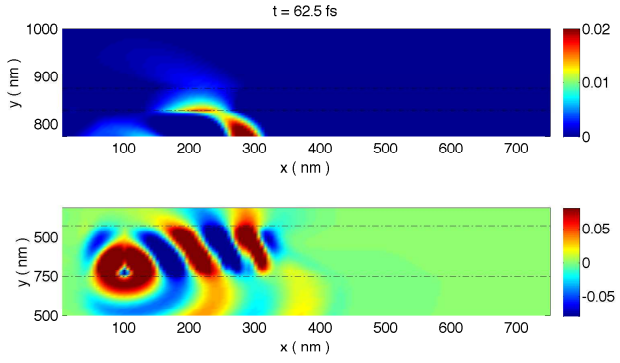

(a)

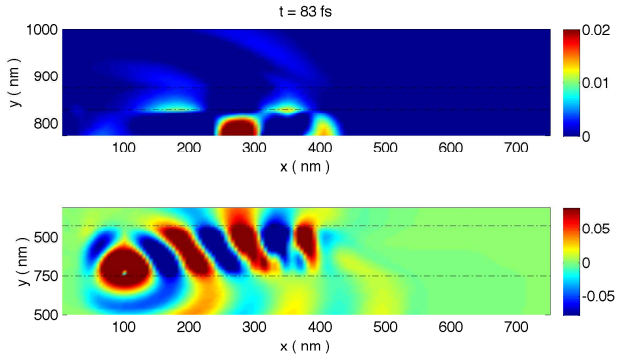

(b)

Figure 4.18: Snapshots of the structure after two elapsed times: (a) $t_1 = 62.5$ fs, the SP_d mode is excited for the first time. (b) $t_2 = 83$ fs, the SP_d mode is excited again after one period T_t. The structure is mapped in two parts because of the relative weakness of the field's amplitude for the surface mode, as compared to the guided mode.

the Palik data [81] for calculating the permittivity of the metallic layer, the result is shown in Fig. 4.21. The spatial oscillations between the modes are no longer as marked and a steady state of the system is difficult to see. This result shows that the spatial oscillations are present, but the losses of the metal rapidly attenuate the field. Fig. 4.22 illustrates in one dimension the spatial oscillations between the two modes, with the Drude model and the Palik data. The period of the oscillations is $T_s = 1.7\mu$m.

With an evanescent gaussian beam, we can also observe the modes far away from the region of the strong coupling regime. Fig. 4.23a shows the region of the dispersion relation we want to observe. We are looking to excite the fundamental

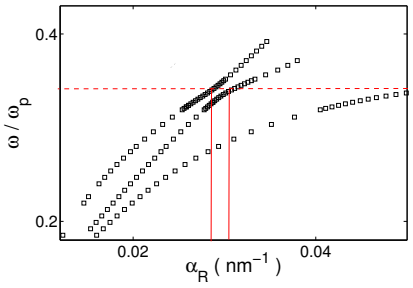

Figure 4.19: Range of the propagation constant, including the two hybrid modes in order to observe spatial oscillations between them, at the wavelength $\lambda_l = 421.5$ nm.

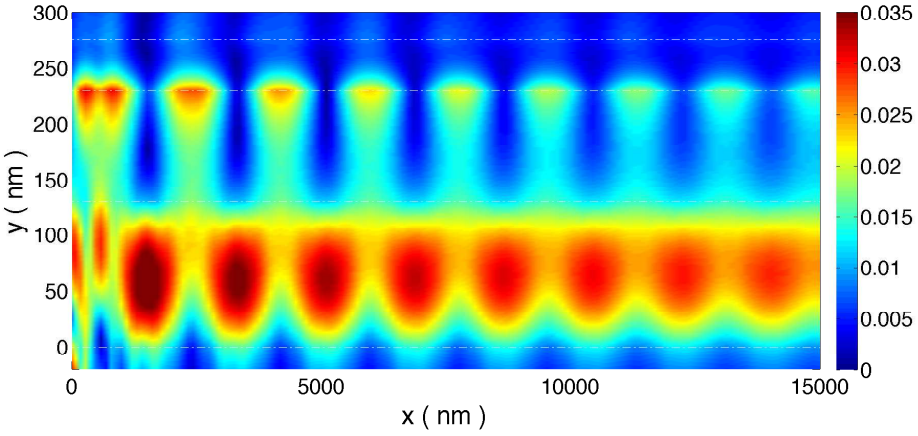

Figure 4.20: Map of the field with an incident evanescent gaussian beam used to observe the spatial oscillations in the complete structure when $e_d = 100$ nm. The metallic permittivity ε_m is taken from the Drude model. The energy of the hybrid guided mode is transferred to the hybrid plasmon which passes approximatively twice less time on the metallic surface. Its intrinsic decay has to be reduced.

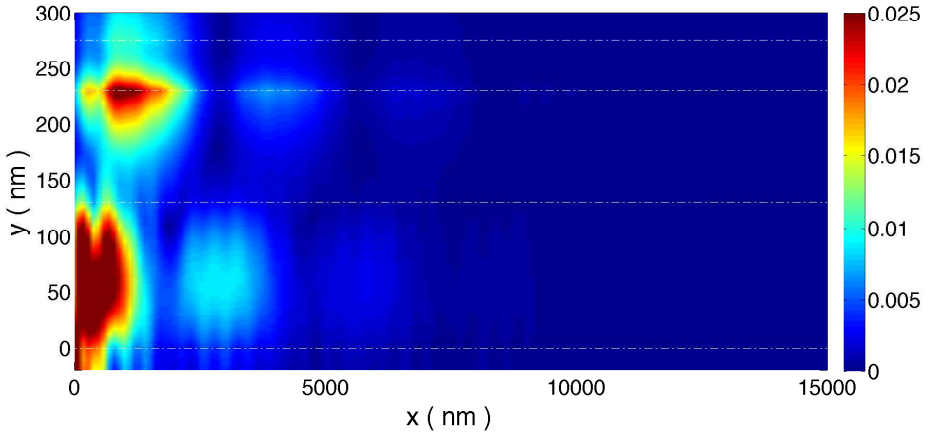

Figure 4.21: Spatial oscillations between the two hybrid modes when the strong coupling regime occurs, using the Palik data for the metallic permittivity [81]. The propagation length of the hybrid $SP_{d,c}$ mode is approximatively 1μm, against only 400 nm in the uncoupled case.

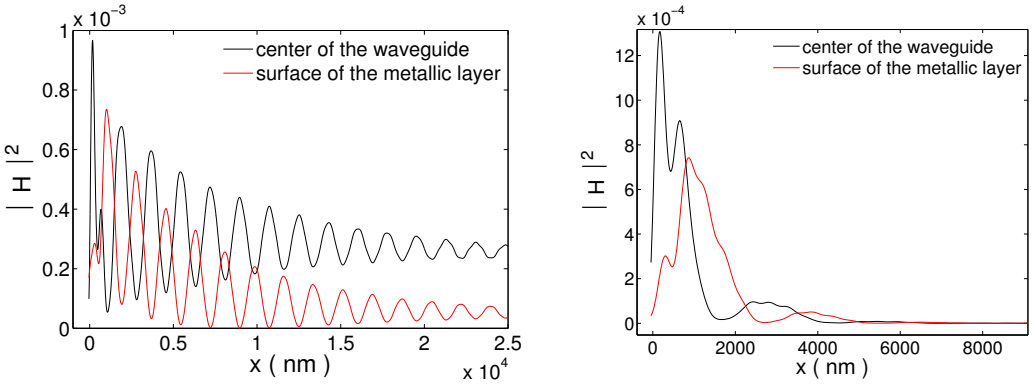

(a) (b)

Figure 4.22: Spatial oscillations between the two hybrid modes when the strong coupling regime occurs (a) with the Drude model and (b) the Palik data for silver permittivity [81]. GM_c exchanges energy with $SP_{d,c}$, with a period $T_s = 1.7\mu$m.

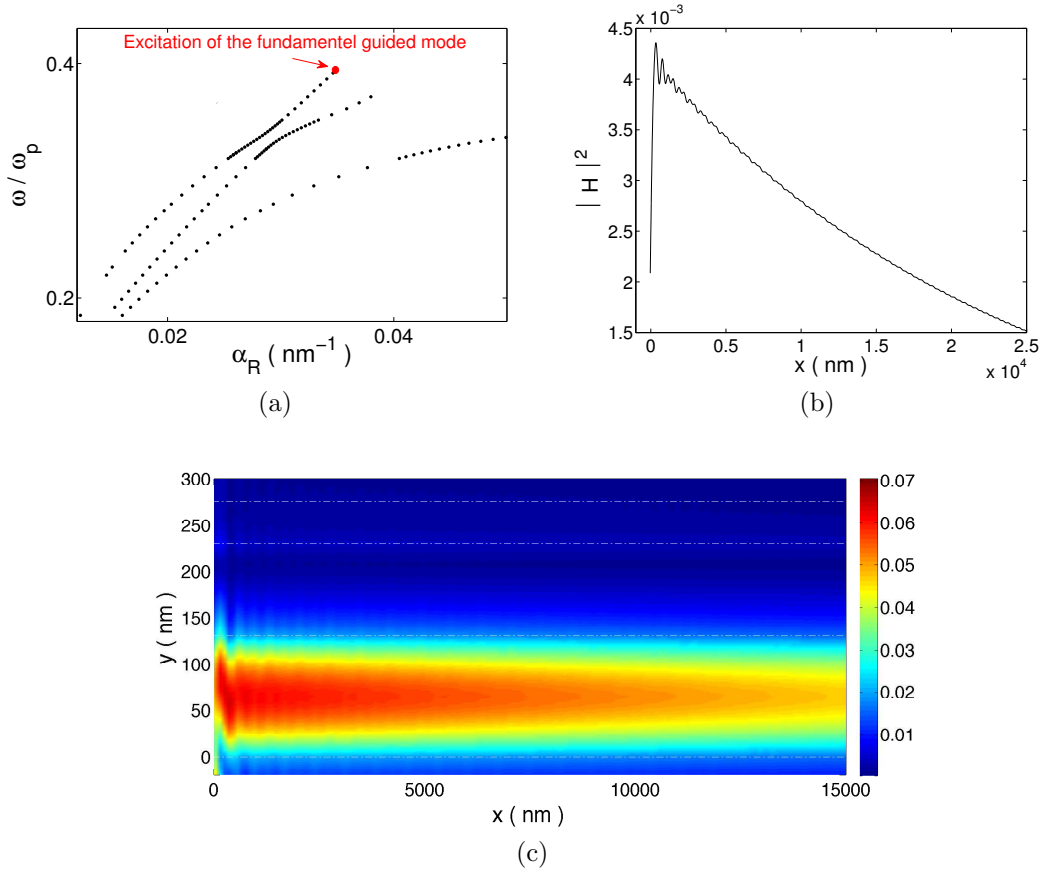

Figure 4.23: The fundamental guided mode far away from the anticrossing, excited by an evanescent gaussian beam with the Palik data [81]. (a) In the dispersion curves, we consider the point noted by a red dot characterized by $\alpha_R = 0.0346$ nm^{-1}, at a wavelength $\lambda = 349.5$ nm. (b) In one dimension, the intensity of the field in the center of the waveguide. (c) The corresponding map of the field in the plane (x, y).

guided mode. Once again, we use the Palik data for the metallic permittivity [81]. In Fig. 4.23b, the intensity of the field in the center of the dielectric waveguide is plotted as a function of the distance x. The corresponding map of the field is in Fig. 4.23c. Having no losses, the guided mode has a propagation length and a shape strongly related to what was expected.

Confinement of the $SP_{d,c}$ mode

The confinement of the $SP_{d,c}$ mode relates to the depth penetration of the surface plasmon in the dielectric, with ε_d ($\varepsilon_d = 2.1025$). Theoretically, the depth pene-

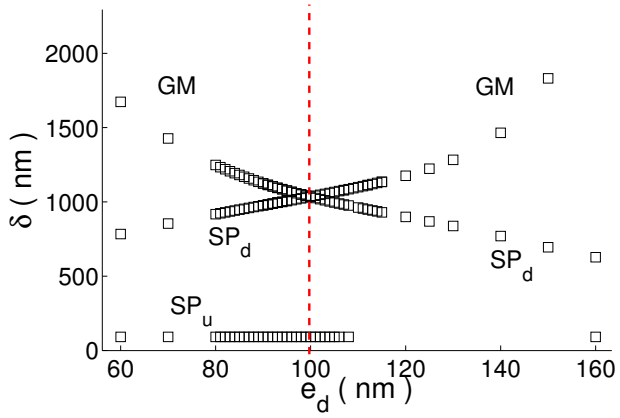

Figure 4.24: Propagation length δ as a function of the distance e_d for the modes in the complete structure (Fig. 4.8) for $\lambda_l = 421.5$ nm. The crossing of the curves corresponds to the maximum of the propagation length for the $SP_{d,c}$ mode, what occurs for $e_d = 100$ nm, $\delta_{SP} = 1036$ nm.

tration of an uncoupled SP in this configuration is $\delta_{d,uncoupled} = 80$ nm. With the maps of the field (Figs. 4.20 and 4.21), we deduced that the field of $SP_{d,c}$ mode decays of $1/e$ along the y-direction after a distance $\delta_d \sim 50$ nm. The confinement of the plasmon is fairly good, better than the one in an uncoupled structure. The hybrid mode also created is still a surface mode and keeps the main property of the classical SPs.

Enhancement of the propagation length

In Fig. 4.21, the hybrid $SP_{d,c}$ mode has a propagation length equalling approximatively to 1μm, when in the uncoupled case[2], its propagation length is only 400 nm. To confirm this result, we use the tetrachotomy method to determine the propagation constant as a function of the thickness e_d at the wavelength $\lambda_l = 421.5$ nm. The result is plotted in Fig. 4.24.

For a SP mode at the interface between a metallic medium with ε_m (ε_m is taken from the Palik data) and a dielectric medium with ε_d ($\varepsilon_d = 2.1025$), the theoretical propagation length (Eq. 2.13) is 300 nm. The crossing of the curves corresponds to the maximum of the propagation length for the $SP_{d,c}$ mode that occurs for $e_d = 100$ nm, $\delta_{SP_{d,c}} = 1036$ nm. The table 4.1 includes the propagation

[2]The uncoupled structure is a metallic layer embedded between a two dielectric media with the permittivities ε_d and ε_a (see Fig. 4.12b)

uncoupled SP	**strongly coupled SP**
δ_{SP_d}(theoretical)= 300 nm	$\delta_{SP_{d,c}}$(map of the field)$\sim$ 1000 nm
δ_{SP_d}(tetrachotomy)= 400 nm	$\delta_{SP_{d,c}}$(tetrachotomy)= 1036 nm
δ_{SP_u}(theoretical)= 94 nm	
δ_{SP_u}(tetrachotomy)= 91 nm	

Table 4.1: Propagation lengths obtained in different manners for the uncoupled/strongly coupled SP_d and the uncoupled SP_u, when $\lambda_l = 421.5$ nm. For the uncoupled case, the match between the theory and the tetrachotomy method is pretty good. The propagation length of $SP_{d,c}$ in the strong coupling regime is calculated with the tetrachotomy method and verified with the map of the field.

lengths obtained in different manners for the uncoupled/strongly coupled SP_d and the uncoupled SP_u. The propagation length for $SP_{d,c}$ increases by more than a factor of two, as compared to the uncoupled case. This result is encouraging for enhancing the plasmon emission.

The same study can be carried out at the wavelength $\lambda_h = 405$ nm. The crossing of the curves corresponding to the maximum of the propagation length for the $SP_{d,c}$ mode is $\delta_{SP_{d,c}} = 1200$ nm, and occurs for $e_d = 100$ nm.

4.4 Adding gain in the strongly coupled structure

We consider the complete device of Fig. 4.8 with a distance $e_d = 100$ nm that allows the strong coupling regime between the guided and surface modes. We look the two wavelength $\lambda_l = 421.5$ nm and $\lambda_h = 405$ nm which correspond to the lower and the higher branches at the anticrossing. They are related to the hybrid $SP_{d,c}$ and GM_c modes, respectively, and that is verified for this part. We also consider a distance e_d corresponding to the maximum propagation length of the surface mode for the wavelength: $\lambda_l = 421.5$ nm is associated with $e_d = 100$ nm; $\lambda_h = 405$ nm is associated with $e_d = 110$ nm. The gain we are going to apply will always be within the nanometer range. We check that the break of the PT symmetry (see Section 3.3) for two coupled dielectric waveguides, with $\varepsilon_g = 4.84 \pm ig\lambda/(2\pi)$, embedded in media, with $\varepsilon_d = 2.1025$ takes place for higher values than the ones we used. The critical value of the gain that corresponds to the break of the PT symmetry

e_d	λ	$SP_{d,c}$	GM_c
100 nm	421.5 nm	$\delta_{SP} = 16.3$ μm $g_n = 0.4522$ $g = 6.7 * 10^{-3}$ nm^{-1}	$\delta_{GM} = 202.4$ μm $g_n = 0.2733$ $g = 4.1 * 10^{-3}$ nm^{-1}
110 nm	405 nm	$\delta_{SP} = 1$ μm no notable variation with the gain	$\delta_{GM} = 7722$ μm $g_n = 0.1018$ $g = 1.6 * 10^{-3}$ nm^{-1}

Table 4.2: Maximum of the propagation lengths of $SP_{d,c}$ and GM_c as a function of the gain, added in the core of the waveguide, and for the notable wavelengths $\lambda_l = 421.5$ nm (with $e_d = 100$ nm) and $\lambda_h = 405$ nm (with $e_d = 110$ nm). The dielectric permittivity of the core of the waveguide is changed such as $\varepsilon_g = 4.84 - i * g_n$. There is no notable variation of the propagation length of the $SP_{d,c}$ mode with the added gain.

is $g \sim 400$ nm.

4.4.1 Adding gain in the core of the waveguide

Gain is added in the core of the dielectric waveguide. Its dielectric permittivity becomes:

$$\varepsilon_g = 4.84 - i * g_n, \tag{4.43}$$

where g_n is the normalized gain with $g_n = (\lambda/2\pi)g$, and g the gain in nm^{-1}.

Fig. 4.25 illustrates the propagation length δ as a function of the normalized gain g_n in the core of the waveguide when the wavelength is $\lambda_l = 421.5$ nm and $e_d = 100$ nm.

Although the excitation at this wavelength matches the $SP_{d,c}$ mode, the propagation length δ_{GM} of the GM_c mode is higher than the propagation length δ_{SP} of the $SP_{d,c}$ mode, since the gain is inserted in the core of the waveguide. We have $\delta_{GM} = 202.4$ μm, whereas $\delta_{SP} = 16.3$ μm. The increase of the propagation length of the surface mode exists but it is not notable. The increase of normalized gain beyond 1 does not enable to obtain another maximum of the propagation length. There is a limit to the enhancement of the propagation length in this configuration.

Fig. 4.26 shows δ as a function of the normalized gain g_n when $\lambda_h = 405$ nm and $e_d = 110$ nm. The predominant mode becomes the GM_c mode at this wavelength. The maximum of its propagation length is $\delta_{GM} = 7.7$ mm, a very high value as compared to the 1 μm obtained when the strong coupling between

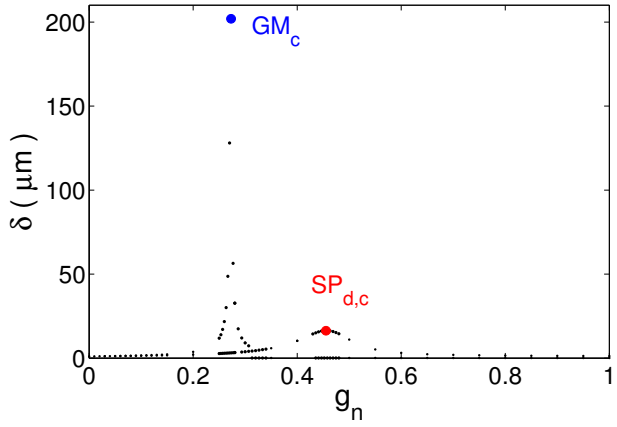

Figure 4.25: The propagation length δ of the modes as a function of the gain in the core of the waveguide when $\lambda_l = 421.5$ nm and $e_d = 100$ nm. The maximum of the propagation lengths are $\delta_{GM} = 202.4$ μm for $g_n = 0.2733$ and $\delta_{SP} = 16.3$ μm for $g_n = 0.4522$.

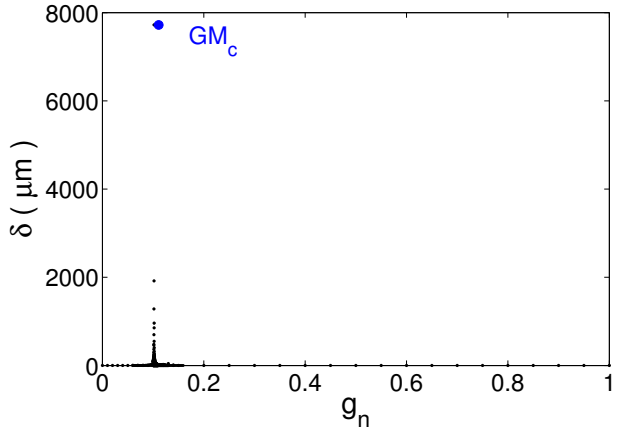

Figure 4.26: The propagation length δ of the modes as a function of the gain in the core of the waveguide when $\lambda_h = 405$ nm and $e_d = 110$ nm. The maximum of the propagation length for the GM_c mode is $\delta_{GM} = 7722$ μm for $g_n = 0.1018$.

e_d	λ	$SP_{d,c}$	GM_c
100 nm	421.5 nm	$\delta_{SP} = 6461\ \mu$m $g_n = 0.1031$ $g = 1.5 * 10^{-3}$ nm^{-1}	$\delta_{GM} = 4149\ \mu$m $g_n = 0.118$ $g = 1.8 * 10^{-3}$ nm^{-1}
110 nm	405 nm	$\delta_{SP} = 1435\ \mu$m $g_n = 0.1578$ $g = 2.4 * 10^{-3}$ nm^{-1}	$\delta_{GM} = 4400\ \mu$m $g_n = 0.1386$ $g = 2.2 * 10^{-3}$ nm^{-1}

Table 4.3: Maximum of the propagation lengths of $SP_{d,c}$ and GM_c as a function of the gain added into the dielectric layer between the two strongly coupled modes, and for the notable wavelengths $\lambda_l = 421.5$ nm (with $e_d = 100$ nm) and $\lambda_h = 405$ nm (with $e_d = 110$ nm). The dielectric permittivity of the dielectric layer is changed such as $\varepsilon_d = 2.1025 - i * g_n$.

this mode and the surface plasmon occurs. The propagation length of the surface mode is not amplified at all, $\delta_{SP} = 1\ \mu$m. The results are summarized in table 4.2.

This configuration cancels the losses for the guided mode due to the strong coupling with the SP_d mode. The propagation length δ_{SP} of the $SP_{d,c}$ can be enhanced sixteen times as compared to the strong coupling case without gain, but the introduction of gain in the medium between the two strongly coupled modes has to improve the SP mode.

4.4.2 Adding gain in the medium between the two strongly coupled modes

We add gain in the medium of permittivity ε_d, with the thickness e_d, between the two strongly coupled modes. Fig. 4.27 shows the propagation length δ of the modes as a function of the normalized gain g_n in the layer, when $\lambda_l = 421.5$ nm and $e_d = 100$ nm. At this wavelength, the $SP_{d,c}$ mode is predominant and its propagation length is $\delta_{SP} = 6461\ \mu$m for $g_n = 0.1031$.

The propagation length δ of the modes when $\lambda_h = 405$ nm and $e_d = 110$ nm is plotted in Fig. 4.28. The propagation length corresponding to the guided mode δ_{GM} stays almost constant at the two wavelengths when δ_{SP} goes down 1435 μm when $\lambda_h = 405$ nm. The results are summarized in table 4.3.

The understanding of the improvement of propagation lengths passes by the study of the evolution of the dispersion and absorption curves (Figs. 4.29 and 4.30), as well as the evolution of the poles in the complex plane (α_R, α_I), plotted

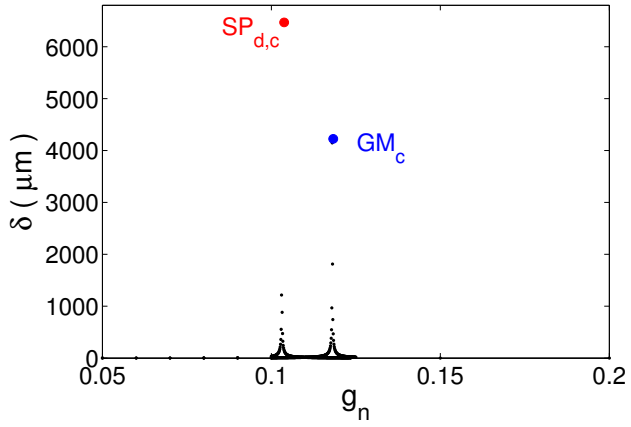

Figure 4.27: The propagation length δ of the modes as a function of the gain in the layer between the two strongly coupled modes when $\lambda_l = 421.5$ nm and $e_d = 100$ nm. The maximum of the propagation lengths are $\delta_{GM} = 4149$ μm for $g_n = 0.118$ and $\delta_{SP} = 6461$ μm for $g_n = 0.1031$.

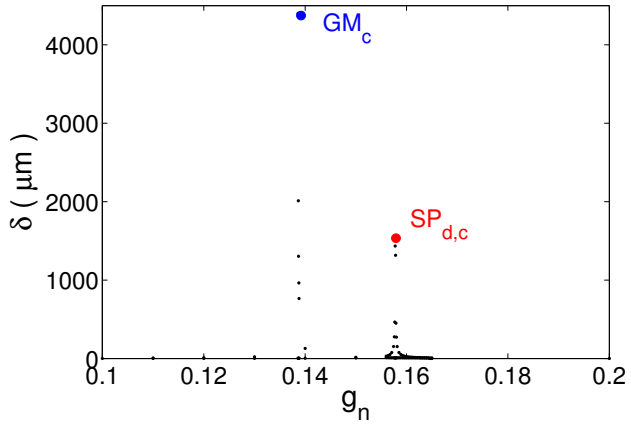

Figure 4.28: The propagation length δ of the modes as a function of the gain in the layer between the two strongly coupled modes when $\lambda_l = 405$ nm and $e_d = 110$ nm. The maximum of the propagation lengths are $\delta_{GM} = 4400$ μm for $g_n = 0.1386$, and $\delta_{SP} = 1435$ μm for $g_n = 0.1578$.

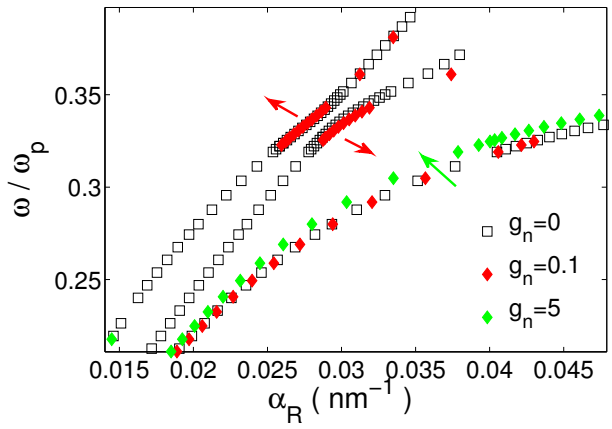

Figure 4.29: Dispersion curves of the complete device as a function of the gain in the dielectric layer between the two strongly coupled modes. First, the anticrossing increases up to a normalized gain $g_n = 0.14$. Then, the dispersion curve of the SP_u mode moves towards lower values of the propagation constant.

in Fig. 4.31.

The anticrossing of the dispersion curves (Fig. 4.29) increases with the gain to attain a Rabi splitting $E_{R,a} = 145$ meV, when $g_n = 0.14$, when the losses for the surface mode are the most compensated. The crossing of the absorption curves (Fig. 4.30) moves to lower losses with the increase of the gain, and reaches almost zero when $g_n = 0.14$. The conservation of the crossing up to this value of the gain is a proof of the strong coupling regime between these modes despite the added gain.

The poles of the S-matrix plotted in the complex plane (α_R, α_I) move as a function of the gain. First, the poles corresponding to the hybrid coupled modes move down until reaching the real axis, when $g_n = 0.14$. Then, these poles do not evolve anymore, whereas the poles for the SP_u mode move towards a minimum of absorption, before a new increase of the losses with a decreasing propagation constant (as is confirmed with the dispersion curve).

Fig. 4.32 represents the map of the field obtained with an incident evanescent beam for observing the spatial oscillations, for a gain $g_n = 0.1031$ at the wavelength $\lambda_l = 421.5$ nm. The metallic permittivity ε_m is taken from the Palik data [81]. The energy of the hybrid guided mode is transferred with an amplified dielectric separating medium to the hybrid plasmon. The period of the oscillations increases

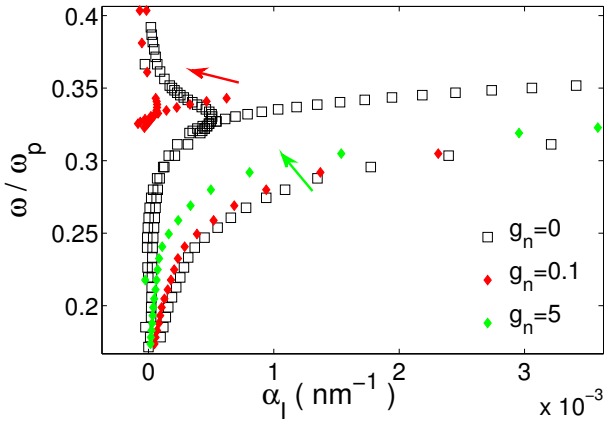

Figure 4.30: Absorption curves of the complete device as a function of the gain in the dielectric layer between the two strongly coupled modes. First, the crossing moves towards lower values of the absorption up to a normalized gain $g_n = 0.14$. Then, the absorption curve of the SP_u mode also moves towards lower values of the absorption.

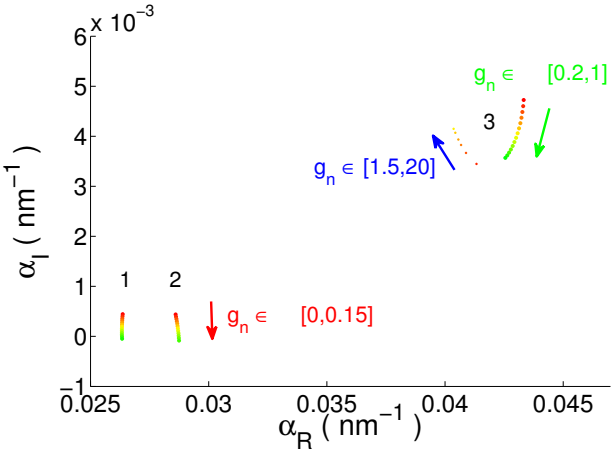

Figure 4.31: Poles of the S-matrix of the complete device in the strong coupling, as a function of the gain in the dielectric layer between the two strongly coupled modes. The hybrid guided mode GM_c and the hybrid surface mode $SP_{d,c}$ are noted 1 and 2 without gain, respectively. The upper surface mode SP_u is noted 3. First, the poles corresponding to the hybrid coupled modes move down until attaining the real axis when $g_n = 0.14$. Then, these poles do not move anymore, whereas the poles for the SP_u mode move towards a minimum of absorption, before a new increase of the losses, with a decreasing propagation constant.

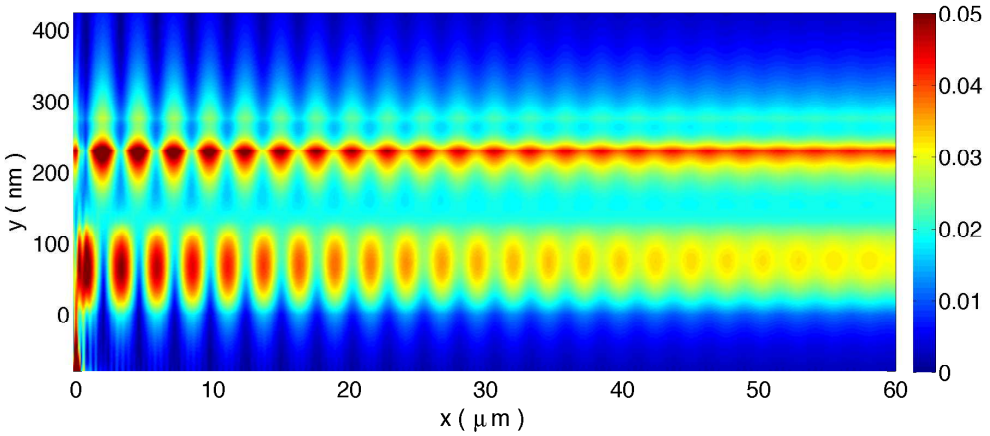

Figure 4.32: Map of the field obtained with an incident evanescent beam to observe the spatial oscillations for a gain $g_n = 0.1031$ at the wavelength $\lambda_l = 421.5$ nm. The metallic permittivity ε_m is taken from the Palik data [81]. The energy of the hybrid guided mode is transferred with an amplified dielectric separating medium to the hybrid plasmon. The period of the oscillations is $T_{s,a} = 2.6$ μm.

to $T_{s,a} = 2.6$ μm, whereas the spatial oscillations with the Palik data for the metal rapidly vanish without gain (Fig. 4.21). The amplitude of the field corresponding to the hybrid plasmon becomes greater than the amplitude of the hybrid guided mode, which is coherent with a greater propagation length in this configuration.

The results obtained in Figs. 4.26, 4.25, 4.28 and 4.27 are with a constant value of the wavelength (421.5 or 405 nm). If we consider Fig. 4.30, we see that at a given value of frequency, we do not follow the crossing of the absorption curves. The two successive peaks in the plot of the propagation length as a function of the added gain also correspond to both quasi-coupled modes which have different values of propagation constant.

Fig. 4.33 shows the propagation length δ of the hybrid modes as a function of the gain in the layer between both strongly coupled modes when the wavelength changes with the crossing of the absorption curves as a function of the added gain. We find that the propagation length increases until the value we consider as the limit in the plot of the poles in the complex plane (Fig. 4.31), $g_n = 0.14$. The propagation length for the hybrid plasmon is $\delta_{SP_{d,c}} = 1237$ μm. Fig. 4.34 represents the map of the field obtained with an incident evanescent beam for observing the spatial oscillations, for a gain $g_n = 0.14$ at the wavelength $\lambda_l = 409$ nm, the corresponding value of the wavelength to the crossing of the absorption

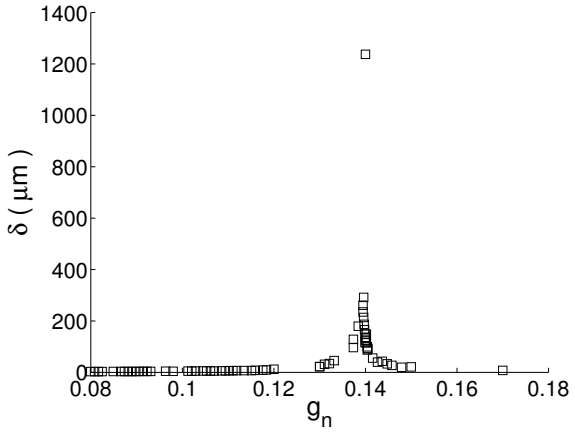

Figure 4.33: The propagation length δ of the hybrid modes as a function of the gain in the layer between both strongly coupled modes when the wavelength corresponds to the crossing of the absorption curves as a function of the added gain. The maximum of the propagation lengths are at the same value of the propagation constant, $\delta_{SP_{d,c}} = 1237$ μm.

curves. After this critical value, the gain starts to enhance the emission of the SP_u mode (Fig. 4.30).

4.4.3 Adding gain without a strong coupling device

The necessity of a device, which allows a strong coupling regime, is demonstrated with the plot of the propagation length as a function of the gain in two cases: firstly, an incident medium with a permittivity ε_d and a layer of thickness e_d with a permittivity $\varepsilon = \varepsilon_d - i * g_n$ deposited directly against the metallic layer; secondly, an incident medium directly with the gain, $\varepsilon = \varepsilon_d - i * g_n$ against the metallic layer. The results are summarized in Table 4.4. In both cases, the increase of the propagation length for the SP_d mode is not comparable to the result obtained with the complete waveguide in strong coupling regime.

In conclusion, we demonstrate the possibility to enhance the SP emission in the strong coupling regime with added gain. Next, the necessity of the strong coupling configuration for obtaining this improvement has also been demonstrated. It is important to note that the surface plasmon SP_d is not the most efficient type of plasmon we can obtain in the visible range[3], because it is taken too high on the dispersion curve. However, it is easy to observe with these characteristic

[3]as compared to the SP in the air for a wavelength $\lambda = 633$ nm)

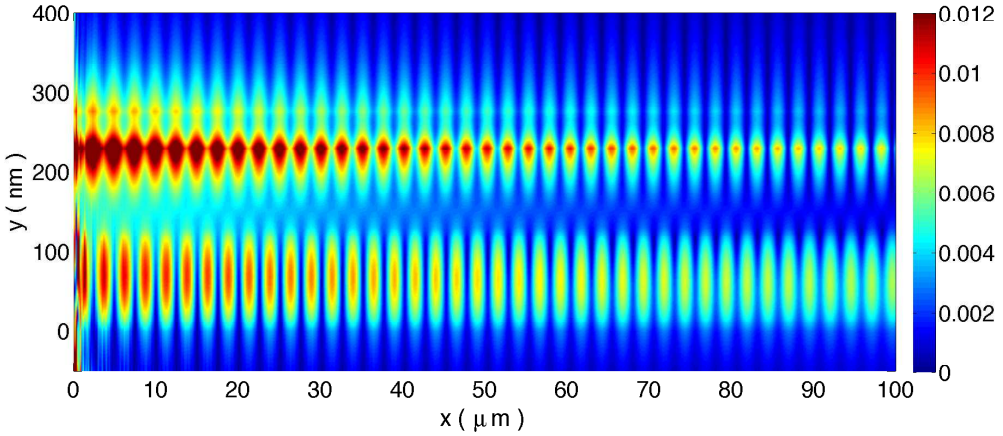

Figure 4.34: Map of the field obtained with an incident evanescent beam to observe the spatial oscillations for a gain $g_n = 0.14$ at the wavelength $\lambda_l = 409$ nm, the corresponding value of the wavelength to the crossing of the absorption curves.

e_d	λ	δ_{SP_u}	g_n
100 nm	421.5 nm	3.38 μm	$g_n = 0.15$
110 nm	405 nm	36.1 μm	$g_n = 0.12$
no e_d	421.5 nm	3.9 μm	$g_n = 0.15$
no e_d	405 nm	12.9 μm	$g_n = 0.11$

Table 4.4: Maximum of the propagation lengths of $SP_{d,c}$ as a function of the gain without the dielectric waveguide (no layer with $\varepsilon_g = 4.84$) and for the notable wavelengths $\lambda_l = 421.5$ nm (with $e_d = 100$ nm) and $\lambda_h = 405$ nm (with $e_d = 110$ nm). The dielectric permittivity of the dielectric layer is changed as $\varepsilon_d = 2.1025 - i * g_n$. Then, the dielectric permittivity of the incident medium is changed in the same way without a layer before the metal.

distances. The result is still instructive for imagining device for enhancing the SP emission such as the surface plasmon amplification by stimulated emission of radiation (SPASER) [43, 44].

Conclusion

This work dealt with the theoretical and numerical study of the strong coupling between surface plasmons and guided modes with added gain in different layers of the complete stratified structure. We have focused on the phenomenon of coupling in different cases and, in the last chapter, specifically on the strong coupling regime.

More precisely, the coupling between two surface plasmons has been recalled in order to present a new device that allows the excitation of a long range surface plasmon without a symmetric medium. Currently, this structure can be experimentally achieved in the terahertz range of frequencies where metal has the behavior of a perfect electric conductor, and a doped semiconductor can take on the characteristic of metal. The surface mode which lives at the interface between the doped semiconductor and the vacuum is a classical long range surface plasmon.

Better understanding of the coupling was made possible with the presentation of the case of two coupled dielectric waveguides, with the application of the coupled-mode theory in the transverse electric and transverse magnetic polarizations. The special case of the PT symmetry was also presented.

The strong coupling regime is defined in the simple case of two coupled oscillators with the characteristic anticrossing of the dispersion curves, as compared to the weak regime. The strong coupling regime between a plasmon and a guided mode has been demonstrated. This regime is highlighted by both the dispersion and absorption curves that were numerically obtained. Special care was given to determinating the absorption curves. The usual approaches (Newton-like methods) being inefficient, we developed - after [48] - a version of the tetrachotomy algorithm which is derived from Cauchy's integral theorem.

We also demonstrated that the strong coupling regime enables to increase the propagation length of the created hybrid surface plasmon mode, which is still a very confined mode on the metallic surface. The last step involved putting gain

into different layers of the structure. We demonstrated that gain directly added into the core of the waveguide does not really enhance the plasmon emission in comparison to the guided mode. However, gain in the layer that separates the two strongly coupled modes greatly improves the propagation length of the two hybrid modes. We finally obtained a hybrid surface plasmon with a propagation length superior to 6 mm and a very satisfactory confinement of 50 nm on the metallic surface.

These results were obtained in the visible range of frequencies and can be easily reproduced in other frequency ranges with other materials. For a given structure, those are the properties, and more precisely the dispersion relation of the surface plasmon, which impose the other parameters such as the distance of the SP mode from the core of the dielectric waveguide or the thickness of this core, in order to obtain the coupling.

This work can be extended to the numerical and experimental observations of an excited long range surface plasmon on a doped semiconductor layer, deposited on a metal in the terahertz range of frequencies. But the most important goal is the continuation of the work concerning the enhancement of the SP emission. An interesting approach would be to use the Maxwell-Bloch equations so as to take into account the gain medium [197, 198, 199, 200] and allow a more physical result. This system of equations is often used in the computation of lasing phenomena. When an experimental realization of a SPASER is made with spherical nanoparticles [44], the present approach gives new possibilities for the creation of a SPASER in stratified media that could have more practical use. Finally, we carried out the study of Maxwell-Bloch equations in one dimension with a Crank-Nicolson algorithm [201]. However, the study has to be extended to two dimensions [202] for it to be applicable in the strongly coupled structure.

Appendix A

2D dispersive FDTD

Classical studies concerning the Finite-Difference Time-Domain (FDTD) method are also published by A. Taflove [203] or D. M. Sullivan [204]. Sullivan's book gives an excellent starting reference to learn this method.

We begin by recalling Maxwell's equations with the flux density $\mathbf{D}$ in the frequency domain. The equations for the fields $\mathbf{E}$ and $\mathbf{B}$ are very similar but the presence of the coefficients ε_0 and μ_0 implies a difference of several orders of magnitude. We also consider the following change of variables:

$$\tilde{\mathbf{E}} = \sqrt{\frac{\varepsilon_0}{\mu_0}} \cdot \mathbf{E}, \tag{A.1}$$

$$\tilde{\mathbf{D}} = \sqrt{\frac{1}{\varepsilon_0 \mu_0}} \cdot \mathbf{D}. \tag{A.2}$$

And Maxwell's equations can be written as:

$$\frac{\partial \tilde{\mathbf{D}}}{\partial t} = \frac{1}{\sqrt{\varepsilon_0 \mu_0}} \nabla \times \mathbf{H}, \tag{A.3}$$

$$\tilde{\mathbf{D}}(\omega) = \varepsilon_r^*(\omega) \cdot \tilde{\mathbf{E}}(\omega), \tag{A.4}$$

$$\frac{\partial \tilde{\mathbf{H}}}{\partial t} = -\frac{1}{\sqrt{\varepsilon_0 \mu_0}} \nabla \times \mathbf{E}. \tag{A.5}$$

For two-dimensional simulation, we have to choose between the transverse mag-

netic (TM) modes and the transverse electric (TE) modes. We will work only in TM polarization, which is composed of $\tilde{\mathbf{E}}_x$, $\tilde{\mathbf{E}}_y$ and $\tilde{\mathbf{H}}_z$, in order to always allow the excitation of the surface plasmon mode. Maxwell's equations are rewritten with the fields noted as E_x, E_y and H_z :

$$\partial_t D_x = \frac{1}{\sqrt{\varepsilon_0 \mu_0}} \partial_y H_z, \tag{A.6}$$

$$\partial_t D_y = -\frac{1}{\sqrt{\varepsilon_0 \mu_0}} \partial_x H_z, \tag{A.7}$$

$$D_x(\omega) = \varepsilon_r^*(\omega) \cdot E_x(\omega), \tag{A.8}$$

$$D_y(\omega) = \varepsilon_r^*(\omega) \cdot E_y(\omega), \tag{A.9}$$

$$\partial_t H_z = \frac{1}{\sqrt{\varepsilon_0 \mu_0}} (\partial_y E_x - \partial_x E_y). \tag{A.10}$$

The finite differencing method gives the following differential equations (Fig. A.1):

$$\frac{D_x^{n+1}(i, j+1/2) - D_x^n(i, j+1/2)}{\Delta t} = \frac{1}{\sqrt{\varepsilon_0 \mu_0}} \left[\frac{H_z^{n+1/2}(i, j+1) - H_z^{n+1/2}(i, j)}{\Delta y} \right], \tag{A.11}$$

$$\frac{D_y^{n+1}(i+1/2, j) - D_x^n(i+1/2, j)}{\Delta t} = -\frac{1}{\sqrt{\varepsilon_0 \mu_0}} \left[\frac{H_z^{n+1/2}(i+1, j) - H_z^{n+1/2}(i, j)}{\Delta x} \right], \tag{A.12}$$

$$\begin{aligned} \frac{H_z^{n+1/2}(i, j) - H_z^{n-1/2}(i, j)}{\Delta t} = & -\frac{1}{\sqrt{\varepsilon_0 \mu_0}} \left[\frac{E_y^n(i+1/2, j) - E_y^n(i-1/2, j)}{\Delta x} \right] \\ & + \frac{1}{\sqrt{\varepsilon_0 \mu_0}} \left[\frac{E_x^n(i, j+1/2) - E_x^n(i, j-1/2)}{\Delta y} \right]. \end{aligned} \tag{A.13}$$

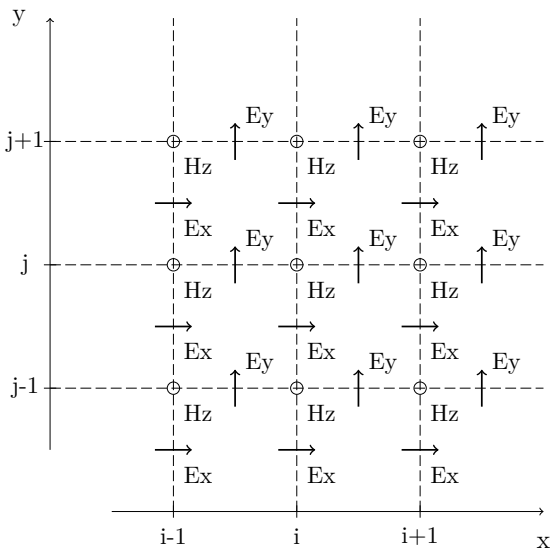

Figure A.1: Yee's scheme: Interleaving of the E and H fields for the two-dimensional TM formulation.

The time step

We consider that the cell size is the same in the two directions $\Delta x = \Delta y = \Delta l$, and the time step is noted Δt. An electromagnetic wave propagating in vacuum cannot go faster than the speed of light c. To propagate to a distance of one cell requires a minimum time $\Delta t = \Delta l/c$. Obviously, two-dimensional simulation requires $\Delta t = \Delta l/\sqrt{2}$ and three-dimensional simulation requires $\Delta t = \Delta l/\sqrt{3}$. These conditions are summarized as the "Courant condition":

$$\Delta t \leq \frac{\Delta l}{\sqrt{n}c}, \tag{A.14}$$

with n the dimension of the simulation. To simplify our computations, we determine Δt by:

$$\Delta t = \frac{\Delta l}{2c}. \tag{A.15}$$

Therefore:

$$\frac{1}{\sqrt{\varepsilon_0 \mu_0}} \frac{\Delta t}{\Delta l} = c \frac{(\Delta l/2)c}{\Delta l} = \frac{1}{2}. \tag{A.16}$$

We also replace the coefficient $1/\sqrt{\varepsilon_0\mu_0}$ by $1/2$ in our computations.

Reformulation in the time domain

We rewrite these equations in the time domain. We also assume that we are dealing with a lossy dielectric medium of the form:

$$\varepsilon_r^*(\omega) = \varepsilon_r + \frac{\sigma}{i\omega\varepsilon_0}, \tag{A.17}$$

and substitute Eq. A.17 into Eq. A.4:

$$\mathbf{D}(\omega) = \varepsilon_r \cdot \mathbf{E}(\omega) + \frac{\sigma}{i\omega\varepsilon_0}\mathbf{E}. \tag{A.18}$$

In the time domain:

$$\mathbf{D}(t) = \varepsilon_r \cdot \mathbf{E}(t) + \frac{\sigma}{\varepsilon_0}\int_0^t \mathbf{E}(t') \cdot \mathrm{d}t'. \tag{A.19}$$

The integral can be approximated as a summation over the time step Δt:

$$\mathbf{D}^n = \varepsilon_r \cdot \mathbf{E}^n + \frac{\sigma\Delta t}{\varepsilon_0}\mathbf{E}^n + \frac{\sigma\Delta t}{\varepsilon_0}\sum_{i=0}^{n-1}\mathbf{E}_i. \tag{A.20}$$

Then:

$$\mathbf{E}^n = \frac{\mathbf{D}^n - \frac{\sigma\Delta t}{\varepsilon_0}\sum_{i=0}^{n-1}\mathbf{E}_i}{\varepsilon_r + \frac{\sigma\Delta t}{\varepsilon_0}}. \tag{A.21}$$

We denote a new parameter for the summation:

$$I^n = \frac{\sigma\Delta t}{\varepsilon_0}\sum_{i=0}^{n-1}\mathbf{E}_i, \tag{A.22}$$

and Eq. A.21 can be reformulated as:

$$\begin{aligned} \mathbf{E}^n &= \frac{\mathbf{D}^n - \frac{\sigma\Delta t}{\varepsilon_0}\sum_{i=0}^{n-1}\mathbf{E}_i}{\varepsilon_r + \frac{\sigma\Delta t}{\varepsilon_0}}, \\ I^n &= I^{n-1} + \frac{\sigma\Delta t}{\varepsilon_0}E^n. \end{aligned} \tag{A.23}$$

The absorbing boundary condition

The FDTD computation is always in a "close window". Absorbing boundary conditions are necessary to keep outgoing fields from being reflected back into the problem space. To avoid this reflection, we have to add a layer known as a perfectly matched layer (PML).

To calculate the **E** field, we need to know the surrounding **H** values. At the edge of the problem space, we do not have the value for one side but we also know that there are no sources outside the problem space. Therefore, the fields at the edge must be propagating outward.

We look for a boundary condition at the end where $j = 0$. The speed of a wave which is propagating toward a boundary in free space, noted c, is the speed of light in vacuum. Then, for one time step, the wave travels the following distance:

$$\mathrm{d} = c \cdot \Delta t = c\frac{\Delta l}{2c} = \frac{\Delta l}{2}. \tag{A.24}$$

In this case, the wave takes two time steps to cross one cell. An acceptable boundary condition might be:

$$E_y^n(0) = E_y^{n-2}(1). \tag{A.25}$$

This kind of PML is enough for us if the metallic film does not touch the absorbing layer. The implementation of this PML in two dimensions is presented in [204].

Dispersive media

The dielectric permittivity and the conductivity of most media vary at different frequencies, as in the case of a metallic medium for which a Drude model has to be implemented in the FDTD.

A very simple point of view is the following. Let us consider a medium in one dimension for which the dielectric permittivity and the conductivity vary over a given frequency range. The electric field is also noted E and the flux density D. A classical formulation of its permittivity is the Debye formulation:

$$\varepsilon_r^*(\omega) = \varepsilon_r + \frac{\sigma}{i\omega\varepsilon_0} + \frac{\chi}{1 + i\omega t_0}. \tag{A.26}$$

In order to stimulate this medium, Eq. A.26 must be put into the time domain. We also defined:

$$S(\omega) = \frac{\chi}{1 + i\omega t_0} E(\omega). \tag{A.27}$$

In the time domain, Eq. A.27 in the frequency domain becomes the convolution:

$$S(t) = \frac{\chi}{t_0} \int_0^t e^{-(t'-t)/t_0} E(t') \cdot \mathrm{d}t'. \tag{A.28}$$

The integral can be approximated as a summation over the time step Δt:

$$\begin{aligned} S^n &= \chi \cdot \frac{\Delta t}{t_0} \sum_{i=0}^{n} e^{-\Delta t(n-i)/t_0} \cdot E^i \\ &= \chi \cdot \frac{\Delta t}{t_0} \left(E^n + \sum_{i=0}^{n-1} e^{-\Delta t(n-i)/t_0} \cdot E^i \right), \end{aligned} \tag{A.29}$$

and:

$$\begin{aligned} S^{n-1} &= \chi \cdot \frac{\Delta t}{t_0} \sum_{i=0}^{n-1} e^{-\Delta t(n-1-i)/t_0} \cdot E^i \\ &= \chi \cdot \frac{\Delta t}{t_0} e^{\Delta t/t_0} \sum_{i=0}^{n-1} e^{-\Delta t(n-i)/t_0} \cdot E^i. \end{aligned} \tag{A.30}$$

Substituting this value into Eq. A.29 gives:

$$S^n = \chi \cdot \frac{\Delta t}{t_0} \cdot E^n + e^{-\Delta t/t_0} S^{n-1}. \tag{A.31}$$

The flux density becomes:

$$\begin{aligned} D^n &= \varepsilon_r \cdot E^n + I^n + S^n \\ &= \varepsilon_r \cdot E^n + \left[\frac{\sigma \cdot \Delta t}{\varepsilon_0} \cdot E^n + I^{n-1} \right] + \left[\chi \cdot \frac{\Delta t}{t_0} \cdot E^n + e^{-t/t_0} \cdot S^{n-1} \right], \end{aligned} \tag{A.32}$$

and the electric field can be written as:

$$E^n = \frac{D^n - I^{n-1} - e^{-\Delta t/t_0} S^{n-1}}{\varepsilon_r + \frac{\sigma \cdot \Delta t}{\varepsilon_0} + \chi \cdot \frac{\Delta t}{t_0}}, \tag{A.33}$$

with:

$$I^n = I^{n-1} + \frac{\sigma \cdot \Delta t}{\varepsilon_0} \cdot E^n, \tag{A.34}$$

$$S^n = e^{-\Delta t/t_0} S^{n-1} + \chi \cdot \frac{\Delta t}{t_0} \cdot E^n. \tag{A.35}$$

However, another possibility, more powerful, is the use of the Z transforms for the FDTD formulation of dispersive media [204]. We start again with the calculation of E in a Debye media, in one dimension. We begin in the frequency domain:

$$D(\omega) = \left(\varepsilon_r + \frac{\sigma}{i\omega\varepsilon_0} + \frac{\chi}{1 + i\omega t_0} \right) \cdot E(\omega). \tag{A.36}$$

In the Z domain, the flux density becomes directly:

$$D(z) = \varepsilon_r \cdot E(z) + \frac{\sigma \cdot \Delta t/\varepsilon_0}{1 - z^{-1}} \cdot E(z) + \frac{\chi \cdot \Delta t/t_0}{1 + z^{-1}} \cdot E(z). \tag{A.37}$$

This equation can be rewritten as:

$$D(z) = \varepsilon_r \cdot E(z) + z^{-1} I(z) + \frac{\sigma \cdot \Delta t}{\varepsilon_0} E(z) + e^{-\Delta t/t_0} z^{-1} S(z) + \frac{\chi \cdot \Delta t}{t_0} E(z), \tag{A.38}$$

with:

$$I(z) = \frac{\sigma \cdot \Delta t/\varepsilon_0}{1 - z^{-1}} \cdot E(z) = z^{-1} I(z) + \frac{\sigma \cdot \Delta t}{\varepsilon_0} E(z), \tag{A.39}$$

$$S(z) = \frac{\chi \cdot \Delta t/t_0}{1 - e^{-\Delta t/t_0} z^{-1}} \cdot E(z) = e^{-\Delta t/t_0} z^{-1} S(z) + \frac{\chi \Delta t}{t_0} E(z). \tag{A.40}$$

The electric field is also:

$$E(z) = \frac{D(z) - z^{-1} I(z) - e^{-\Delta t/t_0} z^{-1} S(z)}{\varepsilon_r + \frac{\sigma \cdot \Delta t}{\varepsilon_0} + \chi \cdot \frac{\Delta t}{t_0}}. \tag{A.41}$$

The advantage of the Z transforms is that the summation in the time domain only consists in replacing, for example, $E(z)$ by E^n or $z^{-1}E(z)$ by E^{n-1}. Moreover, we get exactly the same expressions for E^n, I^n and S^n without doing anything to the integrals and their approximations.

Metallic media

A metallic media can be implemented by starting with the Drude model for the dielectric permittivity:

$$\varepsilon^*(\omega) = 1 - \frac{\omega_p^2}{\omega(\omega + i\Gamma)}, \tag{A.42}$$

where Γ is the damping factor and ω_p^2 the plasma frequency. The expression of the permittivity can also be written as:

$$\varepsilon^*(\omega) = 1\frac{\omega_p^2/\Gamma}{i\omega} - \frac{\omega_p^2/\Gamma}{\Gamma + i\omega}. \tag{A.43}$$

With the Z transforms, it becomes:

$$\varepsilon^*(z) = \frac{1}{\Delta t} + \frac{\omega_p^2/\Gamma}{1 - z^{-1}} - \frac{\omega_p^2/\Gamma}{1 - e^{-\Gamma\cdot\Delta t}z^{-1}}. \tag{A.44}$$

The flux density is:

$$\begin{aligned} D(z) &= \varepsilon^*(z) \cdot E(z) \cdot \Delta t \\ &= E(z) + \frac{\omega_p^2\Delta t}{\Gamma}\left[\frac{(1 - e^{-\Gamma\cdot\Delta t})z^{-1}}{1 - (1 - e^{-\Gamma\cdot\Delta t})z^{-1} + e^{-\Gamma\cdot\Delta t}z^{-2}}\right]E(z). \end{aligned} \tag{A.45}$$

And the electric field is:

$$E(z) = D(z) - z^{-1}S(z), \tag{A.46}$$

$$S(z) = (1 - e^{-\Gamma\cdot\Delta t})z^{-1}S(z) - e^{-\Gamma\cdot\Delta t}z^{-2} + \frac{\omega_p^2\Delta t}{\Gamma}(1 - e^{-\Gamma\cdot\Delta t})E(z), \tag{A.47}$$

with:

$$S(z) = \frac{\omega_p^2\Delta t}{\Gamma}\left[\frac{(1 - e^{-\Gamma\cdot\Delta t})}{1 - (1 - e^{-\Gamma\cdot\Delta t})z^{-1} + e^{-\Gamma\cdot\Delta t}z^{-2}}\right]E(z). \tag{A.48}$$

The differential equations are written similarly to Eqs. A.11, A.12 and A.13.

Properties of the source wave

Next, we present the properties of the source wave we used. First, the temporal confinement of the source wave can be obtained with a gaussian beam of the form:

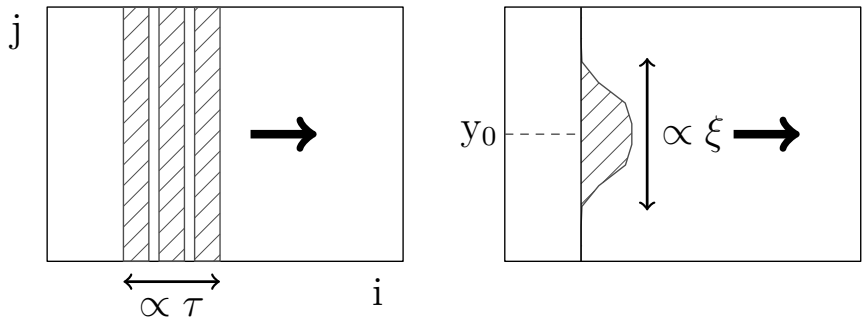

Figure A.2: Diagram of the shape of the source wave depending on parameters τ (for the temporal confinement), y_0 and ξ (for the spatial confinement).

$$e^{\frac{1}{2}\left(\frac{n\mathrm{d}t - t_0}{\tau}\right)^2}, \tag{A.49}$$

where n is the step in our algorithm, dt is the time step and ndt gives the computation time in seconds. The parameters t_0 and τ must be of the same order of size as the time step: t_0 represents the delay in time as compared to the starting time; τ characterizes the "thickness" of the source wave (Fig. A.2).

In addition, to obtain a quasi-monochromatic beam, we use a sinus of the form:

$$\sin(k_x x + k_y y - \omega t), \tag{A.50}$$

where $k_x = k_0 \Delta l \cos\theta$, $k_y = k_0 \Delta l \sin\theta$ and ω is the frequency of the source wave.

We always consider that $\Delta x = \Delta y = \Delta l = 5$ nm and $\mathrm{d}t = \Delta l/(2c)$. To compute the strong coupling regime, we take ω corresponding to the anticrossing of the dispersion curves and the angle θ corresponding to the excitation of the SP mode, as a function of the dielectric permittivities of the structure.

For the spatial confinement of the source wave, we add the following exponential:

$$e^{-(1/\xi^4)[y-y_0]^4}, \tag{A.51}$$

where the parameter ξ allows to control the spatial spread of the wave (Fig. A.2).

Then, it is possible to demonstrate that we always have the following condition

to compute a source wave:

$$\lambda \geq 10\Delta l. \tag{A.52}$$

Thus, the maximal frequency is $f_{max} = c/(10\Delta l)$. This frequency gives the maximal value for which the fourier transformation of the incident field has to be equal to zero. It is equivalent to say that we need "enough sinus" in the envelope containing the incident field to have a quasi-monochromatic incident beam (around the frequency ω).

Bibliography

[1] M. I. Stockman, "Nanophotonics : The physics behind the applications," *Phys. Today*, vol. 64, p. 39, 2011.

[2] R. W. Wood, "On a remarkable case of uneven distribution of light in a diffraction grating spectrum," *Philos. Mag.*, vol. 4, p. 396, 1902.

[3] R. H. Ritchie, "Plasma losses by fast electrons in thin films," *Phys. Rev.*, vol. 106, no. 5, p. 874, 1957.

[4] C. J. Powell and J. B. Swan, "Effect of oxidation of the characteristic loss spectra of aluminium and magnesium," *Phys. Rev.*, vol. 118, p. 640, 1960.

[5] H. Raether, *Surface plasmons on smooth and rough surface and on gratings.* Berlin: Springer-Verlag, 1988.

[6] U. C. Fischer and D. W. Pohl, "Observation of single-particle plasmons by near-field optical microscopy," *Phys. Rev. Lett.*, vol. 62, p. 458, 1989.

[7] P. Dawson, F. de Fornel, and J.-P. Goudonnet, "Imaging of surface plasmon propagation and edge interaction using a photon scanning tunneling microscope," *Phys. Rev. Lett.*, vol. 72, no. 18, p. 2927, 1994.

[8] R. Yang and Z. Lu, "Subwavelength plasmonic waveguides and plasmonic materials," *Intern. J. of Opt.*, vol. 2012, p. 258013, 2012.

[9] Z. Hans and S. I. Bozhevolnyi, "Radiation guiding with surface plasmon polaritons," *Rep. Prog. Phys.*, vol. 76, p. 016402, 2013.

[10] S. A. Maier and H. A. Atwater, "Plasmonics : localization and guiding of electromagnetic energy in metal/dielectric strutures," *J. oj Appl. Phys.*, vol. 98, p. 011101, 2005.

[11] A. V. Zayats and I. I. Smolyaninov, "Near-field photonics : surface plasmon polaritons and localized surface plasmons," *J. Opt. A: Pure Appl. Opt.*, vol. 5, p. S16, 2003.

[12] W. L. Barnes, A. Dereux, and T. W. Ebbesen, "Surface plasmon subwavelength optics," *Nature*, vol. 424, p. 824, 2003.

[13] A. V. Zayats, I. I. Smolyaninov, and A. A. Maradudin, "Nano-optics of surface plasmon polaritons," *Phys. Rep.*, vol. 408, p. 131, 2005.

[14] T. W. Ebbesen, H. J. Lezec, H. F. Ghaemi, T. Thio, and P. A. Wolff, "Extraordinary optical transmission through sub-wavelength hole arrays," *Nature*, vol. 391, p. 667, 1998.

[15] H. A. Bethe, "Theory of diffraction by small holes," *Phys. Rev.*, vol. 66, p. 163, 1944.

[16] Y. Fu and X. Zhou, "Plasmonic lenses : a review," *Plasmonics*, vol. 5, p. 287, 2010.

[17] J. B. Pendry, "Negative refraction makes a perfect lens," *Phys. Rev. Lett.*, vol. 85, p. 3966, 2000.

[18] N. Fang, H. Lee, C. Sun, and X. Zhang, "Sub-diffraction optical imaging with a silver superlens," *Science*, vol. 308, p. 534, 2005.

[19] J. Vickovic and M. Loncar, "Surface plasmon enhanced light-emitting diode," *Quant. Electron.*, vol. 36, no. 10, p. 1131, 2000.

[20] H. A. Atwater and A. Polman, "Plasmonics for improved photovoltaic devices," *Nature Mat.*, vol. 9, p. 205, 2010.

[21] R. J. C. Brown and M. J. T. Milton, "Nanostructures and nanostructured substrates for surface-enhanced raman scattering (sers)," *J. of Raman Spectrosc.*, vol. 39, p. 1313, 2008.

[22] K. Thyagarajan, S. Rivier, A. Lovera, and O. J. F. Martin, "Enhanced second-harmonic generation from double resonant plasmonic antennae," *Opt. Express*, vol. 20, p. 12860, 2012.

[23] A. G. Brolo, "Plasmonics for future biosensors," *Nature Photon.*, vol. 6, p. 709, 2012.

[24] Y. Jiang, H.-Y. Wang, H. Wang, B.-R. Gao, Y.-W. Hao, Y. Jin, Q.-D. Chen, and H.-B. Sun, "Surface plasmon enhanced fluorescence of dye molecules on metal grating films," *J. Phys. Chem. C*, vol. 115, no. 25, p. 12636, 2011.

[25] E. Fort and S. Gresillon, "Surface enhanced fluorescence," *Appl. Phys.*, vol. 41, no. 1, p. 013001, 2008.

[26] D. Schultz, "Plasmon resonant particles for biological detection," *Current opinion in biotechnol.*, vol. 14, p. 13, 2003.

[27] A. V. Kabashin, P. Evans, S. Pastkovsky, W. Hendren, G. A. Wurtz, R. Atkinson, R. Pollard, V. A. Podolskiy, and A. V. Zayats, "Plasmonic nanorod metamaterials for biosensing," *Nature Mat.*, vol. 8, p. 867, 2009.

[28] S. Zhijun and K. Hongkoo, "Refractive transmission of light and beam shaping with metallic nano-optic lenses," *Appl. Phys. Lett.*, vol. 85, p. 642, 2004.

[29] M. I. Stockman, "Nanoplasmonics : past, present and glimpse into future," *Opt. Express*, vol. 19, no. 22, p. 22029, 2011.

[30] E. Ozbay, "Plasmonics : merging photonics and electronics at nanoscale dimensions," *Science*, vol. 311, p. 189, 2006.

[31] J. M. Pitarke, V. M. Silkin, E. V. Chulkov, and P. M. Echenique, "Theory of surface plasmons and surface-plasmon polaritons," *Rep. Prog. Phys.*, vol. 70, pp. 1–87, 2007.

[32] D. Sarid and W. Challener, *Modern introduction to surface plasmons*. Cambridge University, 2010.

[33] K. Welford, "Surface plasmon-polariton and their uses," *Opt. and Quant. Elec.*, vol. 23, pp. 1–27, 1991.

[34] P. Berini, R. Charbonneau, N. Lahoud, and G. Mattiussi, "Characterization of long-range surface-plasmon-polariton waveguides," *J. Appl. Phys.*, vol. 98, p. 043109, 2005.

[35] S. Herminghaus, "Attenuated total reflectance as a quantum interference phenomenon," *Opt. Lett.*, vol. 19, no. 4, p. 293, 1994.

[36] P. Berini, "Long-range surface plasmon polaritons," *Advances in Opt. and Photonics*, vol. 1, p. 484, 2009.

[37] D. Sarid, "Long-range surface-plasma waves on very thin metal films," *Phys. Rev. Lett.*, vol. 47, p. 1927, 1981.

[38] M. Miyata and J. Takahara, "Excitation control of long-range surface plasmons by two incident beams," *Opt. Express*, vol. 20, p. 9493, 2012.

[39] V. N. Konopsky and E. V. Alieva, "Long-range propagation of plasmon polaritons in a thin metal film on a one-dimensional photonic crystal surface," *Phys. Rev. Lett.*, vol. 97, p. 253904, 2006.

[40] A. Yanai and U. Levy, "The role of short and long range surface plasmons for plasmonic focusing applications," *Opt. Express*, vol. 17, no. 16, p. 14270, 2009.

[41] S. Wuestner, A. Pusch, K. L. Tsakmakidis, J. M. Hamm, and O. Hess, "Overcoming losses with gain in a negative index metamaterial," *Phys. Rev. Lett.*, vol. 105, p. 127401, 2010.

[42] O. Hess, J. B. Pendry, S. A. Maier, R. F. Oulton, J. M. Hamm, and K. L. Tsakmakidis, "Active nanoplasmonic metamaterials," *Nature Mat.*, vol. 11, p. 573, 2012.

[43] D. J. Bergman and M. I. Stockman, "Surface plasmon amplification by stimulated emission radiation : quantum generation of coherent surface plasmons in nanosystems," *Phys. Rev. Lett.*, vol. 90, no. 2, p. 027402, 2003.

[44] M. A. Noginov, G. Zhu, A. M. Belgrave, R. Bakker, V. M. Shalaev, E. E. Narimanov, S. Stout, E. Herz, T. Suteewong, and U. Wiesner, "Demonstration of a spaser-based nanolaser," *Nature*, vol. 460, p. 1110, 2009.

[45] C. Symonds, G. Lheureux, J. P. Hugonin, J. J. Greffet, J. Laverdant, G. Brucoli, A. Lemaître, P. Senellart, and J. Bellessa, "Confined tamm plasmon lasers," *Nano Lett.*, vol. 13, no. 7, pp. 3179–3184, 2013.

[46] M. Kaliteevski, S. Brand, R. A. Abram, I. Iorsh, A. V. Kavokin, and I. A. Shelykh, "Hybrid states of tamm plasmons and exciton polaritons," *Appl. Phys. Lett.*, vol. 95, no. 251108, 2009.

[47] M. E. Sasin, R. P. Seisyan, M. A. Kaliteevski, S. Brand, R. A. Abram, J. M. Chamberlain, I. V. Iorsh, I. A. Shelykh, A. Y. Egorov, A. P. Vasil'ev, V. S. Mikhrin, and A. V. Kavokin, "Tamm plasmon-polaritons: First experimental observation," *Superlattices and Microstructures*, vol. 47, pp. 44–49, 2010.

[48] F. Zolla, G. Renversez, A. Nicolet, B. Kuhlmey, S. Guenneau, and D. Felbacq, *Foundations of photonic crystal fibres*. Imperial College Press, 2005.

[49] A. Yariv, "Universal relations for coupling of optical power between microresonators and dielectric waveguides," *Electronics Lett.*, vol. 36, no. 4, pp. 321–322, 2000.

[50] A. Yariv, "Coupled-mode theory for guided-wave optics," *IEEE J. of Quantum Electron.*, vol. QE-9, no. 9, p. 919, 1973.

[51] S. L. Chuang, *Physics of optoelectronic devices*. John Wiley and Sons Inc., 1995.

[52] H. A. Haus, "Coupled-mode theory," *Proc. of the IEEE*, vol. 79, 1991.

[53] H. A. Haus, W. P. Huang, S. Kawakami, and N. A. Whitaker, "Coupled-mode theory of optical waveguides," *J. of Lighwave Techno.*, vol. LT-5, no. 1, p. 16, 1987.

[54] C. M. Bender, "Real spectra in non-hermitian hamiltonian having pt symmetry," *Phys. Rev. Lett.*, vol. 80, no. 24, p. 5243, 1998.

[55] C. Weisbuch, M. Nishioka, A. Ishikawa, and Y. Arakawa, "Observation of the coupled exciton-photon mide splitting in a semiconductor quantum microcavity," *Phys. Rev. Lett.*, vol. 69, no. 23, p. 3314, 1992.

[56] B. Gayral and P. Senellart, "Contrôle de l'émission spontanée d'un émetteur à l'état solide," *Images de la Physique*, 2007.

[57] T. J. Davis, "Surface plasmon modes in multi-layer thin-films," *Opt. Comm.*, vol. 282, p. 135, 2009.

[58] D. K. Ko and J. R. Sambles, "Scattering matrix method for propagation of radiation in stratified media : attenuated total reflection studies of liquid crystals," *J. Opt. Soc. Am. A*, vol. 5, no. 11, p. 1863, 1988.

[59] A. Tishchenko, "Fenomenological representation of deep and high contrast lamellar gratings by means of the modal method," *Opt. and Quant. Elec.*, vol. 37, p. 309, 2005.

[60] D. A. Bykov and L. L. Doskolovich, "Numerical methods for calculating poles of the scattering matrix with applications in grating theory," *J. of Lighwave Techno.*, vol. 31, no. 5, p. 793, 2013.

[61] G. Gallatin, J. C. Webster, E. C. Kintner, and C. J. Morgan, "Scattering matrices for imaging layered media," *J. Opt. Soc. Am. A*, vol. 5, no. 2, p. 220, 1988.

[62] C. C. Katsidis and D. I. Siapkas, "General transfer-matrix method for optical multilayer systems with coherent, partially coherent, and incoherent interference," *Appl. Opt.*, vol. 41, no. 19, p. 3978, 2002.

[63] Z.-Y. Li, "Principles of the plane-wave transfer-matrix method for photonic crystals," *Sci. Technol. Adv. Mater.*, vol. 6, p. 837, 2005.

[64] H. T. Minden, "Scatter matrix algorithm for the transverse kerr magnetooptic effect in multilayer optical film structures," *Appl. Opt.*, vol. 29, no. 27, p. 3955, 1990.

[65] O. Buccafusca, "The mathematical group of scattering matrices: Introduction of scattering matrix multiplication," *Microw. Opt. Technol. Lett.*, vol. 49, pp. 179–183, 2007.

[66] M. Neviere, E. Popov, and R. Reinisch, "Electromagnetic resonances in linear and nonlinear optics : phenomenological study of grating behavior through the poles and zeros of the scattering operator," *J. Opt. Soc. Am. A*, vol. 12, no. 3, p. 513, 1995.

[67] G. J. Gbur, *Mathematical methods for optical sciences*, vol. chapter 9. Cambridge University, 2011.

[68] R. Petit, *L'outil mathématique.* Masson, 3rd ed. ed., 1991.

[69] P. Helluy, S. Maire, and P. Ravel, "Intégration numérique d'ordre élevé de fonctions régulières ou singulières sur un intervalle," *C. R. Acad. Sci. Paris*, vol. 327, pp. 843–848, 1998.

[70] F. Jedrzejewski, *Introduction aux méthodes numériques.* Springer-Verlag, 2nd ed., 2005.

[71] L. Novotny and B. Hecht, *Principles of nano-optics.* Cambridge University, 2nd ed. ed., 2012.

[72] P. Drude, "Zur elektronentheorie der metalle," *Annalen der Physik*, vol. 306, no. 3, pp. 566–613, 1900.

[73] E. J. Zeman and G. C. Schatz, "An accurate electromagnetic theory study of surface enhancement factors for silver, gold, copper, lithium, sodium, aluminum, gallium, indium, zinc, and cadmium," *J. Phys. Chem.*, vol. 91, pp. 634–643, 1987.

[74] B. Ong, X. Yuan, S. Tjin, and J. Zhang, "Optimised fild thickness for maximum evanescent field enhancement of a bimetallic film surface plasmon resonance biosensor," *Sensors and Actu. B*, vol. 114, pp. 1028–1034, 2006.

[75] M. Watanabe and K. Kajikawa, "An optical fiber sensor based on anomalous reflection of gold," *Sensors and Actu. B*, vol. 89, pp. 126–130, 2003.

[76] H. Raether, *Excitation of plasmons and interband transitions by electrons*, vol. 88. Berlin, Heidelberg: Springer tracts in mod. phys., 1980.

[77] W. L. Barnes, "Surface plasmon-polariton length scales : a route to sub-wavelength optics," *J. Opt. A: Pure Appl. Opt.*, vol. 8, p. S87, 2006.

[78] P. Berini, "Figures of merit for surface plasmon waveguides," *Opt. Express*, vol. 14, no. 26, p. 13030, 2006.

[79] P. Dawson, B. A. F. Puygranier, and J.-P. Goudonnet, "Surface plasmon polariton propagation length : a direct comparison using photon scanning tunneling microscopy and attenuated total reflection," *Phys. Rev. B*, vol. 63, p. 205410, 2001.

[80] J. M. Vigoureux, "De l'onde evanescente de fresnel au champ proche optique," *Annales de la Fond. Louis de Broglie*, vol. 28, no. 3, p. 525, 2003.

[81] E. Palik, *Handbook of optic constants of solids*. New York: Academic Press, 1985.

[82] F. Y. Kou and T. Tamir, "Range extension of surface plasmons by dielectric layers," *Opt. Lett.*, vol. 12, no. 5, p. 367, 1987.

[83] P. T. Worthing, "Modification of the spontaneous emission rate of eu3+ ions embedded within a dielectric layer above a silver mirror," *Phys. Rev. A*, vol. 59, p. 865, 1999.

[84] L. H. Smith, J. A. E. Wasey, and W. L. Barnes, "Light outcoupling efficiency of top-emitting organic light-emitting diodes," *Appl. Phys. Lett.*, vol. 84, p. 2986, 2004.

[85] P. B. Johnson and R. W. Christy, "Optical constants of the noble metals," *Phys. Rev. B*, vol. 6, no. 12, p. 4370, 1972.

[86] S. V. Boriskina, M. Povinelli, V. N. Astratov, A. V. Zayats, and V. A. Podolskiy, "Collective phenomena in photonic, plasmonic and hybrid structures," *Opt. Express*, vol. 19, no. 22, p. 22024, 2011.

[87] P. Berini, "Plasmon-polariton waves guided by thin lossy metal films of finite width: Bound modes of asymmetric structures," *Phys. Rev. B*, vol. 63, p. 125417, 2001.

[88] A. Hessel and A. A. Oliner, "A new theory of wood's anomalies on optical gratings," *Appl. Opt.*, vol. 4, p. 1275, 1965.

[89] R. Petit and L. C. Botten, *Electromagnetic theory of gratings*. Springer-Verlag, 1980.

[90] L. Ruan, F. Yang, and J. R. Sambles, "Otto-coupled surface plasmons in a liquid crystal cell," *Appl. Phys. Lett.*, vol. 95, p. 171102, 2009.

[91] J. A. Dionne, "Planar metal plasmon waveguides : frequency-dependent dispersion, propagation, localization, and loss beyond the free electron model," *Phys. Rev. B*, vol. 72, p. 075405, 2005.

[92] K. L. Kliewer and R. Fuchs, "Collective electronic motion in a metallic slab," *Phys. Rev.*, vol. 153, p. 498, 1967.

[93] R. Pettit, J. Silcox, and R. Vincent, "Measurement of surface-plasmon dispersion in oxidized aluminium films," *Phys. Rev. B*, vol. 11, p. 3116, 1975.

[94] G. J. Kovacs and G. D. Scott, "Optical excitation of surface plasma waves in layered media," *Phys. Rev. B*, vol. 16, p. 1297, 1977.

[95] M. Fukui, V. C. Y. So, and R. Normandin, "Lifetimes of surface plasmons in thin silver films," *Phys. Status Solidi*, vol. 91, p. K61, 1979.

[96] G. J. Kovacs and G. D. Scott, "Attenuated total reflection angular spectra of an ag film bounded by dielectric slabs," *Canadian J. Phys.*, vol. 56, no. 9, p. 1235, 1978.

[97] J. C. Quail, J. G. Rako, and H. J. Simon, "Long-range surface-plasmon modes in silver and aluminium films," *Opt. Lett.*, vol. 8, p. 377, 1983.

[98] J. C. Quail, J. G. Rako, H. J. Simon, and R. T. Deck, "Optical second-harmonic generation with long-range surface plasmons," *Phys. Rev. Lett.*, vol. 50, p. 1987, 1983.

[99] B. Lamprecht, J. R. Krenn, G. Schider, H. Ditlbacher, M. Salerno, N. Felidj, A. Leitner, F. R. Aussenegg, and J. C. Weeber, "Surface plasmon propagation in microscale metal stripes," *Appl. Phys. Lett.*, vol. 79, p. 51, 2001.

[100] J. C. Weeber, J. R. Krenn, A. Dereux, B. Lamprecht, Y. Lacroute, and J. P. Goudonnet, "Near-field observation of surface plasmon polariton propagation on thin metal stripes," *Phys. Rev. B*, vol. 64, p. 045411, 2001.

[101] G. G. Nenninger, P. Tobiska, J. Homola, and S. S. Yee, "Long-range surface plasmons for high-resolution surface plasmon resonance sensors," *Sensors and Actu. B*, vol. 74, p. 145, 2001.

[102] R. F. Oulton, V. J. Sorger, D. A. Genov, D. F. P. Pile, and X. Zhang, "A hybrid plasmonic waveguide for subwavelength and long-range propagation," *Nature Photon.*, vol. 2, p. 496, 2008.

[103] X. Shi, S. Zheng, H. Chi, X. Jin, and X. Zhang, "All-optical modulator with long range surface plasmon resonance," *Opt. and Laser Techn.*, vol. 49, p. 316, 2013.

[104] P. Berini, "Plasmon-polariton waves guided by thin lossy metal films of finite width: Bound modes of symmetric structures," *Phys. Rev. B*, vol. 61, no. 15, p. 10484, 2000.

[105] J. Guo and R. Adato, "Extended long range plasmon waves in finite thickness metal film layered dielectric materials," *Opt. Express*, vol. 14, no. 25, p. 12409, 2006.

[106] J. Yoon, S. H. Song, and S. Park, "Flat-top surface plasmon-polariton modes guided by double-electrode structures," *Opt. Express*, vol. 15, p. 17151, 2007.

[107] D. Ballester, M. S. Tame, C. Lee, and M. S. Kim, "Long-range surface-plasmon-polariton excitation at the quantum level," *Phys. Rev. A*, vol. 79, p. 053845, 2009.

[108] Nagaraj and A. A. Krokhin, "Long-range surface plasmons in dielectric-metal-dielectric structure with highly anisotropic substrates," *Phys. Rev. B*, vol. 81, p. 085426, 2010.

[109] C. R. Williams, S. R. Andrews, S. A. Maier, A. I. Fernandez-Dominguez, L. Martin-Moreno, and F. J. Garcia-Vidal, "Highly confined guiding of terahertz surface plasmon polaritons on highly confined guiding of terahertz surface plasmon polaritons on structured metal surfaces," *Nature Photon.*, vol. 2, p. 175, 2008.

[110] R. Harrington, *Time-harmonic electromagnetic fields*. IEEE Press Classic Reissue, 2001 (origin. 1961).

[111] R. P. Feynman, *The Feynman lectures on physics vol 2 : Mainly electromagnetism and matter*. Addison Wesley, 1963.

[112] P. Gadenne and G. Vuye, "In situ determination of the optical and electrical properties of thin films during their depositions," *J. Phys. E*, vol. 10, p. 733, 1977.

[113] Y.-J. Lu, J. Kim, H.-Y. Chen, C. Wu, and N. D. et al., "Plasmonic nanolaser using epitaxially grown silver film," *Science*, vol. 337, p. 450, 2012.

[114] L. Shen, X. Chen, and T.-J. Yang, "Terahertz surface plasmon polaritons on terahertz surface plasmon polaritons on periodically corrugated metal surfaces," *Opt. Express*, vol. 16, no. 5, p. 3326, 2008.

[115] J. G. Rivas, C. Janke, P. H. Bolivar, and H. Kurz, "Transmission of thz radiation through insb gratings of subwavelength apertures," *Opt. Express*, vol. 13, no. 3, p. 847, 2005.

[116] M. van Exter and D. Grischkowsky, "Optical and electronic properties of doped silicon from 0.1 to 2 thz," *Appl. Phys. Lett.*, vol. 56, no. 17, p. 1694, 1990.

[117] A. W. Snyder and J. D. Love, *Optical waveguide theory.* Springer, 1983.

[118] R. Magnanini and F. Santosa, "Wave propagation in a 2-d optical waveguide," *SIAM J. Appl. Math.*, vol. 61, no. 4, pp. 1237–1252, 2000.

[119] D. Marcuse, *Theory of dielectric optical waveguides.* Academic Press, 1974.

[120] B. E. Little and W. P. Huang, "Coupled-mode theory for optical waveguides," *Progress in Electromagn. Research*, vol. 10, pp. 217–270, 1995.

[121] R. R. A. Syms, "Improved coupled-mode theory for codirectionally and contradirectionally coupled waveguides arrays," *J. Opt. Soc. Am. A*, vol. 8, p. 1062, 1991.

[122] E. A. J. Marcatili, "Improved coupled-mode equations for dielectric guides," *Quant. Electron.*, vol. 22, pp. 988–993, 1986.

[123] E. A. J. Marcatili, L. L. Buhl, and R. C. Alferness, "Experimental verification of the improved coupled-mode equations," *Appl. Phys. Lett.*, vol. 49, p. 1692, 1986.

[124] S. L. Chuang, "A coupled-mode theory for multiwaveguide systems satisfying the reciprocity theorem and power conservation," *J. of Lighwave Techno.*, vol. 5, p. 174, 1987.

[125] S. L. Chuang, "Application of the strongly coupled-mode theory to integrated optical devices," *Quant. Electron.*, vol. 23, p. 499, 1987.

[126] C. M. Bender, "Pt-symmetric quantum mechanics," *J. of Math. Phys.*, vol. 40, pp. 2201–2229, 1999.

[127] C. M. Bender, "Generalized pt symmetry and real spectra," *J. of Phys. A: Math. and General*, vol. 35, pp. L467–L471, 2002.

[128] A. Mostafazadeh, "Spectral singularities of complex scattering potentials and infinite reflection and transmission coefficients at real energies," *Phys. Rev. Lett.*, vol. 102, p. 220402, 2009.

[129] R. El-Ganainy, K. G. Makris, D. N. Christodoulides, and Z. H. Musslimani, "Theory of coupled optical pt-symmetric structures," *Opt. Lett.*, vol. 32, no. 17, p. 2632, 2007.

[130] S. Klaiman, U. Günther, and N. Moiseyev, "Visualization of branch points in pt-symmetric waveguides," *Phys. Rev. Lett.*, vol. 101, p. 080402, 2008.

[131] Z. H. Musslimani, "Optical solitons in pt periodic potentials," *Phys. Rev. Lett.*, vol. 100, p. 030402, 2008.

[132] K. G. Makris, "Pt-symmetric optical lattices," *Phys. Rev. A*, vol. 81, p. 063807, 2010.

[133] A. Guo, G. J. Salamo, D. Duchesne, R. Morandotti, M. Volatier-Ravat, V. Aimez, G. A. Siviloglou, and D. N. Christodoulides, "Observation of pt-symmetry breaking in complex optical potentials," *Phys. Rev. Lett.*, vol. 103, p. 093902, 2009.

[134] C. E. Rüter, K. G. Makris, R. El-Ganainy, D. N. Christodoulides, M. Segev, and D. Kip, "Observation of parity-time symmetry in optics," *Nature Phys.*, vol. 6, pp. 192–195, 2010.

[135] C. M. Bender, "Making sense of non-hermitian hamiltonians," *Rep. Prog. Phys.*, vol. 70, pp. 947–1018, 2007.

[136] C. M. Bender, "Spontaneous breaking of classical pt symmetry," *J. of Math. Phys.*, vol. 48, p. 042703, 2007.

[137] A. Mostafazadeh, "Pseudo-hermicity versus pt-symmetry iii: Equivalence of pseudo-hermicity and the presence of antilinear symmetries," *J. of Math. Phys.*, vol. 43, pp. 3944–3951, 2002.

[138] Z. Ahmed, "Real and complex discrete eigenvalues in an exactly solvable one-dimensional complex pt-invariant potential," *Phys. Lett. A*, vol. 282, pp. 343–348, 2001.

[139] O. Bendix, R. Fleischmann, T. Kottos, and B. Shapiro, "Exponentially fragile pt symmetry in lattices with localized eigenmodes," *Phys. Rev. Lett.*, vol. 103, p. 030402, 2009.

[140] K. G. Makris, R. El-Ganainy, and D. N. Christodoulides, "Beam dynamics in pt-symmetric optical lattices," *Phys. Rev. Lett.*, vol. 100, p. 103904, 2008.

[141] P. G. Kevrekidis, Z. Chen, B. A. Malomed, D. J. Frantzeskakis, and M. I. Weinstein, "Spontaneous symmetry breaking in photonic lattices : Theory and experiment," *Phys. Lett. A*, vol. 340, p. 275280, 2005.

[142] J. F. Jia, Y. P. Zhang, W. D. Li, and L. Li, "Optical modes in a nonlinear double-channel waveguide," *Opt. Comm.*, vol. 283, pp. 132–137, 2010.

[143] R. J. Li, F. Lv, L. Li, and Z. Y. Xu, "Symmetry breaking and manipulation of nonlinear optical modes in an asymmetric double-channel waveguide," *Phys. Rev. A*, vol. 84, p. 033850, 2011.

[144] T. Kato, *Perturbation theory of linear operators*. Springer, 1966.

[145] L. Novotny, "Strong coupling, energy splitting, and level crossings : A classical perspective," *Am. J. Phys.*, vol. 78, no. 11, p. 1199, 2010.

[146] J. P. Reithmaier, G. Sek, A. Löffler, C. Hofmann, and S. K. et al., "Strong coupling in a single quantum dot-semiconductor microcavity system," *Nature*, vol. 432, no. 7014, pp. 197–200, 2004.

[147] L. C. Andreani and G. Panzarini, "Strong-coupling regime for quantum boxes in pillar microcavities : Theory," *Phys. Rev. B*, vol. 60, pp. 13276–13279, 1999.

[148] C. Cohen-Tannoudji, *Quantum mechanics*, vol. 1. John Wiley and Sons Inc., 2006.

[149] S. Rudin and T. L. Reinecke, "Oscillator model for vacuum rabi splitting in microcavities," *Phys. Rev. B*, vol. 59, p. 10227, 1999.

[150] X.-G. Zhao, G. A. Georgakis, and Q. Niu, "Rabi oscillations between bloch bands," *Phys. Rev. B*, vol. 54, pp. R5235–R5238, 1996.

[151] T. Yoshie, A. Scherer, J. Hendrickson, G. Khitrova, H. M. Gibbs, G. Rupper, C. Ell, O. B. Shchekin, and D. G. Deppe, "Vacuum rabi splitting with a single quantum dot in a photonic crystal nanocavity," *Nature*, vol. 432, pp. 200–203, 2004.

[152] T. B. Norris, J.-K. Rhee, and C.-Y. Sung, "Time-resolved vacuum rabi oscillations in a semiconductor quantum microcavity," *Phys. Rev. B*, vol. 50, pp. 14663–14666, 1994.

[153] R. Houdré, R. P. Stanley, U. Oesterle, and C. Weisbuch, "Strong coupling regime in semiconductor microcavities," *C. R. Physique*, vol. 3, pp. 15–27, 2002.

[154] E. Centeno and D. Felbacq, "Rabi oscillations in bidimensional photonic crystals," *Phys. Rev. B*, vol. 62, p. 10101, 2000.

[155] V. M. Agranovich, M. Litinskala, and D. G. Lidzey, "Cavity polaritons in microcavities containing disordered organic semiconductors," *Phys. Rev. B*, vol. 67, p. 085311, 2003.

[156] G. Khitrova, H. M. Gibbs, M. Kira, S. W. Koch, and A. Scherer, "Vacuum rabi splitting in semiconductors," *Nature Phys.*, vol. 2, pp. 81–90, 2006.

[157] R. Houdré, J. L. Gibernon, P. Pellandini, R. P. Stanley, U. Oesterle, C. Weisbuch, J. O'Gorman, B. Roycroft, and M. Llegems, "Saturation of the strong-coupling regime in a semiconductor microcavity: Free-carrier bleaching of cavity polaritons," *Phys. Rev. B*, vol. 52, pp. 7810–7813, 1995.

[158] M. S. Skolnick, T. A. Fisher, and D. M. Whittaker, "Strong coupling phenomena in quantum microcavity structures," *Semicond. Sci. Technol.*, vol. 13, p. 645, 1998.

[159] G. Khitrova, H. M. Gibbs, F. Jahnke, M. Kira, and S. W. Koch, "Nonlinear optics of normal-mode-coupling semiconductor microcavities," *Rev. Mod. Phys.*, vol. 71, pp. 1591–1639, 1999.

[160] R. J. Holmes and S. R. Forrest, "Strong exciton-photon coupling in organic materials," *Organic Electron.*, vol. 8, pp. 77–93, 2007.

[161] D. G. Lidzey, D. D. C. Bradleya, M. S. Skolnick, T. Virgili, S. Walker, and D. M. Whittaker, "Strong exciton-photon coupling in an organic semiconductor microcavity," *Nature*, vol. 395, pp. 53–55, 1998.

[162] D. G. Lidzey, D. D. C. Bradley, A. Armitage, S. Walker, and M. S. Skolnick, "Photon-mediated hybridization of frenkel excitons in organic semiconductor microcavities," *Science*, vol. 288, no. 5471, pp. 1620–1623, 2000.

[163] P. Schouwink, H. V. Berlepsch, L. Dähne, and R. F. Mahrt, "Observation of strong exciton-photon coupling in an organic microcavity," *Chem. Phys. Lett.*, vol. 344, p. 352, 2001.

[164] N. Takada, T. Kamata, and D. D. C. Bradley, "Polariton emission from polysilane-based organic microcavities," *Appl. Phys. Lett.*, vol. 82, p. 1812, 2003.

[165] M. Pope and C. E. Swenberg, *Electronic Processes in Organic Crystals and Polymers*. Oxford Univ. Press, 1999.

[166] D. G. Lidzey, D. D. C. Bradley, T. Virgili, A. Armitage, M. S. Skolnick, and S. Walker, "Observation of strong exciton-photon coupling in semiconductor microcavities containing organic dyes and j-aggregates," *Opt. Mater.*, vol. 12, pp. 243–247, 1999.

[167] A. I. Tartakovskii, M. Emam-Ismail, and D. G. L. et al., "Raman scattering in strongly coupled organic semiconductor microcavities," *Phys. Rev. B*, vol. 63, p. 121302, 2001.

[168] A. Brehler, R. Parashkov, J. S. Lauret, and E. Deleporte, "Strong exciton-photon coupling in a microcavity containing layered perovskite semiconductors," *Appl. Phys. Lett.*, vol. 89, p. 171110, 2006.

[169] J. R. Tischler, M. S. Bradley, and V. Bulovic, "Strong coupling in a microcavity led," *Phys. Rev. Lett.*, vol. 95, p. 036401, 2005.

[170] F. Médard, J. Zuniga-Perez, P. Disseix, M. Mihailovic, J. Leymarie, A. Vasson, F. Semond, E. Frayssinet, J. C. Moreno, M. Leroux, S. Faure, and T. Guillet, "Experimental observation of strong light-matter coupling in zno microcavities: Influence of large excitonic absorption," *Phys. Rev. B*, vol. 79, p. 125302, 2009.

[171] S. Faure, C. Brimont, T. Guillet, T. Bretagnon, B. Gil, F. Médard, D. Lagarde, P. Disseix, J. Leymarie, J. Zuniga-Perez, M. Leroux, E. Frayssinet, J. C. Moreno, F. Semond, and S. Bouchoule, "Relaxation and emission of bragg-mode and cavity-mode polaritons in a zno microcavity at room temperature," *Appl. Phys. Lett.*, vol. 95, p. 121102, 2009.

[172] J. Bellessa, C. Bonnand, and J. C. Plenet, "Strong coupling between surface plasmons and excitons in an organic semiconductor," *Phys. Rev. Lett.*, vol. 93, p. 036404, 2004.

[173] J. Dintinger, S. Klein, F. Bustos, W. L. Barnes, and T. W. Ebbesen, "Strong coupling between surface plasmon-polaritons and organic molecules in subwavelength hole arrays," *Phys. Rev. B*, vol. 71, p. 035424, 2005.

[174] I. Pockrand, A. Brillante, and D. Möbius, "Exciton–surface plasmon coupling: An experimental investigation," *J. of Chem. Phys.*, vol. 77, p. 6289, 1982.

[175] N. I. Cade, T. Ritman-Meer, and D. Richards, "Strong coupling of localized plasmons and molecular excitons in nanostructured silver films," *Phys. Rev. B*, vol. 79, p. 241404, 2009.

[176] Y. Sugawara, T. A. Kelf, J. J. Baumberg, M. E. Abdelsalam, and P. N. Bartlett, "Strong coupling between localized plasmons and organic excitons in metal nanovoids," *Phys. Rev. Lett.*, vol. 97, p. 266808, 2006.

[177] S. Nie and S. R. Emory, "Probing single molecules and single nanoparticles by surface-enhanced raman scattering," *Science*, vol. 275, no. 5303, pp. 1102–1106, 1997.

[178] S. V. Baieva, T. K. Hakala, and J. J. Toppari, "Strong coupling between surface plasmon polaritons and sulforhodamine 101 dye," *Nanoscale Research Lett.*, vol. 7, p. 191, 2012.

[179] S. V. Baieva, J. A. Lhalainen, and J. J. Toppari, "Strong coupling between surface plasmon polaritons and beta-carotene in nanolayered system," *J. of Chem. Phys.*, vol. 138, p. 044707, 2013.

[180] Z. Xi, Y. Lu, W. Yu, P. Yao, P. Wang, and H. Ming, "Strong coupling between plasmonic fabry–pérot cavity mode and magnetic plasmon," *Opt. Lett.*, vol. 38, pp. 1591–1593, 2013.

[181] A. Christ, S. G. Tikhodeev, N. A. Gippius, J. Kuhl, and H. Giessen, "Waveguide-plasmon polaritons: Strong coupling of photonic and electronic resonances in a metallic photonic crystal slab," *Phys. Rev. Lett.*, vol. 91, p. 183901, 2003.

[182] R. Ameling, D. Dregely, and H. Giessen, "Strong coupling of localized and surface plasmons to microcavity modes," *Opt. Lett.*, vol. 36, pp. 2218–2220, 2011.

[183] C. J. Tang, P. Zhan, Z. S. Cao, J. Pan, Z. Chen, and Z. L. Whang, "Magnetic field enhancement at optical frequencies through diffraction coupling of magnetic plasmon resonances in metamaterials," *Phys. Rev. B*, vol. 83, p. 041402, 2011.

[184] C. Symonds, C. Bonnand, J. C. Plenet, A. Bréhier, R. Parashkov, J. S. Lauret, E. Deleporte, and J. Bellessa, "Particularities of surface plasmon–exciton strong coupling with large rabi splitting," *New J. of Phys.*, vol. 10, p. 065017, 2008.

[185] C. Bonnand, J. Bellessa, C. Symonds, and J. C. Plenet, "Polaritonic emission via surface plasmon cross coupling," *Appl. Phys. Lett.*, vol. 89, p. 231119, 2006.

[186] C. Bonnand, J. Bellessa, and J. C. Plenet, "Properties of surface plasmons strongly coupled to excitons in an organic semiconductor near a metallic surface," *Phys. Rev. B*, vol. 73, p. 245330, 2006.

[187] R. Houdré, R. P. Stanley, U. Oesterle, and M. Llegems, "Room-temperature cavity polaritons in a semiconductor microcavity," *Phys. Rev. B*, vol. 49, pp. 16761–16764, 1994.

[188] O. Benson, "Assembly of hybrid photonic architectures from nanophotonic constituents," *Nature*, vol. 480, pp. 193–199, 2011.

[189] V. J. Sorger, R. F. Oulton, J. Yao, G. Bartal, and X. Zhang, "Plasmonic fabry-pérot nanocavity," *Nano Lett.*, vol. 9, pp. 3489–3493, 2009.

[190] K. J. Vahala, "Optical microcavities," *Nature*, vol. 424, pp. 839–846, 2003.

[191] E. Peter, P. Senellart, D. Martrou, A. Lemaître, J. Hours, J. M. Gérard, and J. Bloch, "Exciton-photon strong-coupling regime for a single quantum dot embedded in a microcavity," *Phys. Rev. Lett.*, vol. 95, p. 067401, 2005.

[192] A. V. Kavokin, I. A. Shelykh, and G. Malpuech, "Lossless interface modes at the boundary between two periodic dielectric structures," *Phys. Rev. B*, vol. 72, p. 233102, 2005.

[193] M. Kaliteevski, I. Iorsh, S. Brand, R. A. Abram, J. M. Chamberlain, A. V. Kavokin, and I. A. Shelykh, "Tamm plasmon-polaritons: Possible electromagnetic states at the interface of a metal and a dielectric bragg mirror," *Phys. Rev. B*, vol. 76, p. 165415, 2007.

[194] C. Symonds, A. Lemaître, E. Homeyer, J. C. Plenet, and J. Bellessa, "Emission of tamm plasmon/exciton polaritons," *Appl. Phys. Lett.*, vol. 95, p. 151114, 2009.

[195] J. Bellessa, S. Rabaste, J. C. Plenet, and J. Dumas, "Eu3plus-doped microcavities fabricated by sol-gel process," *Appl. Phys. Lett.*, vol. 79, no. 14, p. 2142, 2001.

[196] J. Bellessa, C. Symonds, C. Meynaud, J. C. Plenet, E. Cambril, A. Miard, L. Ferlazzo, and A. Lemaître, "Exciton/plasmon polariton in gaas / al0.93ga0.07as heterostructures near a metallic layer," *Phys. Rev. B*, vol. 78, p. 205326, 2008.

[197] B. Bidégaray-Fesquet, *Hiérarchie de modèles en optique quantique*. Springer, 2000.

[198] A. Bourgeade and O. Saut, "Numerical methods for the bidimensional maxwell-bloch equations in nonlinear crystals," *J. of Computational Phys.*, vol. 213, pp. 823–843, 2006.

[199] B. Bidégaray, "Time discretizations for maxwell-bloch equations," *Num. Meth. for Partial Diff. Eq.*, vol. 19, pp. 284–300, 2003.

[200] J. Xiong, M. Colice, F. Schlottau, K. Wagner, and B. Fornberg, "Numerical solutions to 2d maxwell-bloch equations," *Opt. Quant. Electron.*, vol. 40, pp. 447–453, 2008.

[201] R. W. Ziolkowski, J. M. Arnold, and D. M. Gogny, "Ultrafast pulse interactions with two-level atoms," *Phys. Rev. A*, vol. 52, no. 4, p. 3082, 1995.

[202] G. Slavcheva, J. M. Arnold, I. Wallace, and R. W. Ziolkowski, "Coupled maxwell-pseudospin equations for investigations of self-induced transparency effects in a degenerate three-level quantum system in two dimensions: Finite-difference time-domain study," *Phys. Rev. A*, vol. 66, p. 063418, 2002.

[203] A. Taflove and S. C. Hagness, *Computational electrodynamics : The finite-difference time-domain method*. Artech house, 2005.

[204] D. M. Sullivan, *Electromagnetic simulation using the fdtd method*. IEEE Publications, 2000.